Scour at the Base of Bridge Piers: Monitoring Instrumentation and Physical Investigations over a Wide Range of Reynolds Numbers

Polydefkis Bouratsis

Dissertation submitted to the faculty of the Virginia Polytechnic Institute and State University in partial fulfillment of the requirements for the degree of

Doctor of Philosophy
In
Civil and Environmental Engineering

Panayiotis Diplas, Chair
Clinton Dancey, Co-Chair
Thomas Grizzard
Ronald Kriz
Nina Stark

09/29/2014
Blacksburg, VA

Keywords: scour, bridge hydraulics, loose boundary hydraulics, horseshoe vortex, junction flows, physical modelling, underwater photogrammetry, acoustic Doppler velocimeter

Scour at the Base of Bridge Piers: Monitoring Instrumentation and Physical Investigations over a Wide Range of Reynolds Numbers

Polydefkis Bouratsis

ABSTRACT

Hydraulically induced scour of the streambed at the base of bridge piers is the leading cause of bridge failures. Despite the significant scientific efforts towards the solution of this challenging engineering problem, there are still no reliable tools for the prediction and mitigation of bridge scour. This shortcoming is attributed to the lack of understanding of the physics behind this phenomenon. The experimental studies that attempted the physical investigation of bridge scour in the past have faced two main limitations: i) The characterization of the dynamic interaction between the flow and the evolving bed that is known to drive scour, was not possible due to the limitations in the available instrumentation and the significant experimental difficulties; ii) Most of the existing literature studies are based on the findings of laboratory experiments whose scale is orders of magnitudes smaller compared to bridges in the field, while the scale effects on the scour depth have never been quantified.

The objective of this research was to enhance the existing understanding of the phenomenon by tackling the aforementioned experimental challenges. To accomplish this, the first part of this work involved the development of a new underwater photogrammetric technique for the monitoring of evolving sediment beds. This technique is able to obtain very high resolution measurements of evolving beds, thus allowing the characterization of their dynamic properties (i.e. evolving topography and scour rates) and overcoming

existing experimental limitations. Secondly, the underwater photogrammetric technique was applied on a bridge scour experiment, of simple geometry, and the dynamic morphological characteristics of the phenomenon were measured. The detailed measurements along with reasonable comparisons with descriptions of the flow, from past studies, were used to provide insight on the interaction between the flow and the bed and describe quantitatively the mechanisms of scour. Finally, the scale effects on scour were studied via the performance of two experiments under near-prototype conditions. In these experiments the effects of the Reynolds number on the flow and the scour were quantified and implications concerning existing small-scale studies were discussed.

Acknowledgements

I would like to thank those who supported me during the course of my graduate studies, in an academic, financial, or personal level.

First of all, I want to express my gratitude to my academic advisors, Dr. Panayiotis Diplas and Dr. Clinton Dancey, who guided my research efforts and helped me reach my goals. Through their mentorship, they helped me shape my personality and grow as a researcher and an engineer. I am honored to have worked with them.

I would also like to thank the other members of my Ph.D. committee: Dr. Ronald Kriz, Dr. Thomas Grizzard and Dr. Nina Stark, for their valuable comments and suggestions towards the improvement of my dissertation. Additionally, I am thankful to Dr. Kriz for working closer with me during my first steps as a graduate student.

I am happy to have met and worked with my fellow students at the Baker Lab: Nikolaos Apsilidis, Celso Castro Bolinaga, Ozan Celik, Georgios Deskos, Davis Frith, Soonkie Nam, John Petrie, Manousos Valyrakis, and Edgardo Zalaveta. Being their lab-mate and friend has been a real pleasure. Also, special thanks go to the team of the "Prototype-Scale Bridge Scour" project: Jackie Pettway, Glenn Myrick, Julie Cohen and Charles Ellis.

I am grateful for the financial support that was provided to me by the National Science Foundation, the U.S. Army Corps of Engineers, the Gerondelis Foundation, the Edna Bailey Sussman Foundation, the Virginia Water Resources Research Center, the Mechanical Engineering Department and the Graduate School at Virginia Tech.

I want to thank my parents, Amalia and Pantelis, and my brother, George, for their continuous love and support. With their guidance and advice, I will always be able to handle any situation.

Most of all, I am grateful to my beloved wife, Nelie. She has supported me more than anyone else and she has always made me want to be a better person. I am very happy we made this wonderful journey together.

Table of Contents

List of Figures

List of Tables

Chapter 1. Introduction

1.1 Background

More than half of the reported bridge failures in the U.S. have been attributed to the hydraulically induced scour of the streambed at their foundations, typically occurring during flood events [*Briaud*, 1999; *Wardhana*; *Annandale*, 2006; *Melville and Coleman*, 2000; *Shirole and Holt*, 1991]. Some recent examples include: the severe damage of 73 bridges by floods in Pennsylvania, Virginia, and West Virginia, in 1985 [*Mueller*, 1997]; the 1987 failure of the I-90 bridge over Schoharie Creek near Albany, New York, which resulted in the loss of ten lives and millions of dollars for bridge repair/replacement [*Richardson et al.*, 1988; *Richardson*, 1996]; the damage of over 2,400 bridge crossings during the 1993 upper Mississippi River basin flooding [*Parola et al.*, 1997]; the failure of numerous bridges during tropical Storm Alberto in central and southwest Georgia (July 3-7, 1994); and hurricanes Katrina and Rita ruining numerous bridges in New Orleans. Some examples of bridge failures because of scour are shown in Figure 1.

Due to the considerable threats against human lives and the financial losses caused by the damage of the structures and the disruption of the local economy, bridge scour has received great attention from engineers and scientists, over the last decades. Consequently, a vast amount of literature has been published on this subject. The purpose of the scientific efforts is the development of engineering tools for the reliable prediction of the scour depth at the base of existing or new bridge foundations, and the design of countermeasures that can mitigate scour. This has been pursued primarily through the repetitive physical modelling of scour in small-scale laboratory flumes and the derivation of empirical formulae that

express scour depth as a function of the characteristics of the flow and the setup. Most of these empirical formulations were summarized and compared recently by *Sheppard et. al* [2011]. It was shown that formulae, developed from various researchers following similar procedures, estimated significantly inconsistent results for problems with the same geometry and flow characteristics. As expected, many practicing engineers do not trust the existing predicting methods, since they have repeatedly failed to estimate reliably the scour depth in the field [*Richardson and Davis*, 1995]. A recent example involves a study by the United States Geological Survey (USGS) [*Chase and Holnbeck*, 2004] that compared the results of 5 scour prediction equations with field measurements in several sites in Montana, Alaska, Maryland, Ohio, and Virginia. It was found that in most cases the equations overpredicted the maximum scour depth by more than 0.5 m. The tendency of existing empirically derived formulae to overpredict the scour depth has been articulated by many other researchers, as well [*Richardson and Davis*, 1995; *Melville and Coleman*, 2000].

The main reason for the inadequacy of existing methodologies is the lack of understanding of the physical principles behind scour. In particular, scour is the result of a very complex and dynamic interaction between the incoming flow, the hydraulic structure and the evolving sediment bed. Therefore, the great number of investigations that pursued the derivation of strictly empirical formulations, adopted essentially a black-box approach that did not explore adequately the underlying physics behind the phenomenon. To overcome this limitation, recent studies have investigated extensively the flow field topology around hydraulic structures, via small-scale flume experiments, over non-erodible and mobile beds [*Dargahi*, 1989; *Graf and Isiarto*, 2001; *Unger and Hager*, 2008], or via numerical simulations [*Roulund and Sumer*, 2005; *Kirkil and Constantinescu*, 2009; *Kirkil et al.*,

2008, 2009; *Paik et al.*, 2010; *Escauriaza and Sotiropoulos*, 2011]. Despite the progress towards the monitoring of the flow velocities, little has been done for the detailed representation of the erodible bed. Instead, most studies obtained either static representations of the bed or measured the evolving bathymetry of the bed at a single location only [*Oliveto and Hager*, 2002; *Ettema*, 1998; *Melville*, 1999; *Lu et al*., 2011], thus ignoring most of the dynamic morphological features that could provide insight on the physics of the phenomenon. This is mainly attributed to the currently available instrumentation that usually forces researchers to make a compromise between the spatial resolution, temporal resolution or reliability of their measuring techniques.

A very important source of ambiguity in the existing prediction tools is that our understanding is based almost exclusively on the results of physical models that are orders of magnitude smaller than field cases. As a result, the existing models cannot fully satisfy similarity of the scour phenomenon. The very limited, and many times unreliable, data from field sites does not suffice for the successful quantification of the scale effects that are inherent in the majority of the bridge scour literature and provide a distorted description of the phenomenon.

1.2 Research Objectives

The main purpose of this research is to provide insight on the physics behind scour around bridge piers by addressing three main problems that have compromised the effectiveness of existing scientific efforts. The main objectives can be summarized as follows:

1. The development of an experimental technique that can be used for the monitoring of fast evolving beds due to scour. The technique should be able to measure

accurately the 3D morphological characteristics of evolving sediment beds with high spatiotemporal evolution, while being minimally intrusive.

2. The quantitative description of the morphological processes that are observed inside an evolving scour hole, via the application of the new technique. The correlation of these processes with the characteristics of the flow field, as described in previous studies, can enhance the understanding of the main mechanisms that drive scour.
3. The detailed investigation of bridge scour under near-prototype conditions, with measurements of the evolving bathymetry and the flow field over developing scour holes. The comparison of these observations with the findings of smaller scale studies can contribute towards the quantification of the scale effects that limit the effectiveness of existing engineering tools.

Overall, a key characteristic of this work is the emphasis on the very detailed characterization of the dynamic features of scour. The majority of previous bridge scour studies involved the repetitive performance of a large number of experiments aiming to the statistical investigation of one or a few parameters per experiment. On the contrary, the experiments described here were carefully designed and prepared so that the measurements could capture dynamic features that were never quantified before, using state of the art instrumentation and data processing methodologies (i.e. acoustic Doppler profilers, acoustic range-finders, pressure transducers, underwater photogrammetry).

1.3 Organization of the Dissertation

The dissertation consists of three self-contained chapters (Chapters 2 to 4). Every chapter is an original research article that is either published or in preparation for submission to a

scientific journal. Chapter 2 is titled “High-resolution 3D Monitoring of Evolving Sediment Beds” and has been published in the journal Water Resources Research. Chapter 3 is titled “Quantitative Characterization of Scour at the base of a Cylinder” and will be submitted to the journal “Advances in Water Resources”. Chapter 4 is titled “Scour and Flow around Prototype Bridge Foundations” and will be submitted to the Journal of Geophysical Research. The main findings and conclusions from all the chapters are summarized in Chapter 5.

References

Annandale, G. W. (2006), Scour technology : mechanics and engineering practice, xviii, 430 p. pp., McGraw-Hill, New York.

Briaud, J., F. Ting, H. Chen, R. Gudavalli, S. Perugu, and G. Wei (1999), SRICOS: Prediction of Scour Rate in Cohesive Soils at Bridge Piers, Journal of Geotechnical and Geoenvironmental Engineering, 125(4), 237-246.

Chase, K. J., Holnbeck, S. R., Montana., & Geological Survey (U.S.) (2004), Evaluation of pier-scour equations for coarse-bed streams., U.S. Dept. of the Interior, U.S. Geological Survey, Reston, VA

Dargahi, B. (1989), The turbulent flow field around a circular cylinder, Experiments in Fluids, 8(1-2), 1-12.

Escauriaza, C., and F. Sotiropoulos (2011), Initial stages of erosion and bed form development in a turbulent flow around a cylindrical pier, Journal of Geophysical Research: Earth Surface, 116(F3), F03007.

Ettema, R., B. Melville, and B. Barkdoll (1998), Scale Effect in Pier-Scour Experiments, Journal of Hydraulic Engineering, 124(6), 639-642.

Istiarto and Graf, W.H. 2001, Experiments on flow around a cylinder in a scoured channel bed, Int. J. Sediment Res. 16(4), 431-444

Kirkil, G., and G. Constantinescu (2009), Nature of flow and turbulence structure around an in-stream vertical plate in a shallow channel and the implications for sediment erosion, Water Resources Research, 45(6), W06412.

Kirkil, G., S. Constantinescu, and R. Ettema (2008), Coherent Structures in the Flow Field around a Circular Cylinder with Scour Hole, Journal of Hydraulic Engineering, 134(5), 572-587.

Kirkil, G., G. Constantinescu, and R. Ettema (2009), Detached Eddy Simulation Investigation of Turbulence at a Circular Pier with Scour Hole, Journal of Hydraulic Engineering, 135(11), 888-901.

Lu, J., Z. Shi, J. Hong, J. Lee, and R. Raikar (2011), Temporal Variation of Scour Depth at Nonuniform Cylindrical Piers, Journal of Hydraulic Engineering, 137(1), 45-56.

Melville, B., and Y. Chiew (1999), Time Scale for Local Scour at Bridge Piers, Journal of Hydraulic Engineering, 125(1), 59-65.

Melville, B. W., and S. E. Coleman (2000), Bridge scour, xxii, 550 p. pp., Water Resources Publications, LLC, Highlands Ranch, Colo.

Mueller, D. S. (1997), Field-Based Research on Channel Scour at Bridges, paper presented at Proceedings of the U.S. Geological Survey (USGS) Sediment Workshop.

Oliveto, G., and W. Hager (2002), Temporal Evolution of Clear-Water Pier and Abutment Scour, Journal of Hydraulic Engineering, 128(9), 811-820.

Paik, J., and F. Sotiropoulos (2010), Numerical simulation of strongly swirling turbulent flows through an abrupt expansion, International Journal of Heat and Fluid Flow, 31(3), 390-400.

Parola, A. C., Hagerty, D. J., Mueller, D. S., Melville, B. W., Parker, G., and Usher, J. S. (1997), NCHRP Project 12-39 Task Final Report: Highway Infrastructure Damage Caused by the 1993 Upper Mississippi River Basin Flooding, National Cooperative Highway Research Program, Washington, D. C., 195

Richardson, E.V. and Davis, Stan (1995), Evaluating Scour at Bridges, *HEC-18, Federal Highway Administration*, Washington, D.C.

Richardson, E. V. (1996), Historical Development of Bridge Scour Evaluations, paper presented at Proceedings of the North American Water and Environment Congress, ASCE, Anaheim, California.

Roulund, A., B. M. Sumer, J. Fredsøe, and J. Michelsen (2005), Numerical and experimental investigation of flow and scour around a circular pile, Journal of Fluid Mechanics, 534, 351-401.

Shirole, A. M. H. R. C. (1991), Planning for a comprehensive bridge safety assurance program, Transportation research record., 1(1290).

Unger, J., and W. Hager (2007), Down-flow and horseshoe vortex characteristics of sediment embedded bridge piers, Experiments in Fluids, 42(1), 1-19.

Wardhana, K., and F. Hadipriono (2003), Analysis of Recent Bridge Failures in the United States, Journal of Performance of Constructed Facilities, 17(3), 144-150.

List of Figures

Figure 1. Bridge failures due to local scour (adopted from USGS).

Chapter 2. High-resolution 3D Monitoring of Evolving Sediment Beds

Polydefkis Bouratsis*, Panayiotis Diplas, Clinton L. Dancey and Nikolaos Apsilidis

Baker Environmental Hydraulics Laboratory, Virginia Tech, Blacksburg, VA 24061, USA

*Email address: polyb86@vt.edu; Phone number: 540-231-2357

Abstract A new photogrammetric technique has been developed for monitoring the morphology of evolving gravel beds in scour experiments. A pair of commercial cameras is used to record the evolution of the bed and a new computational approach that consists of a set of computer-vision and image-processing algorithms is employed to analyze the videos and reconstruct the instantaneous 3D profile of the bed. Accurate representations of the bed are generated at a rate of 30 profiles/second, with high spatial resolution. The required set up for the implementation of the technique is relatively simple and minimally intrusive. A thorough description of the algorithms that were used and detailed instructions for the implementation of the technique are provided. High-resolution measurements of a gravel bed, in a clear-water, bridge scour experiment were carried out to demonstrate the operation and capabilities of the technique. It is shown that the new technique outperforms existing methods in terms of spatial resolution, temporal resolution, simplicity, cost and applicability.

Keywords *Scour, Computer Vision, Photogrammetry, Bridge Pier, Sediment Transport, Loose Boundary Hydraulics*

2.1 Introduction

2.1.1 Scour Monitoring in Hydraulic Experiments

The study of sediment transport, bedform development and migration, and other erosional/depositional processes in riverine environments are time dependent phenomena that require thorough spatial investigation and continuous monitoring of the morphological characteristics of the river bed. To better understand the interplay between the fluid flow and the erodible boundary, the dynamic nature of these phenomena should be adequately represented. The inspection of the bed at a single, or even infrequent states, provides us with some snapshots that are usually inadequate to piece together the full sequence of events.

Although fairly sophisticated instrumentation is widely used in laboratory experiments to investigate the flow field via point and space, time resolved measurements, over mobile beds [*Hill and Younkin*, 2006; *Zhang et al.*, 2009; *Smith and Nicholas*, 2005; *Bottacin-Busolin et al.* 2008], the technology currently available for monitoring the 3D bed topography evolution of an erodible boundary is sorely lacking.

Regarding scour around in-stream structures, several past studies have focused on the topography of the bed at the equilibrium state only [*Chiew*, 1984; *Dongol*, 1994]. This approach is inadequate because it attempts to describe a time-dependent phenomenon with the state of the bed at a single instant. Furthermore, it has been shown that the duration of flood events is typically too short for the final equilibrium state to be reached [*Melville and Chiew*, 1999; *Mia and Nago*, 2003]. Additionally, time-resolved, 3D measurements of the evolving bed topography are essential for the development and validation of accurate

numerical models that examine the morphodynamics of the bed in cases of fluid-structure interaction [*Escauriaza and Sotiropoulos*, 2011; *Khosronejad et al.*, 2012; *Roulund et al., 2005*] in dam-break flows [*Xia et al*., 2010; *Shakibaeinia and Jin*, 2011], in flows around vegetation [*Liu and Shen*, 2008; *Wu et al.*, 2005], in flows at meandering streams [*Zeng et al*, 2007; *Darby et al.*, 2002] and models that examine the dynamics of bed form creation [*Pelletier*, 2009; *Blondeaux*, 2012]. Also, such data can be used for the investigation of the effectiveness of scour evolution prediction formulae [*Kothyari et al.*, 2007; *Melville and Chiew*, 1999]. Finally, it has been well articulated that topographic data is essential for the development of accurate numerical models that study the flow in riverine environments [*Legleiter et al.*, 2011].

The characterization of the bed topography in past studies was usually subject to significant limitations that compromised the spatiotemporal resolution of the obtained data due to intrusive data collection instrumentation and complicated or expensive set ups. Furthermore, it precluded the capability of taking synchronized measurements of the flow field and corresponding instantaneous scour topography, which could lead to an improved understanding of the coupled, and highly complex, flow-boundary interaction phenomena.

The most common approach to the study of the evolving scour hole is the measurement of the bed elevation at a few locations only. This has been achieved either by employing gages and probes, or other sensors [*Oliveto and Hager*, 2002; *Babu et al.*, 2003; *Fael et al.*, 2006; *Berger et al.*, 2010] or by employing scales that are being recorded by periscopes or cameras inside the transparent walls of the flume or the model [*Mia and Nago*, 2003; *Yanmaz and Altinbilek*, 1991; *Lu et al.*, 2011; *Adduce and La Rocca*, 2006]. Another technique involves the use of probes that are mounted on traversing mechanisms [*Ballio*

and Radice, 2003; *Link et al.*, 2008; *Dargahi*, 1990]. The data obtained with this method may be capable to illustrate synoptically the surface of the bed, though in an asynchronous way. This is a major problem especially during the initial stages of scour around in-stream structures when the rate of bed erosion is very high. Additionally, when the probe is located underwater, it may act intrusively and alter the nature of the phenomenon. Our own experiments have clearly demonstrated the susceptibility of the scour hole characteristics to modest perturbations in the approach flow field. Laser scanners also have been used in sediment transport experiments [*Gonzalez et al.*, 2008]. This method can be successful when the free surface is relatively calm; however, in the vicinity of hydraulic structures, the flow is dominated by surface waves which are diffracting the laser beam. A common approach is the interruption of the experiment and measurement of the bed morphology with mechanical means, such as point-gages [*Rodrigue-Gervais*, 2011], or with more advanced techniques, such as stereo-vision methods [*Umeda et al.*, 2008]. This approach is rather tedious when the bed topography is measured at multiple instants and the disruption of the experiment may introduce disturbances that affect the scouring process. Also, intermittent bed elevation measurements usually involve the assumption that the behavior of the bed during the intermediate periods can be obtained by interpolation. This might not be always correct because the rate of scour may vary over time at different locations.

2.1.2 Time-resolved photogrammetric techniques in hydraulic experiments

Several recent efforts involve the application of photogrammetry for monitoring the surface of the bed or the flow. The basic principle in this methodology is that the precise location of any point detectable in two images, which have been taken from multiple cameras at

different positions, can be estimated. Photogrammetry is well established and it has been widely applied in various areas such as terrestrial mapping, industrial surveying and robotics [*Remondino and El-Hakim*, 2006; *DeSouza and Kak*, 2002; *Band*, 1986]. However, each application has different requirements and the development of suitable techniques for every case, is a material of active research.

Existing photogrammetric applications in hydraulic experiments usually require the use of target points on the monitored surface to provide texture. A common approach is the use of structure light, where a laser or a light projector and optics are combined to create a pattern on the surface. Such an approach was followed by *Foti et al.* [2011] and *Astruc et al.* [2012] who projected a grid on the bed and then estimated the location of the points of the grid. Similarly, *Ankamuthu* [1999], instead of using structure light, placed a set of stones on a sand bed and estimated their location. Also, 2D results were obtained by *Zech et al.* [39] by projecting and recording a laser line on the bed of a laboratory flume in a dam-break flow study. The approach of using targets or particles for texture has also been followed for the reconstruction of the free surface in channels [*Douxchamps et al.*, 2005; *Chandler et al.*, 2008]. These techniques are capable of obtaining accurate, time-resolved measurements of the bed, or the free surface. However, the use of structure light or targets, increases the complexity and the cost of the experimental set-up and compromises the spatial resolution of the measurements, since the elevation of only a few locations of the bed are reconstructed. Also, in applications where the free surface is very unsteady, such as flows around hydraulic structures, the structure light cannot be projected through the free surface and the complexity of the set up is further increased.

Finally, several commercial software for close range photogrammetric applications have been released the last years. The accuracy and the efficiency of these software is constantly improving, however, they exhibit various limitations that prevent their use in scour experiments. These limitations involve the use of targets on the recorded surface, restrictions relative to the orientation of the cameras and their working distance, special illumination requirements, or applicability only on static surfaces.

The main particularities of the application of photogrammetry in hydraulic flumes are: 1) the images of the bed illustrate repetitive patterns and lack of distinctive features, 2) the data collection rate should be sufficiently high to capture the continuously deforming surface, 3) the experiment should not be interrupted, 4) the user does not have physical access to the surface during the experiments, 5) usually, the geometry of the experimental set up does not allow the cameras to be mounted at the ideal distance and orientation. Here we present a new stereo vision based technique for continuous measurements of the bed morphology that overcomes the limitations of the aforementioned techniques. The technique is capable of reconstructing instantaneous surface profiles of the evolving bed with high spatial resolution during scour experiments. Two calibrated cameras are used to record videos of the evolving bed geometry. The technique takes into advantage the texture of gravel beds and does not require the use of targets or structure light. A set of algorithms based on image processing and computer vision principles was used for reconstructing accurately the surface profile of the bed. A code performing the steps of each algorithm was written to analyze the videos on a workstation. The highest temporal resolution of the technique is dictated by the frame rate of the cameras. The technique does not require the interruption of the experiment or the use of additional instrumentation and it can capture

the 3D bed topography nearly non-intrusively. At section 2, an overview of the new technique and the developed algorithms is provided. At section 3, the application of the technique in a bridge scour experiment is described and more details about the algorithm are presented. At section 4, the results of the bridge scour experiment are discussed and the technique is evaluated.

2.2 Overview of the Technique

The experimental procedure of this technique involves the continuous recording of an evolving sediment bed by 2 video cameras. The guidelines for the positioning of the cameras and the tasks that should be carried out during the experiments are mainly described in section 3. In this section an overview of the computational approach that is followed, after the completion of the experiments, to transform the video data to surface profiles of the bed, is explained. The video analysis can be divided into 4 steps, namely the pre-processing, the image processing, the geometrical transformations and the post-processing step. In Fig. 1, a summary of the various steps included in this technique is presented. The inputs, the computations and the outputs at each step are listed. Here, a general description of each step is given and the sequence of the computations shown in Fig. 1 is explained. Some of the photogrammetric principles that are described are well established; however, they have been included here for completeness. The purpose of sections 2 and 3 is to provide adequate information for the repetition of this technique, in any sediment-related experiment

2.2.1 Pre-Processing

After the completion of the experiment and the collection of the videos, the first task of the analysis is the synchronization of the 2 videos so that the time lapse between them is precisely known. Synchronization can be achieved either by using specialized hardware or software, or by creating pulsed light signals that are visible in both videos. Then the frame extraction from the videos follows. In experiments that last for several hours, hundreds of thousands of frames are contained in the videos and the required time for their analysis would be prohibitive, if all of them were processed. Also, in most cases, the rate of the bed deformation is significantly lower than the frame rate of the cameras, especially after the initial phase of scour. Therefore, the user should select the instants that the surface of the bed will be reconstructed and extract the corresponding pairs of frames.

Then the camera calibration is carried out to obtain the parameters that are required to correlate the information contained in the videos with the dimensions of any recorded surface. These consist of the external parameters, which describe the relative position of the two cameras and the internal parameters, which describe the characteristics of each camera [*Hartley and Zisserman*, 2003]. An object whose dimensions are precisely known, the calibration target, needs to be recorded by both cameras simultaneously, at different angles. The camera calibration needs to be performed only once, given that the position of the cameras remains fixed throughout the scour experiment. The recording of the calibration target can take place either prior to the beginning, or after the completion of the experiment. In any case, the calibration target should be recorded while being submerged, to take into account the distortion that is caused by the water. In some of the aforementioned photogrammetric applications, calibration was carried out under drained conditions, thus compromising the accuracy of the final results.

As described in Fig. 1, the output of the first step is the ensemble of the images that will be analyzed and the camera parameters, derived from calibration. From now on the description of the video processing will deal with a single pair of frames obtained at the same instant. The two frames will be referred to, as the left and the right frame, based on the position of the camera that recorded them. The same processing is repeated to analyze the entire set of the extracted pairs of frames.

2.2.2 Image Processing

The second step of the technique involves the processing of the frames and the extraction of the useful information they contain. The application of stereo vision requires that a point of a surface that has been recorded by the two cameras is detectable in both views. If the location of this point in the two frames (pixel coordinates) can be identified, then its location in space (world coordinates) can be estimated, using the calibration parameters. The main objective of the second step of the technique is the detection of the pixel coordinates of the same set of points of the sediment surface depicted in the left and right frames. This procedure is called correspondence establishment. To accomplish this task a correlation-based algorithm was developed. This algorithm divides both frames in small templates and statistically compares them to find the best match. If a comparison satisfies some preselected criteria, then the centers of the respective templates are designated as a pair of correspondences.

Some of the points in the images that will be designated as correspondences are expected to be erroneous, since the statistical comparison is not perfectly effective. However, the frames can be further processed to facilitate the establishment of correspondences between them. If the frames are intensely corrupted by noise, then their properties are altered and

the statistical comparison may yield erroneous results. For this reason, a smoothing filter can be used to mitigate the noise in the images. Usually, an averaging or Gaussian filter can be used for this purpose. The level of the noise depends mainly on the quality of the cameras and the light conditions of the scene during the video recording.

After the image denoising, another type of processing is applied to the frames, called image rectification. In this procedure, the calibration parameters are used to transform geometrically the frames. The rectified frames have been transformed in a way that any two corresponding points of the left and right frame have the same vertical pixel coordinate [*Hartley and Zisserman*, 2003]. This property improves significantly the speed and the performance of the correspondence establishment algorithm. The reason is that every template that has been extracted from one frame, in the correspondence establishment procedure, has to be compared with the templates of the other frame that are located on one horizontal line. This way the comparison of the templates takes place in 1D, instead of 2D space and the computational time is significantly reduced, while the possibility for the establishment of erroneous correspondences is reduced, as well. Therefore, as shown in Fig. 1, the purpose of the image smoothing and rectification is to increase the efficiency of the correspondence establishment process. The output of the second step is a group of pixel coordinates that represent the correspondences between the extracted pairs of frames.

Contrary to the first step, many parameters of the analysis in the second step may vary and the performance of the technique can be optimized after running some trial and error tests. Some of these parameters are the exact statistical criteria of the correspondence establishment, the size of the extracted templates and the type of the denoising filter. The

parameters that optimized the technique in the application that will be described here are listed in section 3.

2.2.3 Geometrical Transformations

All the required inputs for the reconstruction of the surface profiles are obtained in the first two steps. In the third step (Fig. 1), the calibration parameters and the sets of pixel correspondences will be correlated to estimate the world coordinates of these sets of points. The procedure that is followed for this purpose is called triangulation. The result is a cloud of points that represent the bed at the selected instants. The reconstruction that has been accomplished is valid only up to a similarity level. This means that in the cloud of reconstructed points, the ratio of any two lengths can be found, but the value of each length is not known. Also, the cloud of points has been reconstructed in a reference frame that is not convenient for further analysis. Hence, the points should be scaled, rotated and translated to an appropriate coordinate system. This can be achieved by using a set of reference points that are visible in the images and whose position in space must be precisely known.

2.2.4 Post-Processing

In this final step of the technique the reconstructed points are filtered and a surface is fitted to represent the bed at any instant. Some of the points that were designated as correspondences are erroneous and their reconstructions do not belong to the surface of the bed. An outlier removal algorithm is applied here to detect and discard these points. This algorithm consists of the imposition of a global threshold, the segmentation of the bed in smaller sub-areas and the application of 2 local windowing functions that make use of continuity criteria. For the outlier removal step, it is assumed that the erroneous points are

few compared to the ensemble of the data (less than 20% usually) and that their location in space is not biased. It should be noted here that the combination of the correspondence establishment and the outlier removal steps, as applied here, make the use of structure light or other targets on the bed, unnecessary.

Finally a surface is fitted to the points after the outliers have been removed. In general, various approaches can be followed for the surface fitting procedure. If there is confidence that almost all the outliers have been removed, then linear interpolation can be adequate for the representation of the bed topography. However, if some outliers remain in the processed data, then a robust fitting technique should be adopted instead (e.g. Lowess statistical test) [*Ott and Longnecker*, 2010]. The user should carry out visual inspection of the final results to determine the most appropriate surface fitting approach. In the following section, the application of the technique in a bridge scour experiment is described and more details on the proposed computational approach are discussed.

2.3 Bridge scour experiment

The presented technique was applied to monitor the evolving topography of a sediment bed in a scour around a bridge pier experiment. The detailed steps that were followed for the implementation of the technique are described here. Scour around bridge foundations is a phenomenon where the evolution of the bed morphology is of great importance. The examination of the evolution of the scour depth, the shape of the scour hole and the rates of scour has been pursued in the past with methods that suffered from the limitations that were described in section 1. It is shown here that the presented technique is very suitable for bridge scour experiments and it can be used to provide insight for the study of this phenomenon.

2.3.1 Experimental set up and data collection

The experiment was carried out in a tilting flume, with dimensions16.2x1.2m, located in the Baker Environmental Hydraulics Laboratory of Virginia Tech. The slope of the bed was set to 0.0005 and the sediment was gravel with d_{50}=0.355cm and d_{90}=0.47mm. The model pier was a plexiglass cylinder with diameter D=15.24cm. A view of the flume and the model pier is shown in Fig. 2. The approach flow depth was 20.5cm and the mean velocity was 62cm/s. The experiment was performed under clear-water scour conditions. Two Olympus Stylus Tough-6020 waterproof cameras were used to record the scour hole evolution. The cameras were recording at a rate of 30 frames/second and the resolution of the videos was 720x1280 pixels. The dimensions of each camera were 10cm x 6.5cm x 2.6cm. The cameras were firmly mounted on the side walls of the flume and were submerged during the experiments. The technique does not require that the cameras be submerged; however, the largest part of the scour hole was occluded when viewed through the transparent side walls of the flume. Furthermore, recording the bed evolution through the free surface was not feasible due to the presence of surface waves.

Preliminary tests determined that the resolution of the cameras was sufficient to provide videos of high quality that satisfy the requirements of the technique. In general, it is recommended that the videos are recorded in high definition (HD). The basic criteria for the choice of the cameras were their size, shape and angle of view. When submerged, the size of the cameras should be small and the shape should allow a steamlined positioning during the experiments, to minimize intrusiveness. Based on the distance of the cameras from the bed and the size of the surface that is recorded, the minimum required angle of view of the cameras should be estimated. In general, wide-angle lenses should be avoided

because they introduce severe distortion that is hard to be taken into account. The use of cameras with higher frame rate and resolution, or special lenses can increase the efficiency of the technique, in terms of spatial resolution, temporal resolution and accuracy; however, the current experiments showed that low-cost, charged-coupled device (CCD), commercial cameras can provide high quality data. Also, it was found that the level of noise in the videos was relatively low and it could be adequately removed with a simple filtering procedure. Since the technique was not tested with a wide range of cameras, a conclusive description of the minimum requirements of their specifications cannot be provided here.

The fixture that was built to hold the cameras consisted of 2 optical posts and 4 knuckles. The knuckles allowed the rotation of the cameras by 360^{o}. Preliminary tests showed that the fixture could keep the cameras steady, without any change in orientation caused by the flow or vibration. In order to achieve the optimum performance, the cameras were positioned in a way that their common field of view was maximized and the angle between the plane of their lenses and the bed was minimized. In general, when submerged, the cameras should be as far as possible from the test section to minimize the intrusiveness of the technique. Fig. 3 illustrates the position of the cameras during the experiments and the fixture that was mounted on the side walls of the flume to hold the cameras. For the current experiments, the cameras were 36cm (2.4xD) away from the pier and their horizontal distance from the edge of the scour hole at the end of the experiment was 21.5cm (1.4xD). The cameras were oriented in way that their smallest dimension was perpendicular to the direction of the flow as it is shown in Fig. 3. Prior to the experiments a set of dots was carefully drawn on the surface of the pier, with their location being precisely known. The dots, which were visible by both cameras during the experiments, served as reference

points for the coordinate transformation step and are the only required targets for this technique. Preliminary experiments showed that the performance of the technique depends greatly on the light conditions at the test section; two 100W lamps were mounted on the flume to illuminate the bed.

At first, the flume was very slowly filled with water, to ensure that scour did not take place. The depth of the water was increased to cover the cameras, using the tailgate of the flume. Then the cameras started recording. A laser pointer was used to create light pulses, which were used later for the synchronization of the videos. A 6.35x8.16x0.2 cm checkerboard was submerged at the text section, to serve as the calibration target. The checkerboard was relocated several times under water to be recorded from different angles by the cameras, as it is shown in Fig. 4. The technique requires that the videos of the calibration target are taken while it is submerged. Then, the checkerboard was removed and the flow rate was slowly increased to reach the desired conditions. Scour evolved continuously and was recorded for the duration of the experiment, which was 250 minutes.

2.3.2 First stage of the analysis

The videos were imported in a workstation and the steps described in Fig. 1 were followed to analyze the data and reconstruct the morphology of the evolving bed. At first, the exact frame lapse between the two videos was found by observing the recorded laser light signals; the lapse was 11 frames. Then, a set of 74 frames was extracted from each camera. Eighteen pairs of frames were used as images of the calibration target and were recorded before the commencement of the experiment. In Fig. 4, the frames that were used for the calibration of one camera are shown. The rest 56 pairs of frames were images of the bed at selected instants throughout the experiment. One pair of such frames is presented in Fig.

5a. The "Camera Calibration Toolbox for Matlab®" [*Bouguet*, 2010] was used to carry out the calibration of the stereo system. The Toolbox is using the corners of the squares of the checkerboard, as they appear in the images to estimate the internal and external calibration parameters of the stereo system that will be used in a subsequent step of the technique. The cameras need to be calibrated only once, since their position did not change throughout the experiments.

The estimated external calibration parameters are a 3x3 rotation matrix (**R**) and a 3x1 translation vector (**T**) that describe the relative position of the 2 cameras. The estimated internal calibration parameters are a calibration matrix ($\mathbf{C_i}$) and a vector of distortion coefficients ($\mathbf{k_{ci}}$) for each camera (*i*). The internal parameters **C** and $\mathbf{k_c}$ are defined in Equations (1) and (2), respectively.

$$\mathbf{C_i} = \begin{bmatrix} f_{xi} & 0 & c_{xi} \\ 0 & f_{yi} & c_{yi} \\ 0 & 0 & 1 \end{bmatrix} \quad (1)$$

$$\mathbf{k_{ci}} = \begin{bmatrix} k_{1i} & k_{2i} & p_{1i} & p_{2i} & k_{3i} \end{bmatrix} \quad (2)$$

In Equation (1), f_x and f_y describe the focal length in terms of horizontal and vertical pixels and c_x and c_y are the pixel coordinates of the principal point. In Equation (2) k_1, k_2 and k_3 are the radial distortion coefficients and p_1 and p_2 are the tangential distortion coefficients. The explanation of the calibration procedure and the calibration parameters is out of the scope of this manuscript. The reader is referred to *Bouguet* [2010] and to *Hartley and Zisserman*, [2003] for a detailed description of these parameters.

2.3.3 Second stage of the analysis

All the extracted frames were transformed to gray-scale images and a smoothing Gaussian filter was applied to them, to mitigate the noise. Since the images were not severely corrupted by noise and to avoid the distortion of their features, the standard deviation and the window size of the Gaussian filter were relatively small [*Gonzalez and Woods*, 2008]. The smoothened images were then rectified making use of the estimated calibration parameters. The image rectification was carried out using the Camera Calibration Toolbox for Matlab® [*Bouguet*, 2010].

In Fig. 5a, two coincident raw frames, recorded from the left and the right cameras, are shown. In Fig.5b, the same frames are shown after being filtered and rectified. Four corresponding points of the bed have been marked with dots in the left and right frames of Fig. 5b. It is shown that the correspondences of the two images with pixel coordinates (x_{p1},y_{p1}) in the left image and (x_{p2},y_{p2}) in the right image, lie on the same horizontal line, so that $y_{p1}=y_{p2}$. Since the necessary manipulation of the images has been completed, the remaining task for the second stage of the technique is the establishment of correspondences for every extracted pair of frames.

The code that was developed for the automated establishment of correspondences is a correlation-based algorithm, which is appropriate for images that lack distinctive features, such as edges, corners or color discontinuities [*Shapiro and Stockman*, 2001]. The procedure is the same for every pair of frames. Templates of size 35x35 pixels were extracted from the left image. The distance between the centers of the templates was 9 pixels in the horizontal and the vertical direction. The correspondence of the center of each extracted template was found by carrying out normalized cross-correlation between the

gray-scale intensity of the pixels of the template and the right image. However, since the images were rectified, the cross-correlation had to be performed on a horizontal line only. Therefore, each template from the left image had to be compared with a window of the right image with dimensions 35x1280 pixels, where 1280 pixels is the width of the images. If the images were not rectified, the templates would have to be compared with the entire right image, with dimensions 720x1280 pixels. Additionally, visual inspection was performed to narrow the width of the extracted windows from the right image. The first and the last extracted pairs of frames were visually examined and a few correspondences were identified. Then the horizontal coordinates (x_1 and x_2) of the correspondences were compared and a value for the maximum and the minimum horizontal disparity was determined. It was found that the size of the extracted windows can be decreased to 35x500 pixels. The step of visual inspection for the estimation of the disparity limits increases even more the speed of the calculations; however, it is not mandatory for the application of the technique. The normalized cross correlation was carried out using the following expression by Lewis [1995]:

$$\mathbf{g}(x_t, y_t) = \frac{\sum_{x_w, y_w} [\mathbf{f}(x_w, y_w) - \overline{f_{x_t, y_t}}][\mathbf{t}(x_w - x_t, y_w - y_t) - \bar{t}]}{\left\{ \sum_{x_w, y_w} [\mathbf{f}(x_w, y_w) - \overline{f_{x_t, y_t}}]^2 \sum_{x_w, y_w} [\mathbf{t}(x_w - x_t, y_w - y_t) - \bar{t}]^2 \right\}^{0.5}} \qquad (3)$$

Where **g** is the result of the normalized cross-correlation, **f** is a matrix containing the pixels of the window from the right image with coordinates ($\mathbf{x_w, y_w}$), **t** is a matrix containing the pixels of the template of the left image with coordinates ($\mathbf{x_t, y_t}$), $\bar{t}$ is the mean value of the pixel intensities of the template and $\overline{f}$ is the sum of the pixel intensities of the window in

the region under the template. The position (x_w,y_w) where the normalized cross-correlation was maximized, was designated as a candidate correspondence, if the value of the normalized cross correlation was over the threshold value of 0.3. If the result of Equation (3) was always lower than the threshold, then no correspondence was found for the specific template. If the normalized cross-correlation was maximum in more than one location in the respective window, then the sum of absolute differences was carried out at those locations to select the location of the candidate correspondence. This procedure was repeated for all the extracted templates of the left image and a set of candidate correspondences was found in the right image.

The described procedure is visually demonstrated in Fig. 5b for 4 points. It is shown that templates centered at those points are extracted from the left figure and cross-correlated with the windows of the right frame, located on the same horizontal line. The location where the normalized cross-correlation was maximized is marked on the right image of Fig. 5b. In Fig. 6 the result of the normalized cross-correlation between the template and the window that are located in the lowest position in Fig. 5b is presented. The location of the maximum value in Fig. 6 is marked in the respective window of Fig. 5b as a candidate correspondence. In Fig. 6, it is also shown that there are only 6 locations where the result of the normalized cross-correlation is higher than the threshold value.

For verification, an inverse procedure was followed; 35x35 pixel templates were extracted from the right image, centered at the locations of the candidate correspondences. These templates were cross-correlated with windows from the left image and a second set of candidate correspondences was found in the left image. The coordinates of the candidate correspondences in the left image were compared with the coordinates of the centers of the

templates that were initially extracted from the same image. The candidate correspondences in the left image that were less than 3 pixels away from the center of the respective templates of the same image were designated as final correspondences; all the other candidate correspondences were discarded.

Fig. 7 shows the location of all the final correspondences in the left and right images of Fig. 5b. It can be observed that there are some areas of the bed where no correspondence could be found. Regions without successful correspondence are possible since some of these areas do not belong to the common field of view of both cameras (e.g. at the edge of the images), or the plane of the bed at these areas is almost parallel to the cameras' viewing axes and its features appear to be distorted. In Fig. 7, the number of the identified correspondences is 7517 and the area of the bed is approximately 370 cm^2.

It should be noted that most of the parameters of the correspondence establishment algorithm, such as the number and the size of the templates, the threshold value for the normalized cross-correlation, or the maximum allowed distance between the center of a template and the respective candidate correspondence in the same image, were chosen based upon experimenting with the algorithm.

In general, the templates should be large enough to include an area of the image with adequate variability, in terms of pixel intensities; otherwise, the correlation magnitudes are expected to be very low. Therefore, more than one sediments should be included in every template. However, if the area of the template is very large then the possibility for the establishment of erroneous correspondences is increased. Also, larger templates increase the required computational time. As far as the distance between the centers of the templates is concerned, smaller distances result to more templates and consequently increase the

spatial resolution of the technique. The highest spatial resolution can be achieved if one template is extracted for every pixel of the image. In the current experiments, where every sediment was represented by 10-40 pixels, approximately, the extraction of one template / pixel would be superabundant. The computational time of the correspondence establishment algorithm is proportional to the number of the extracted templates. Regarding the selection of the threshold cross-correlation magnitude and the maximum allowed distance in the verification procedure, no general rule can be stated. Here, these parameters were selected after a trial and error procedure and the subsequent visual inspection of the results. Overall, the size of the sediments, the distance of the cameras from the bed, the cameras' resolution and the desired spatial resolution should be taken into account when selecting the parameters of the second step of the technique. Also, it was found that the performance of this algorithm depends on the orientation of the cameras and the light conditions during the experiments. Although most of the steps of this technique (Fig. 1) can be applied almost unchanged for any application, the correspondence establishment step requires preliminary experiments for the determination of the optimum set up and the parameters that should be used.

2.3.4 Third stage of the analysis

After the completion of the first 2 stages of the technique all the required inputs from the videos have been extracted. The calibration parameters and the set of correspondences are used in the third stage of the technique to reconstruct a cloud of points that represent the bed at each instant. Here, the procedure that is followed for the reconstruction of the world coordinates of a single point of the bed is explained. The algorithm that was used here is based on well known concepts that are primary components of most photogrammetric

applications; however, the computations are described here for completeness purposes. The pixel coordinates of every correspondence, $\mathbf{x_d}$, that was found in the previous step are written in a homogeneous representation, so that $\mathbf{x_{di}}=[x_{di}\ y_{di}\ 1]^{\tau}$; where, x_d and y_d are the horizontal and vertical pixel coordinates respectively, i=1,2, denotes the left and right view respectively and τ denotes the transpose matrix. First, the homogeneous pixel coordinates of every correspondence are normalized in Equation (4) using the calibration matrices defined in Equation (1) [*Hartley and Zisserman*, 2003].

$$\mathbf{x_{hni}} = \mathbf{C_i}^{-1} \times \mathbf{x_{pi}} \tag{4}$$

Where $\mathbf{x_{hni}}=[x_{ni}\ y_{ni}\ 1]$ are the homogeneous, normalized, pixel coordinates. Then, the inhomogeneous normalized pixel coordinates, $\mathbf{x_{ni}}=[x_{ni}\ y_{ni}]$, are corrected for distortion in Equation (5) using the distortion vectors of Equation (2) [*Bouguet*, 2010].

$$\mathbf{x_{ui}} = \frac{(\mathbf{x_{ni}} - \boldsymbol{\delta}_\mathbf{t})}{\delta_r} \tag{5}$$

Where $\mathbf{x_{ui}}=[x_{ui}\ y_{ui}]$, are the undistorted pixel coordinates and $\boldsymbol{\delta}_\mathbf{t}$, δ_r and r are defined in Equations (6), (7) and (8).

$$\boldsymbol{\delta}_\mathbf{t} = \begin{bmatrix} 2p_{1i}x_{ni}y_{ni} + p_{2i}(r_i^2 + 2x_{ni}^2) \\ 2p_{2i}x_{ni}y_{ni} + p_{1i}(r_i^2 + 2y_{ni}^2) \end{bmatrix} \tag{6}$$

$$\delta_{ri} = 1 + k_{1i}r_i^2 + k_{2i}r_i^4 + k_{3i}r_i^6 \tag{7}$$

$$r_i = \sqrt{x_{ni}^2 + y_{ni}^2} \tag{8}$$

The external orientation matrix of each camera, $\mathbf{o_i}$, is defined in Equation (9) using the external calibration parameters.

$$\mathbf{o_1} = \begin{bmatrix} \mathbf{I_3} & \mathbf{0_{3,1}} \end{bmatrix} \qquad \mathbf{o}_2 = \begin{bmatrix} \mathbf{R} & \mathbf{T} \end{bmatrix} \tag{9}$$

Where $\mathbf{I_3}$ and $\mathbf{0_{3,1}}$ are a 3x3 identity matrix and a 3x1 zero vector, respectively. Then the Direct Linear Transformation is applied to the undistorted pixel coordinates as described by *Hartley and Zisserman* [2003]. For every point found in both views, a new matrix (**A**) is defined as in Equation (10).

$$\mathbf{A} = \begin{bmatrix} x_{u1}o_1^{3\tau} - o_1^{1\tau} \\ y_{u1}o_1^{3\tau} - o_1^{2\tau} \\ x_{u2}o_2^{3\tau} - o_2^{1\tau} \\ y_{u2}o_2^{3\tau} - o_2^{2\tau} \end{bmatrix} \tag{10}$$

Where $\mathbf{o_i^{j\tau}}$ is the j[th] row vector of the i[th] orientation matrix. Matrix **A** is being factorized to three matrices (**U, Σ, V**) through Singular Value Decomposition (SVD), so that $\mathbf{A}=\mathbf{U\Sigma V^{\tau}}$. The world coordinates of the point of the bed, $\mathbf{x}=[x\ y\ z]$, that is related to the pair of correspondences found in the 2 views, are defined in Equation (11).

$$x=\mathbf{V}^{1,4}, y = \mathbf{V}^{2,4}, z = \mathbf{V}^{3,4} \tag{11}$$

Where, $V^{j,k}$ is the element of the matrix **V** that is located on the j[th] row and the k[th] column. Finally, the estimated world coordinates need to be transformed to a convenient reference system. The coordinate transformation involves the rotation, the translation and the scaling of the coordinates, as shown in Equation (12).

$$\mathbf{x_c} = s_c(\mathbf{R_c}\mathbf{x}^{\tau} + \mathbf{t_c}) \tag{12}$$

Where $\mathbf{x_c}=[x_c\ y_c\ z_c]$, are the transformed world coordinates, s_c is a scale factor, $\mathbf{R_c}$ is a 3x3 rotation matrix and $\mathbf{t_c}$ is a 3x1 translation vector. The estimation of s_c, $\mathbf{R_c}$ and $\mathbf{t_c}$ is carried out using the reference points that were marked on the cylinder. The world coordinates of the reference points, in the desired reference system, should be physically measured. Then those points are reconstructed following the steps of this technique. The aforementioned parameters can be estimated by comparing the physically measured coordinates with the reconstructed coordinates, rearranging Equation (12) and minimizing it with a least-squares method. The procedure that was explained here is followed for all the correspondences of both views at the selected instants. The reconstructed points with coordinates equal to $\mathbf{x_c}$, are further processed at the final step of the technique.

2.3.5 Fourth stage of the analysis

Despite the filtering and the constraints that were imposed in the second stage of the technique, it is expected that some of the established correspondences are invalid. Therefore, some of the points that were reconstructed in the third stage are erroneous and need to be removed. For this reason, an outlier removal algorithm was developed. At first, a global threshold was applied to the reconstructed points. The global threshold removed points with negative elevation, points with elevation greater than that of the gravel bed before the commencement of the experiment, and points whose horizontal distance from the cylinder was higher than the expected field of view. Then, a local windowing function was applied at the vicinity of each reconstructed point. Areas of $1cm^2$ that were centered about each reconstructed point were defined. A planar surface was fitted to the points of each area using a least-squares method. Then points whose distance from this surface was greater than 3mm, which is on the order of a sediment diameter, were marked as outliers

and were discarded. The selection of this criterion was made based on the assumption that every $1cm^2$ of the bed has an almost uniform slope.

The remaining points were segmented to a few (7-10) sub-areas with horizontally neighboring points based on their elevation and its gradient. Points whose elevation was greater than two standard deviations of the mean elevation of each sub-area were marked as outliers and were discarded. In Fig. 8, the reconstruction of the points that were found in Fig. 7 is presented. Also, the identified outliers are highlighted in Fig. 8. It is shown that the number of the erroneous points is low compared to the number of the reconstructed points (approximately 5%). Obviously, the performance of the outlier removal algorithm is improved when the percentage of the erroneous reconstructed results is small. Finally, a surface was fitted by applying linear interpolation at the reconstructed points that represent the bed at a given instant, after the removal of the outliers. Other methods can be adopted for the surface fitting step, as well. The surface that was fitted to the valid points of Fig. 8 is presented in Fig. 9. The entire procedure that was explained above can be applied to reconstruct the bed at any instant as in Fig. 9.

2.4 Discussion

2.4.1 Further analysis

Some of the results of the bridge scour experiment are presented in this section. The focus here is on the demonstration of the capabilities of the technique, rather than the findings of the experiment. Some of the information that can be extracted with the use of the presented technique is underlined. A detailed presentation of the results will be included elsewhere [*Bouratsis et al.*, manuscript in preparation].

The bed topography can be reconstructed in detail as shown in Fig. 10, where the reconstructed profile of the scour hole 120 minutes after the commencement of the experiment is presented. In Fig. 10, which is representative of all the profiles that were reconstructed, every $1cm^2$ of the bed is represented by 17 independent point-wise elevation measurements, on average. As it was mentioned above and shown in Fig. 9, part of the scour hole was occluded and could not be reconstructed. For the result of Fig. 10 symmetry was assumed along the centerline of the flume. It is shown that the detailed morphological characteristics of the bed can be found at any instant. In Fig. 10 the average slopes of the front, side and rear parts of the pier are highlighted. In several bridge scour studies it is assumed that the slope of the scour hole is uniform and equal to the angle of the sediment repose; however, here it is shown that the slope varies around the pier. This technique allows the determination of the local slope at any location within the scour hole. The reconstruction of the bed profile at consecutive instants can be used for the development of a video-representation of the scour evolution. To the best of our knowledge, this is the first time that such detailed information about the geometric characteristics of a scour hole have been obtained from experiments.

In Fig. 11 the profiles of the part of the scour hole that is located 0-2.25cm away from the surface of the pier, at different instants, are plotted. A comparison of the scour evolution, at the front and the sides of the pier, during the first 30 minutes of the experiment is made. It is shown that scour starts at the sides of the pier and that for the first 2 minutes the elevation at the front part of the scour hole remains unchanged. Also, it can be observed that the scour rate of the bed at the perimeter of the pier is rapidly decreasing. A more thorough description of the temporal and spatial evolution of the scour rates is illustrated

in Fig. 12. It is shown that the scour rates vary greatly at different instants. The intense scour activity at the sides of the pier during the first 5 minutes of the experiment is highlighted. After that, scour becomes dominant at the front and back of the pier. The development of the scour rates fluctuates with time, since they are higher at the 30^{th} minute than at the 20^{th} minute of the experiment. This analysis can be useful for the investigation of the impact of the horseshoe vortex activity on bed scour. Finally, from Fig. 9 and 10 it can be concluded that point-wise measurements at arbitrarily chosen locations cannot characterize successfully the phenomenon. Instead, the current technique can provide quantitative measurements of the temporal evolution of the shape, the size, the excavated volume and the scour rates of the entire scour hole as well as at specific locations.

2.4.2 Accuracy

The sources of error of this technique are associated with (1) the camera calibration, (2) the establishment of correspondences and (3) the surface fitting. Any camera calibration procedure can estimate the internal and external camera parameters only up to a specific accuracy. Therefore, the inputs of the stereo triangulation step are expected to contain error which is propagated to the subsequent steps. Additionally, even after the outlier removal step it is possible that some of the reconstructed points may have resulted from erroneous correspondences. Finally, some error is expected to be induced by interpolation during the surface fitting step.

Two tests were carried out to investigate the accuracy of the technique. The first test involved the reconstruction of a Rubik's cube with known dimensions (Fig. 13a). The cube was positioned at the test section of the flume and the cameras were located at the same position as in the bridge scour experiment. The calibrated cameras took videos of the cube

and a pair of frames was extracted. Then, the pixel coordinates of the edges of the cube were manually detected, without applying the correspondence establishment algorithm. Finally, the cube was reconstructed applying the stereo triangulation algorithm and the coordinate transformation process. The result is shown in Fig. 13b. It was found that the error of the reconstruction was less than 1% of the side length of the cube. It can be concluded that the error associated with the camera calibration is negligible for the purpose of this technique.

The second test involved the verification of the bed profile measurements with a point-gage. All the steps of Fig. 1 were followed to analyze videos of the bed at a semi-equilibrium state. Then the flume was carefully drained and the bed elevation was measured with a point gage at 30 locations. The residuals of the verification measurements from the reconstructed profile were subsequently determined. It was found that the range of the error at the vicinity of the reconstructed points was 2mm, which is less than 1 grain diameter. It is expected that smaller grain diameters will result to a better accuracy.

2.4.3 Evaluation of the computational approach

For the implementation of this technique a set image processing and stereo-vision algorithms were used. The main advantage of this computational approach, compared to the photogrammetric techniques that were listed at the first section, is the combined use of an exhaustive correspondence establishment and a robust outlier removal algorithm. The basic concept here is that in the establishment of correspondences the texture of the gravel bed is being exploited to establish as many matches as possible between coincident views, taking into consideration that some of these matches are erroneous. Then, the erroneous matches are identified in the outlier removal step that relies on the continuity of the bed.

These 2 steps and the rectification step, allow for the detection of a significantly high number of matches to be found in every pair of coincident frames, resulting to the highest spatial resolution that has been reported in time-resolved, scour experiments (1 measurement/ 6mm^2).

This technique is relatively computationally expensive. This is due to the fact that the task of establishing correspondences here is far more difficult, than in the cases where a structure light is employed. The more advanced computations allow for the use of much simpler and less expensive instrumentation, without compromising the accuracy of the profiles. Therefore, this technique is applicable to a wide range of scour related experiments, with gravel or coarse sand beds. However, the reconstruction of fine sand beds with this technique is expected to be more difficult, since the absence of texture would be more evident.

Finally, the choice of the calibration algorithm that was used here, allows for a relatively free positioning of the cameras, for the correction of distortion and for the rectification of the images in a simple manner.

2.4.4 Modifications of the technique

The technique can be applied with various changes or additions according to the objectives of the experiment. One possibility is the use of more than 2 cameras to increase the size of the reconstructed surface. In this case, all the aforementioned stages will be followed for the overlapping regions of pairs of cameras. Also, high-speed cameras or still cameras can be used according to the expected rate of bed evolution which dictates the desirable frame rate. The cameras do not have to be submerged. Preliminary tests showed that the technique performed equally well when the cameras were recording through the transparent side

walls of the flume; however, the sediment bed in the present experiments did not allow for a clear view of the entire scour hole. Furthermore, a structured light approach can be followed. This could be useful in experiments where the bed elevation needs to be measured at a few locations only, or experiments with very fine sand. Such a modification is expected to improve the accuracy of the technique, but decrease the spatial resolution. Finally, it is worth mentioning that for each case some of the parameters of the algorithm need to be determined through a trial and error procedure and by considering the objectives of the specific application. Those parameters are associated with the correspondence establishment, the outlier removal and the surface fitting algorithms.

2.5 Conclusions

A new technique for obtaining uninterrupted, instantaneous, highly detailed, 3D representations of the evolving bed topography in scour experiments has been presented. The technique requires the use of two relatively freely positioned cameras that record the sediment bed during the experiment. The computational approach employed for the analysis of the video frames has been elaborated. The video analysis follows the sequence that is described in Fig. 1 and consists of a pre-processing, an image processing, a geometrical transformation and a post-processing step. The analysis that is carried out at each stage was described and detailed instructions for the application of the technique were provided, both in terms of the experimental set up and the processing of the data. New algorithms were developed for establishing correspondences between coincident frames and removing outliers. Additionally, a number of well established algorithms were incorporated here to carry out the tasks of camera calibration, image rectification and stereo-triangulation. Overall, the combined use of appropriately chosen algorithms resulted

to a new methodology for generating 3D image reconstruction of the bed, in hydraulic flumes at high spatial and temporal resolution.

The application of the technique in a bridge scour experiment has been presented to provide a better understanding of its operation and its capabilities. The instantaneous morphology of the evolving scour hole, here, can be obtained at a rate of 30 profiles/second. The coordinates of more than 7000 points of the scour hole were estimated and used to characterize the bed profile at every instant. The accuracy that was achieved was lower than 1 grain diameter. It is shown that the results of this technique can be further analyzed to provide a quantitative description of the shape of the scour hole, the slope and the scour rates as they vary with time.

The present technique overcomes several limitations of prior methods by allowing for continuous and nonintrusive scour measurements. The technique does not require the use of targets on the bed, structure light or advanced cameras. The relatively simple methodology and low-cost set up have the potential to make this technique applicable to a wide range of experiments and easily combined with other instrumentation for the measurement of the flow field. The main objective of the present work was to develop a method that can be routinely used to visualize the surface of evolving gravel beds and obtain data of high quality. Several adjustments can be made to accommodate the needs of various applications.

Acknowledgements

The authors would like to thank the National Science Foundation (EAR 0738759) and the Research Office of the United States Army Corps of Engineers (ARO 53512-EV) for their support for this study.

References

Adduce, C., and M. La Rocca (2006), Local scouring due to turbulent water jets downstream of a trapezoidal drop: Laboratory experiments and stability analysis, *Water Resour Res*, *42*(2).

Ankamuthu, S., R. Balachandar, and H. Wood (1999), Computational stereoscopy for three-dimensional scour depth measurement in channels, *Can J Civ Eng.*, *26*(6), 698-712.

Astruc, D., S. Cazin, E. Cid, O. Eiff, and L. Lacaze (2012), A stereoscopic method for rapid monitoring of the spatio-temporal evolution of the sand-bed elevation in the swash zone, *Coast Eng* (Amsterdam), *60*, 11-20.

Babu, M. R., V. Sundar, and S. N. Rao (2003), Measurement of scour in cohesive soils around a vertical pile-simplified instrumentation and regression analysis, *IEEE J Ocean Eng*, *28*(1), 106-116.

Ballio, F., and A. Radice (2003), A non-touch sensor for local scour measurements, *J Hydraul Res*, *41*(1), 105-108.

Band, L. E. (1986), Topographic Partition of Watersheds with Digital Elevation Models, *Water Resour Res*, *22*(1), 15-24.

Berger, C., B. W. McArdell, B. Fritschi, and F. Schlunegger (2010), A novel method for measuring the timing of bed erosion during debris flows and floods, *Water Resour Res*, *46*(2).

Blondeaux, P. (2012), Sediment mixtures, coastal bedforms and grain sorting phenomena: An overview of the theoretical analyses, *Adv Water Resour*, http://dx.doi.org/10.1016/j.advwatres.2012.02.004.

Bouguet, J. Y. (2004), Camera calibration toolbox for matlab, http://www.vision.caltech.edu/bouguetj/calib_doc/2010.

Bottacin-Busolin, A., S. J. Tait, A. Marion, A. Chegini, and M. Tregnaghi (2008), Probabilistic description of grain resistance from simultaneous flow field and grain motion measurements, *Water Resour Res*, *44*(9).

Chandler, J.H., R. Wackrow, X. Sun, K. Shiono and P. Rameshwaran (2008), Measuring a dynamic and flooding river surface by close range digital photogrammetry, paper presented at Silk Road for Information from Imagery, International Society for Photogrammetry and Remote Sensing, Beijing, China, 211-216.

Chiew, Y.M. Local scour at bridge piers. PhD Dissertation, The University of Auckland, New Zealand.

Darby, S. E., A. M. Alabyan, and M. J. Van de Wiel (2002), Numerical simulation of bank erosion and channel migration in meandering rivers, *Water Resour Res*, *38*(9).

Dargahi, B. (1990), Controlling Mechanism of Local Scouring, *J Hydraul Eng* (New York, N.Y.), *116*(10), 1197-1214.

DeSouza, G. N., and A. C. Kak (2002), Vision for mobile robot navigation: a survey, *IEEE Trans Pattern Anal Mach Intell*, *24*(2), 237-267.

Dongol, D.M.S. (1994), Local scour at bridge abutments, PhD Dissertation, The University of Auckland, New Zealand.

Douxchamps, D., D. Devriendt, H. Capart, C. Craeye, and B. Macq (2005), Stereoscopic and velocimetric reconstructions of the free surface topography of antidune flows, *Exp Fluids*, *39*(3), 535-551.

Escauriaza, C., and F. Sotiropoulos (2011), Initial stages of erosion and bed form development in a turbulent flow around a cylindrical pier, *J Geophys Res*, *116*(f3).

Fael, C. M. S., G. Simarro-Grande, J.-P. Martin-Vide, and A. H. Cardoso (2006), Local scour at vertical-wall abutments under clear-water flow conditions, *Water Resour Res*, *42*(10).

Foti, E., I. Caceres Rabionet, A. Marini, R. E. Musumeci, and A. Sanchez-Arcilla (2011), Experimental investigations of the bed evolution in wave flumes: Performance of 2D and 3D optical systems, *Coast Eng* (Amsterdam), *58*(7), 606-622.

Gonzalez, R. C., and R. E. Woods (2008), *Digital image processing*, Prentice Hall, Upper Saddle River, N.J.

Gonzalez, E. P., J. Femarques, F. S.-T. Diaz-Pache, J. P. Agudo, and L. C. Gomez (2008), Experimental validation of a sediment transport two-dimensional depth-averaged numerical model using PIV and 3D Scanning technologies, *J Hydraul Res*, *46*(4), 489-503.

Hartley, R., and A. Zisserman (2003), *Multiple view geometry in computer vision*, Cambridge University Press, Cambridge, UK; New York.

Hill, D. F., and B. D. Younkin (2006), PIV measurements of flow in and around scour holes, *Exp Fluids*, *41*(2), 295-307.

Khosronejad, A., S. Kang, and F. Sotiropoulos (2012), Experimental and computational investigation of local scour around bridge piers, *Adv Water Resour*, *37*, 73-85.

Kothyari, U. C., W. H. Hager, and G. Oliveto (2007), Generalized Approach for Clear-Water Scour at Bridge Foundation Elements, *J Hydraul Eng* (New York, N.Y.), *133*(11), 1229-1240.

Legleiter, C. J., P. C. Kyriakidis, R. R. McDonald, and J. M. Nelson (2011), Effects of uncertain topographic input data on two-dimensional flow modeling in a gravel-bed river, *Water Resour Res*, *47*(3).

Lewis, J.P. (1995), Fast Normalized Cross-Correlation, Industrial Light & Magic, http://scribblethink.org/Work/nvisionInterface/nip.html#foot263.

Link, O., F. Pfleger, and U. Zanke (2008), Characteristics of developing scour-holes at a sand-embedded cylinder, *Int J Sediment Res*（国际泥沙研究：英文版）, *23*(3), 258-266.

Liu, C., and Y.-m. Shen (2008), Flow structure and sediment transport with impacts of aquatic vegetation, . *J Hydrodyn*. *Series B*, *20*(4), 461-468.

Lu, J.-Y., Z.-Z. Shi, J.-H. Hong, J.-J. Lee, and R. V. Raikar (2011), Temporal Variation of Scour Depth at Nonuniform Cylindrical Piers, *J Hydraul Eng* (New York, N.Y.), *137*(1), 45-56.

Melville, W. B., and Y. M. Chiew (1999), Time scale for local scour at bridge piers, *J Hydraul Eng* (New York, N.Y.), *125*(1), 59-65.

Mia, M. F., and H. Nago (2003), Design Method of Time-Dependent Local Scour at Circular Bridge Pier, *J Hydraul Eng* (New York, N.Y.), *129*(6), 420-427.

Oliveto, G., and W. H. Hager (2002), Temporal Evolution of Clear-Water Pier and Abutment Scour, *J Hydraul Eng* (New York, N.Y.), *128*(9), 811-820.

Ott, L., and M. Longnecker (2010), *An introduction to statistical methods and data analysis*, Brooks/Cole Cengage Learning, Australia; United States.

Pelletier, J. D. (2009), Controls on the height and spacing of eolian ripples and transverse dunes: A numerical modeling investigation, *Geomorphol* (Amsterdam, Netherlands), *105*(3-4), 322-333.

Remondino, F., and S. El-Hakim (2006), Image-based 3D modelling: A review, *Photogrammetr Rec*, *21*(115), 269-291.

Rodrigue-Gervais, K., P. M. Biron, and M. F. Lapointe (2011), Temporal Development of Scour Holes around Submerged Stream Deflectors, *J Hydraul Eng* (New York, N.Y.), *137*(7), 781-785.

Roulund, A., B. M. Sumer, J. Fredsoe, and J. Michelsen (2005), Numerical and experimental investigation of flow and scour around a circular pile, *J Fluid Mech*, *534*, 351-401.

Sambrook Smith, G. H., and A. P. Nicholas (2005), Effect on flow structure of sand deposition on a gravel bed: Results from a two-dimensional flume experiment, *Water Resour Res*, *41*(10).

Shakibaeinia, A., and Y.-C. Jin (2011), A mesh-free particle model for simulation of mobile-bed dam break, *Adv Water Resour*, *34*(6), 794-807.

Shapiro, L. G., and G. C. Stockman (2001), *Computer vision*, Prentice Hall, Upper Saddle River, NJ.

Umeda, S., T. Yamazaki and H. Ishida (2008), Time evolution of scour and deposition around a cylindrical pier in steady flow, paper presented at International Conference on Scour and Erosion. Tokyo, Japan, 140-146

Wu, W., F. D. Shields, S. J. Bennett, and S. S. Y. Wang (2005), A depth-averaged two-dimensional model for flow, sediment transport, and bed topography in curved channels with riparian vegetation, *Water Resour Res*, *41*(3).

Xia, J., B. Lin, R. A. Falconer, and G. Wang (2010), Modelling dam-break flows over mobile beds using a 2D coupled approach, *Adv Water Resour*, *33*(2), 171-183.

Yanmaz, A. M., and H. D. Altinbilek (1991), Study of Time-Dependent Local Scour around Bridge Piers, *J Hydraul Eng* (New York, N.Y.), *117*(10), 1247-1268.

Zech, Y., S. Soares-Frazao, B. Spinewine, and N. Le Grelle (2008), Dam-break induced sediment movement: Experimental approaches and numerical modelling, *J Hydraul Res*, *46*(2), 176-190.

Zeng, J., G. Constantinescu, K. Blanckaert, and L. Weber (2008), Flow and bathymetry in sharp open-channel bends: Experiments and predictions, *Water Resour Res*, *44*(9).

Zhang, H., H. Nakagawa, K. Kawaike, and Y. Baba (2009), Experiment and simulation of turbulent flow in local scour around a spur dyke, *Int J Sediment Res*（国际泥沙研究：英文版）, *24*(1), 33-45.

List of Figures

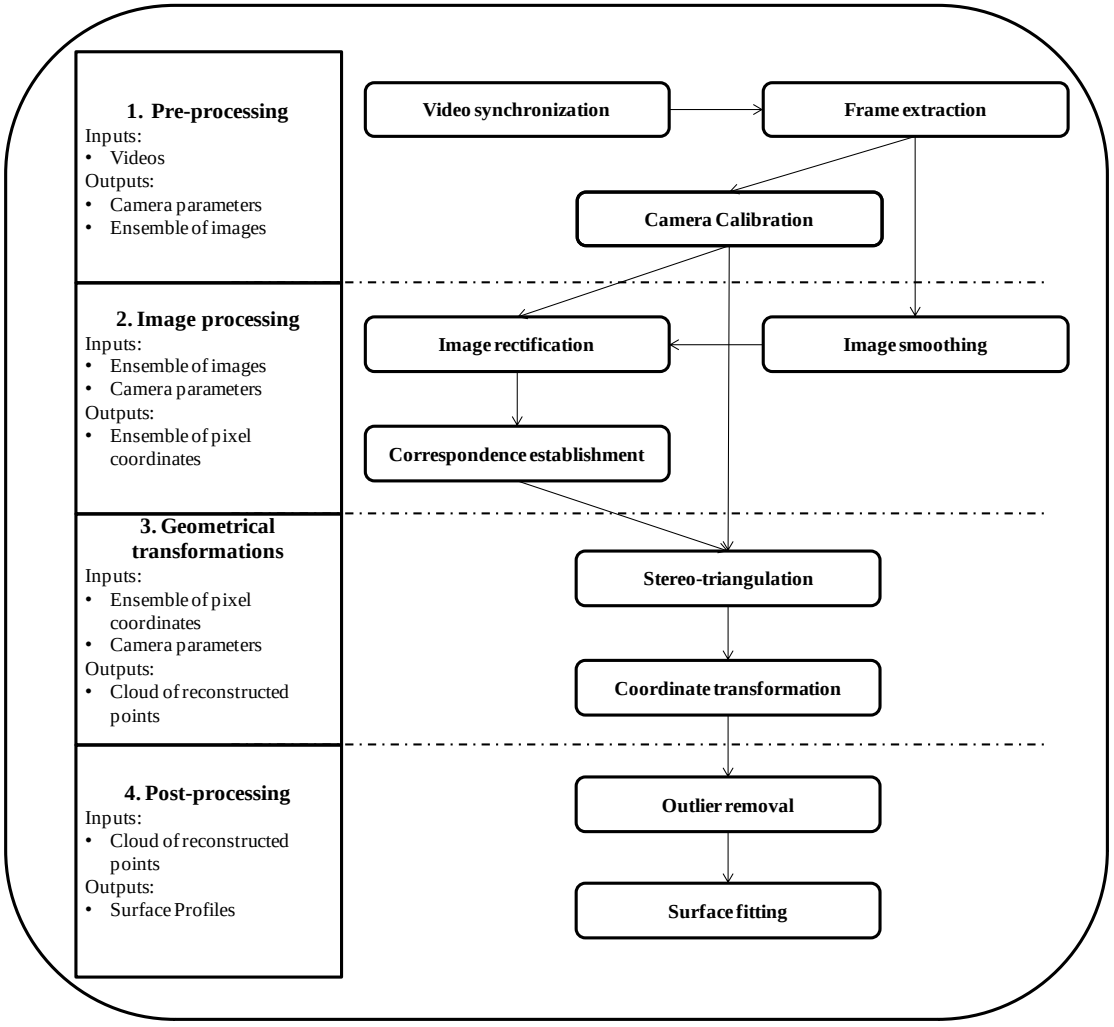

Fig. 1. Overview of the technique.

Fig. 2. View of the flume and the model pier.

Fig. 3. The cameras recording the scour hole, mounted on the side walls of the flume.

Flow direction is from left to right.

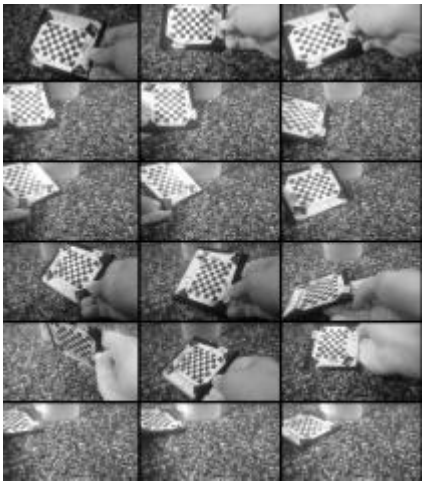

Fig. 4. Images of the calibration target obtained at different angles from the same camera.

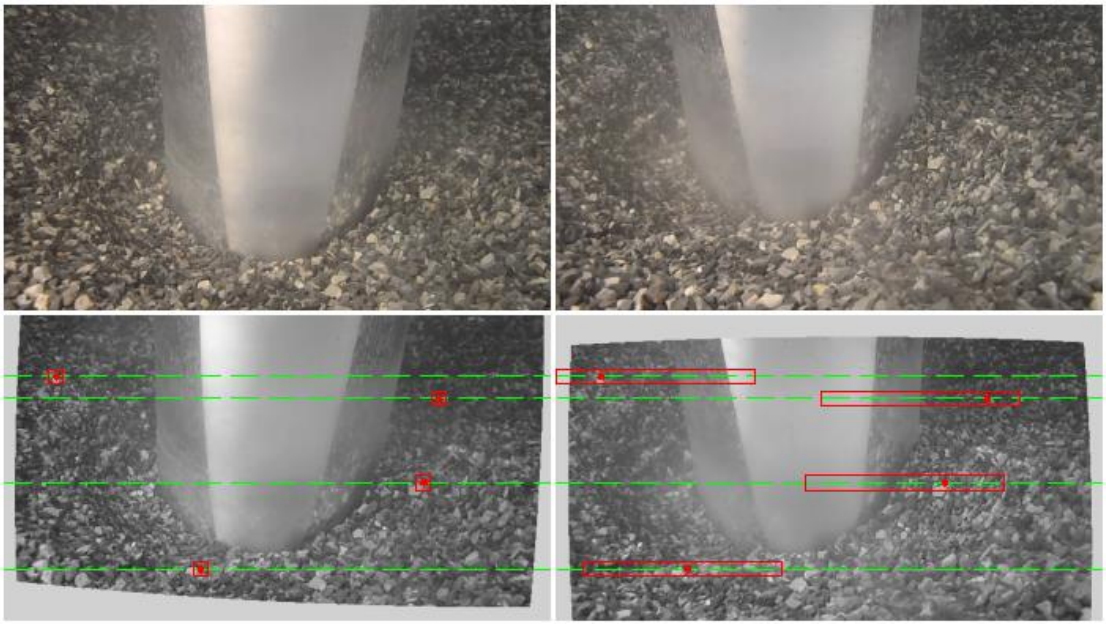

Fig. 5. a (top) A pair of raw coincident frames that were extracted from the videos. b (bottom) The same pair of frames after the smoothing and the rectification procedure. The dots represent a few selected correspondences between the two frames. The dotted lines demonstrate the effect of rectification. The squares of the left frame are the extracted templates that are cross-correlated with the rectangles of the right frame, which are the extracted windows, to find correspondences. Flow direction is from left to right.

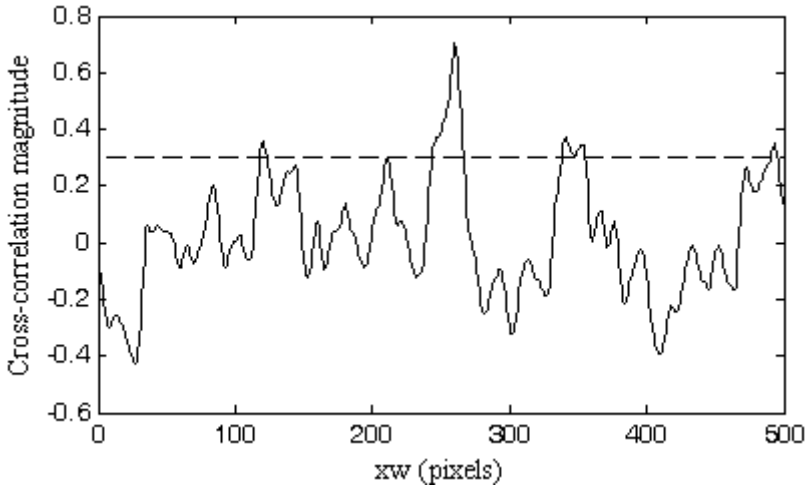

Fig. 6. The result of the normalized cross-correlation of the template that is located in the lower position of Fig. 5b, with the respective window. The dashed line represents the threshold value for the result of the normalized cross-correlation.

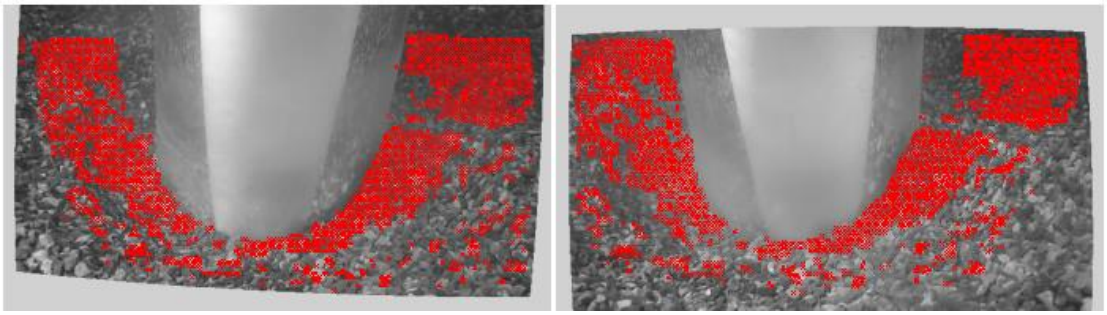

Fig. 7. The pixel location of all the correspondences that were identified between the two coincident frames at the second step of the analysis.

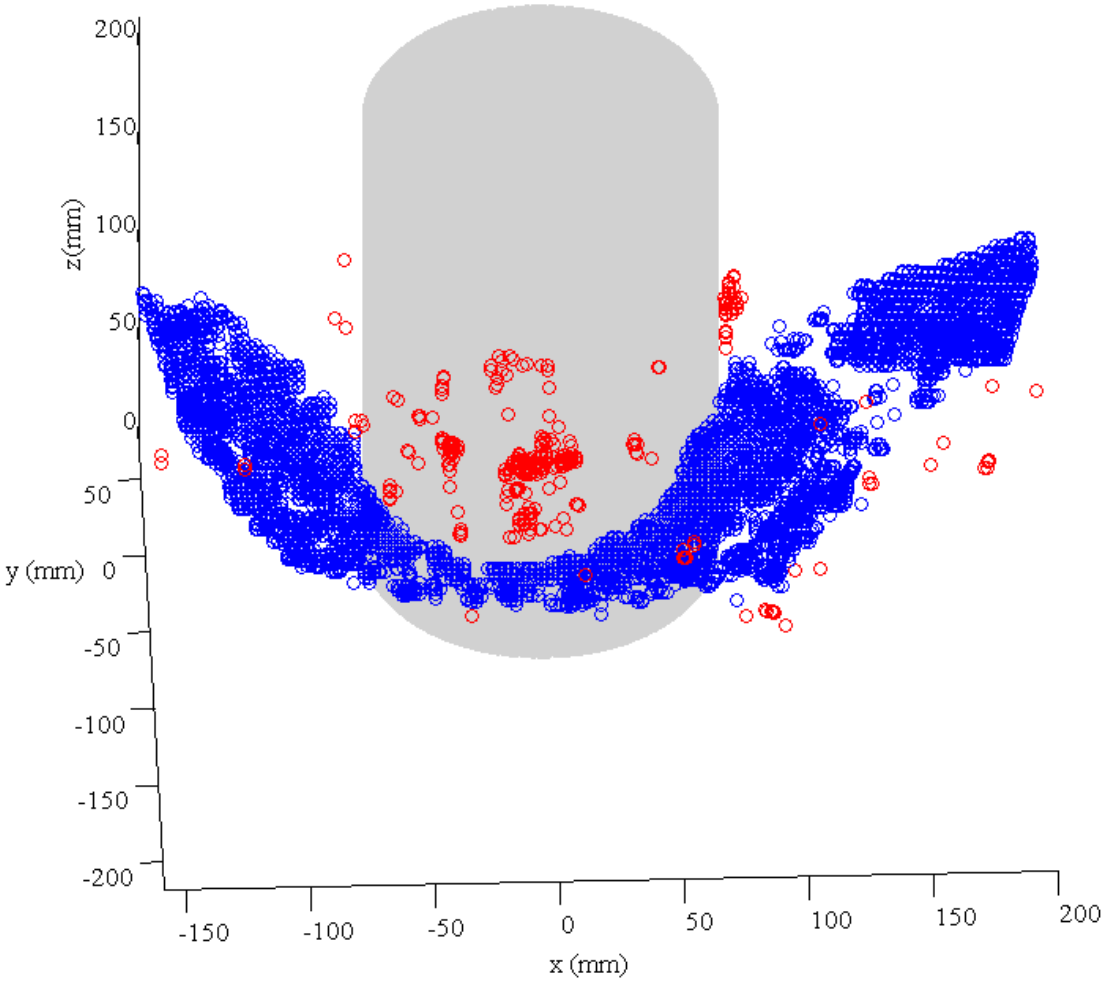

Fig. 8. The reconstruction of the correspondent points that were identified in Fig. 7. The red circles are the points that were marked as outliers in the 4 the stage of the analysis and the blue circles are the valid points.

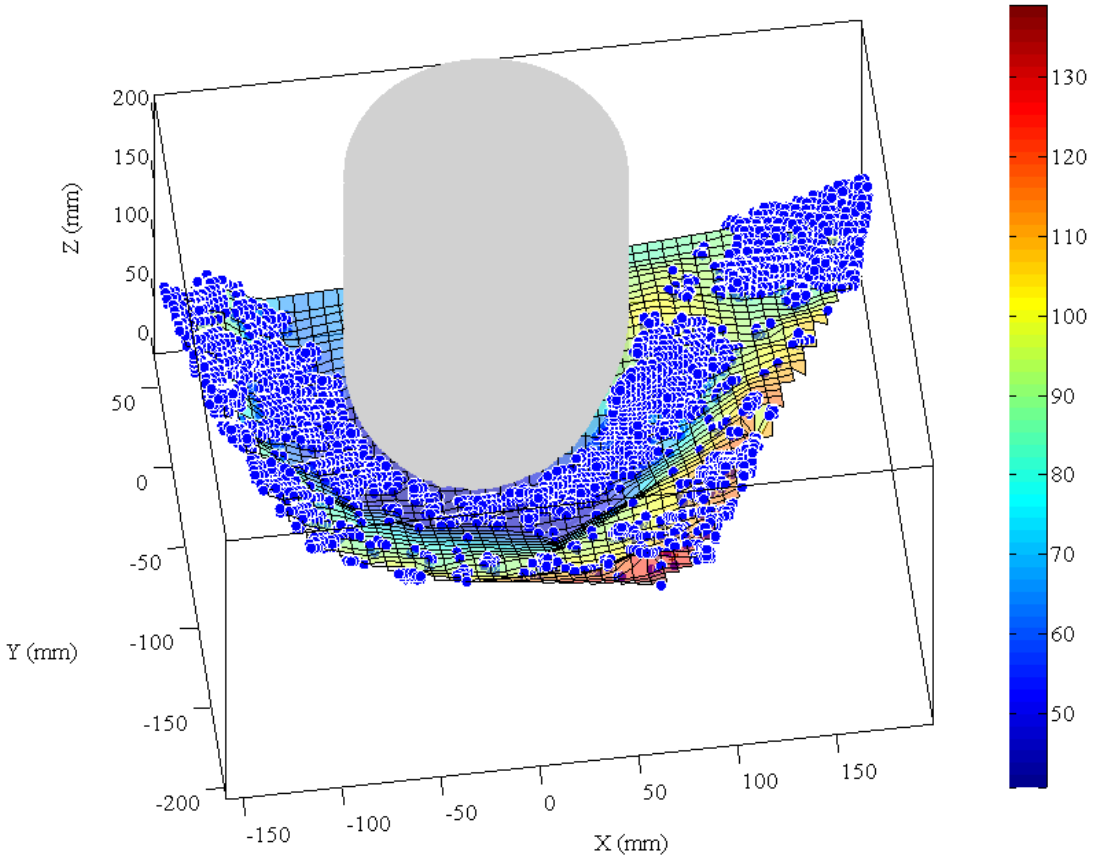

Fig. 9. The surface that was fitted to the valid reconstructed points (circles) through linear interpolation.

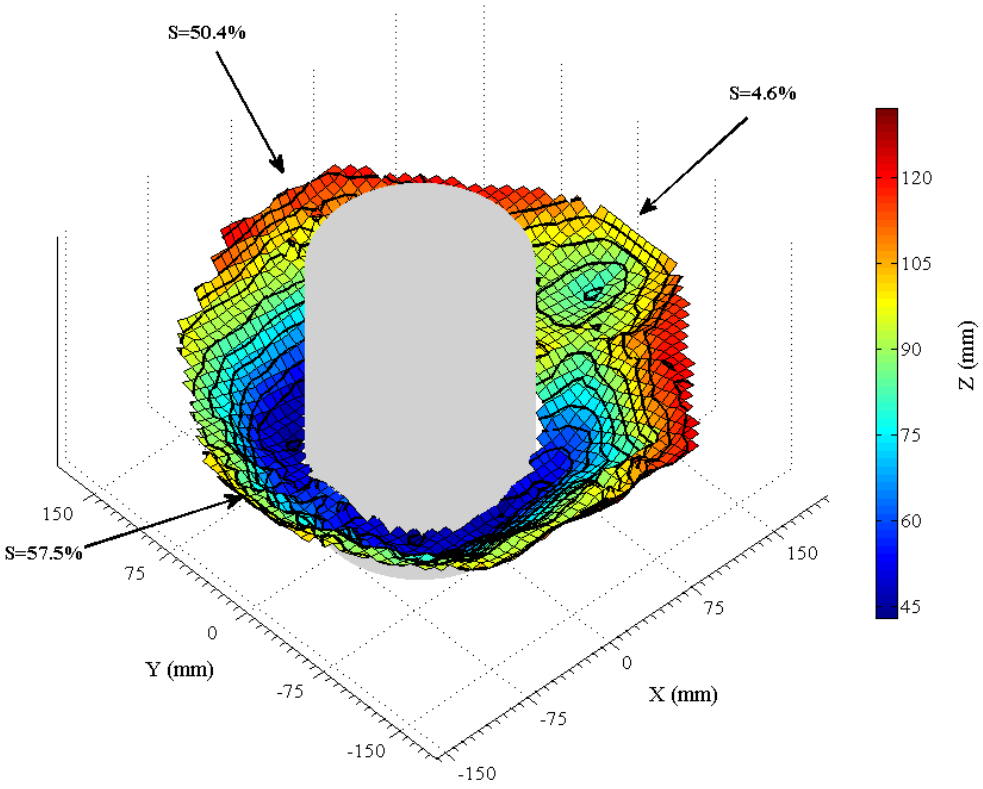

Fig. 10. The reconstructed topography of the bed 120 minutes after the initiation of scour. Flow direction is along the x axis. The average slopes of the upstream, side and downstream part of the scour hole are highlighted.

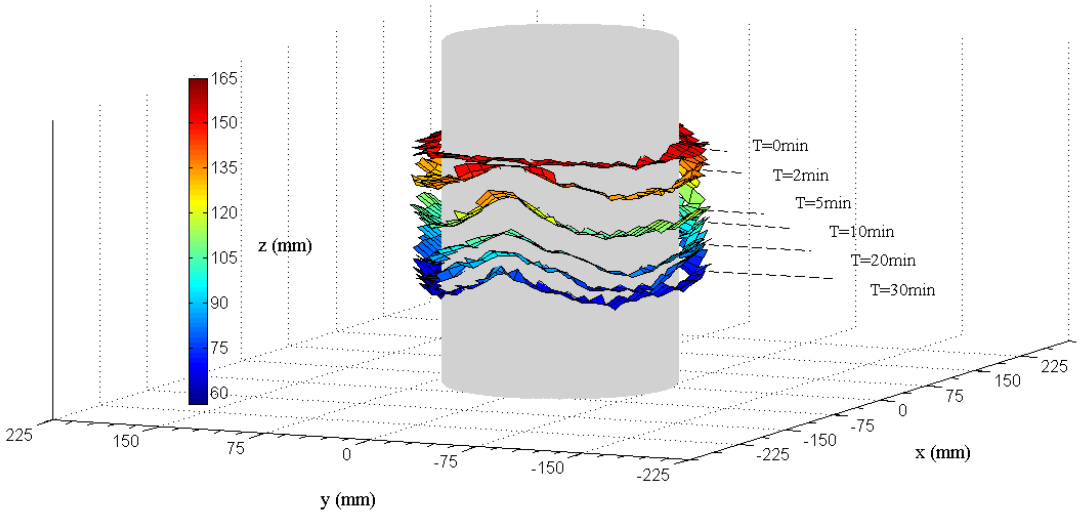

Fig. 11. The profile of the scour hole around the perimeter of the pier at 6 different instants. The maximum radial distance of the reconstructed profiles from the surface of the pier is 0.15D. Flow direction is along the x axis.

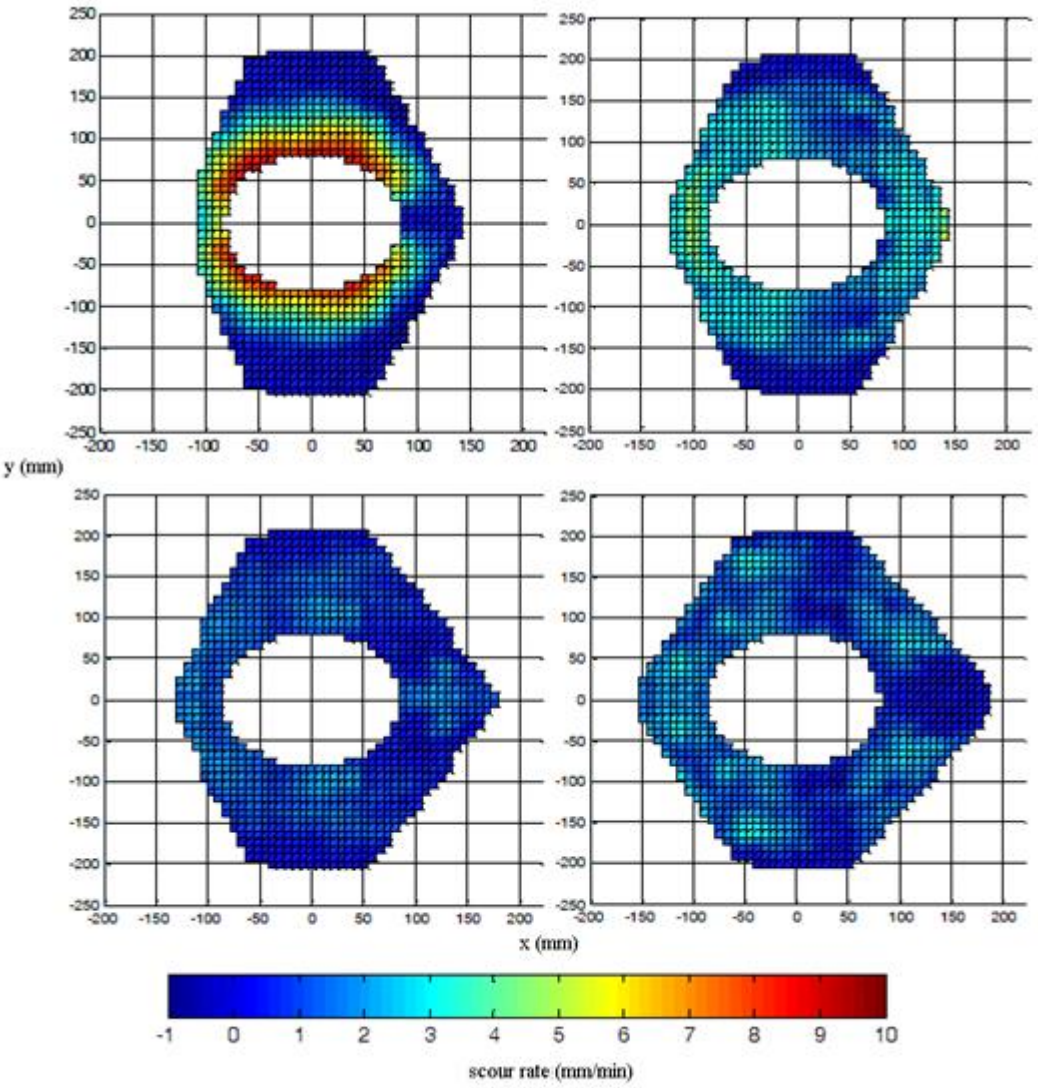

Fig. 12. The scour rates of the scour hole at 5 (upper left), 10(upper right), 20 (lower left) and 30 (lower right) minutes from the initiation of scour. Flow direction is along the x axis.

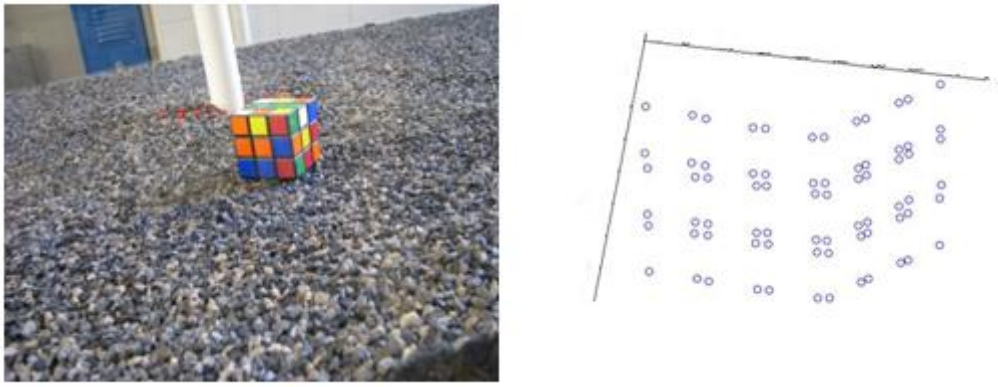

Fig. 13 a (left). The object that was used for the investigation of the calibration error. b (right). The corners of the object that were reconstructed with the current technique.

Chapter 3. Quantitative characterization of scour at the base of a cylinder

Abstract The measurement of the morphologic characteristics of evolving sediment beds around hydraulic structures is crucial for the understanding of the physical processes that drive scour. Although there is significant progress towards the experimental characterization of the flow field in setups with complex geometries, little have been done towards the quantitative investigation of dynamic sediment beds, mainly due to the limiting capabilities of conventional instrumentation. However, it is now commonly accepted that the key to the development of successful engineering tools for the prediction and mitigation of scour is the understanding of the complex interaction between the flow and the eroding bed. Here, a recently developed computer vision technique is applied to obtain high resolution topographic measurements of the bed at the base of a cylinder, during clear water scour. The morphologic characteristics of the bed such as the excavated volume, the slopes of the bed, the rates of scour and the bathymetry at multiple locations are statistically investigated. Through this investigation and the discussion of existing flow measurements from previous studies, the physical processes that take place inside a developing scour hole are thoroughly described. Also, expressions for the statistical modelling of the bed features are derived.

3.1 Introduction

The interaction among hydraulic structures, water flows and sediment beds is one of the most complicated phenomena in hydraulic engineering. The prediction of changes in the bed's topography due to scour is fundamental for the safe and cost-effective design of hydraulic structures. This problem has been extensively investigated over the last decades through numerous laboratory tests, field observations, and derivation of empirical relationships. The main focus of the majority of these studies has been on the prediction of the maximum scour depth after several hours or even days of testing, when equilibrium conditions have been reached. Fewer studies have focused on the temporal evolution of the instantaneous maximum scour depth. Many of the derived empirical or semi-empirical relationships were recently summarized and evaluated by *Sheppard et al.*, [2011]. Although these efforts have provided us with important insights on the effects of various parameters on the scour depth in laboratory simulations, the physical understanding of the phenomenon is incomplete. Consequently, our confidence in the reliability of our engineering tools for the design and protection of hydraulic structures is limited.

In an effort to better understand the physics behind scour, fluid flows around wall mounted obstacles, such as cylinders or wings, have been described from experimental observations [*Baker*, 1979; *Dargahi*, 1989; *Devenport and Simpson*, 1990] or numerical simulations [*Paik et al.*, 2010; *Escauriaza and Sotiropoulos*, 2011; *Koken and Constantinescu*, 2009]. These studies examined the time-averaged and time-resolved characteristics of flows around the obstacles. Coherent vortices forming at the face of the obstacles and

periodically shedding vortices at the wake of these obstacles were identified as the main agents that drive scour.

In order to examine directly the interaction among the flow, the structure and the channel bed, studies of flows over erodible boundaries have been carried out by several researchers. However, the laboratory investigation of these cases presents important challenges that usually compromise the resolution and reliability of the measurements. Consequently, many of these studies focus on the description of the flow over static beds that have either been artificially stabilized, or have reached equilibrium condition [*Istiarto and Graf*, 2001; *Dey et al.*, 2007; *Kumar et al.*, 2012]. However, artificially stabilized beds provide a nearly static representation of the actual dynamic phenomenon and therefore do not allow for the study of the evolving scour hole due to the interaction among the flow, the structure and the channel bed. Also, many researchers agree that the equilibrium is not representative of the conditions in the field, due to the very long duration of floods that are required to approach it [*Melville and Chiew*, 1999; *Kothyari et al.*, 2007; *Simarro et al.*, 2009].

In many other cases, time-resolved measurements of the bed have been carried out by measuring the bathymetry of the bed at one or a few locations within the scour hole [*Olivetto and Hager*, 2002; *Melville and Chiew*, 1999; *Lu et al.*, 2011]. This is usually accomplished with acoustic or laser range finders, or simpler methods such as the recording of measuring scales attached to the model structure. When these measurements are accurate, the results are useful for the derivation of relationships between time and scour depth; yet, the morphological characteristics of the bed are unknown and no significant insight is gained regarding the physics of the phenomenon.

In very few cases the evolving topography of the scour hole has been experimentally investigated. For example, *Radice et al*. [2009 and 2012] employed an image-processing technique to study the kinematics of the mobile sediments within a scour hole around an abutment. They recorded the sediment bed through a transparent window that was covering the surface of the flow to observe how the patterns of sediment transport vary as scour grows. Also, *Link et al.* [2008] used a laser range finder mounted on a motorized carriage inside a transparent cylinder and obtained multiple bathymetric measurements within an evolving scour hole. In their study, complete topographies were measured in an asynchronous manner in 30-180 seconds per topography scan and a few of them were presented to discuss some morphological characteristics of the bed, such as volumes and slopes around the scour hole. Additionally, *Dargahi* [1990] presented the evolving centerline profile upstream and downstream a cylinder, at the first instants of scour and included an extensive discussion about the characteristics of the flow and corresponding bathymetric profiles. He did not provide, however, any information about the accuracy of his measurements and his discussion about various bed features was mainly qualitative in nature.

Perhaps the most thorough descriptions of the evolving morphological characteristics of the bed and correlations with the flow are provided in recent numerical simulations by *Kirkil and Constantinescu* [2007] and *Escauriaza and Sotiropoulos* [2011b]. Both groups carried out coupled modelling of the flow and the bed in an effort to identify the cause and effect relationships that drive scour. Their models were validated with the findings of *Dargahi* [1990], or with very basic laboratory measurements that they carried out themselves.

Based on the measurements, simulations, and visual observations available in existing studies, several descriptions have been provided about the phenomena that take place inside developing scour holes and empirical descriptions of this complicated phenomenon have been proposed. Although reasonable, many of these descriptions are not supported by experimental data and they are rather qualitative.

Here we describe the morphological characteristics of an evolving gravel bed, around a circular cylinder, under clear-water scour conditions. We have employed a recently developed computer vision technique [*Bouratsis et al.*, 2013] to overcome the limitations of existing instrumentation and measure accurately, continuously and nonintrusively the development of the scour hole topography at very high spatial and temporal resolution. Such measurements avoid the perturbations introduced by stopping and restarting the experiment and the impact of intrusive measuring technologies, both of which can alter the outcome of the experiment. The most important characteristics of the evolving bed are described quantitatively for a simple experimental case. The results are physically interpreted and compared with descriptions of the flow and bed characteristics that have been presented in previous studies, to investigate the main mechanisms of scour.

The experimental parameters and the measuring technique are described in the next section. Following, the evolving topographies, scour rates, slopes and volume of the scour hole are elaborated in Section 3. In Section 4, the overall results are considered in an effort to associate the findings with expected flow characteristics and describe physically the phenomenon. Finally, the main conclusions are summarized in Section 5.

3.2 Experimental Set up

The purpose of this work was to study a single experiment to the highest detail and measure processes that were not investigated in previous studies. Also, it was imperative that the results from this experiment could be compared with flow measurements from previous studies. For this reason a simple and commonly observed experimental setup was adopted. The experiment was carried out in a flume 16.2m long and 1.2m wide, with slope (S) equal to 0.0005 (Fig. 1a). The bed material was uniform gravel with median diameter, d_{50} =3.55, geometric standard deviation, σ =1.35, and angle of repose, φ =35^o. The approach flow depth, H, was 0.205m and the approach flow velocity (V) was 0.620m/s. The model pier was a circular cylinder with diameter, D, equal to 0.152m. The cylinder was mounted on the center of the flume approximately 50 flow depths downstream the entrance of the flume, to ensure that the flow was fully developed (Sabersky et al., 1999). The experiment lasted for 250 minutes and the temperature (T) was 25^{o}C. The most relevant dimensionless parameters of the experiment are: τ/τ_c=0.95, H/D=1.35, D/d_{50}=43, Re_D=81,000, Re_H=109,000, Fr=0.44; where τ: bed shear stress; τ_C: critical shear stress for sediment entrainment, Re_D: pier diameter based Reynolds number (Re_D=VD/ν, ν: kinematic viscosity), Re_H: approach depth based Reynolds number (Re_H=VH/ν), and Fr: Froude number ($Fr=V/(gH)^{0.5}$, g: gravitational acceleration).

For the monitoring of the channel bed evolution in the vicinity of the pier, two waterproof cameras (Olympus Stylus Tough - 6020) were used. The cameras were mounted firmly on the sidewalls of the flume close to the test section, as shown in Fig. 1b, and were recording videos at 30 frames per second, with resolution equal to 720x1280 pixels, while being

partially submerged (approximate submerged length 50 mm). The purpose was to record half of the scour hole, and subsequently assume symmetry. The distance of the cameras from the bed and the cylinder were approximately 180mm and 400mm, respectively. Before the beginning of the experiment, water was introduced gradually, while an adjustable tailgate at the downstream end of the flume was raised. As soon as the flow depth reached the desired elevation, the cameras were synchronized using a stroboscopic light, and started recording videos. Then the target velocity was reached by adjusting the flow discharge and the tailgate. At the completion of the experiment, which lasted for 250 minutes, the flow discharge was reduced and the tailgate was raised. Before draining the flume, the bed bathymetry was measured with a point gauge mounted on the rails located on the top of the flume sidewalls.

The recorded videos were processed in Matlab by applying a computer-vision based technique that was recently developed by *Bouratsis et al*. [2013] (Chapter 2). The inputs for this technique are the two synchronized videos of the evolving bed and the final outputs are the 3D representations of the bed topography at multiple instants. This is achieved by the implementation of a series of algorithms that perform calibration of the cameras, establishment of stereo-correspondences between coincident frames, stereo-triangulation of 3D point-clouds, outlier removal from the point clouds and surface fitting. The maximum temporal resolution of the technique, as applied here, was 30 reconstructed surfaces per second. An area of approximately 140 cm^2 of the bed was represented by more than 6000 points at every instant. The accuracy of the measurements was 0.86 mm and the precision was 2.31 mm. The detailed description of the technique along with investigations of its accuracy and reliability are presented by *Bouratsis et al.* [2013]. Overall, this

methodology allows for the continuous collection of very high temporal and spatial resolution measurements of the bed topography, while being minimally intrusive. Though numerous experiments using this rather straightforward set up have been carried out in the past, this is the first time that such high quality quantitative observations of the scour around a pier problem have been possible.

3.3 Results

3.3.1 Overview of the scour hole evolution

In this section, series of scour depth and scour-rate maps are presented, to provide an overview of the evolution of scour. The included series of contour maps provide a useful overview of the spatial and temporal characteristics of scour. Although, these maps are very accurate, they can better convey qualitative, rather than quantitative features of the phenomenon. A more targeted investigation of the statistical properties of the scour evolution will be included in Section 3.2. All results are presented in terms of dimensional parameters in an effort to render the trends in a way that is easier to follow. Furthermore, since a single experiment is described here, a dimensionless approach would not generalize the results in a meaningful way. For most of the description of the results a cylindrical coordinate system is used with coordinates (r, θ, s); where r is the distance from the center of the pier; θ is the angle of the plane around the cylinder, measured from the direction of the flow; and s is the scour depth measured from the original unscoured bed elevation.

Figure 2 includes representations of the scour depth maps during the first 8 minutes of the experiment. It is shown that scour starts at planes 45^o-110^o from the axis of symmetry. Some small erosion is also observed at a radial distance r = 90 mm from the surface of the

cylinder, at planes 60^o-100^o; but the maximum scour is adjacent to the cylinder surface. From the sequence of the contour maps shown in Fig. 2, it is evident that the maximum depth during the first 8 minutes is constantly located at the 60^o plane. The scour hole expands around the perimeter of the cylinder and reaches the axis of symmetry, after approximately 3 minutes. Scour depth along the axis of symmetry remains significantly smaller compared to that at the sides for the duration of the experiment. Overall, the radial span of the scour hole increases continuously during the first 8 minutes, reaching a maximum value of 107 mm at the 20^o plane.

The sediments that were excavated during the first 4 minutes are deposited in the area confined between planes 150^o-180^o. The height and span of the initially formed deposition area remain essentially constant during the first 4 minutes. Then, this small deposition of sediments is removed and scour at the wake begins at t=6 min. The rate of scour at the wake region during the period of 6 – 8 min is higher compared to that observed in any other areas within the scour hole.

At t=8 min, a horseshoe-shaped scour hole has already been developed around the cylinder. The slopes of the hole are steep (up to 39^o) on the sides of the cylinder and very mild (less than 15^o) at the wake of the cylinder. It is noted that the maximum scour depth at t=8min is 63% of the maximum scour depth at t=240min.

Additional scour depth profiles are included in Fig. 3. The time interval between these snapshots is longer than in Fig. 4, because the rate of scour is more moderate and milder differences are observed. From t=8min to t=30min, the most important bathymetric differences have taken place at the front (0^o-20^o) and the wake (155^o-180^o) of the cylinder.

During this time interval, the maximum scour depth, which is always observed at 60^o, is marginally increased (from 71.5 mm to 92.9 mm). Similarly, the contour maps at t=50min, 120min and 180min, show that changes in local bathymetry are more pronounced at the sectors 0^o-20^o and 155^o-180^o. Over the same period, the scour depth at the front of the cylinder is increasing faster (from 78.8mm to 101.5mm), compared to the side (from 96.9mm to 111.2mm). Also, during this period, the horizontal span of the scour hole is increasing uniformly around the cylinder, except for the wake region. The width of the wake region is decreasing, as a deep groove that has formed adjacent to the cylinder is expanding towards the downstream direction. From t=180min to t=250min, the bathymetric changes are very small and are characterized by the increased scour depth at the front of the cylinder and increased width of the groove adjacent to the cylinder. At t=250min, the maximum scour depth is marginally higher at the upstream axis of symmetry, compared to the sides of the cylinder, for the first time since the beginning of the experiment.

In an effort to identify the change in the rate of scour activity with location, corresponding maps were developed (Fig.4). The rates were estimated as follows: 1) A dense (50x50) grid that covers the area of the reconstructed topographies was defined at every instant; 2) The scour evolution at every point of the grid was found; 3) The gradient of every point-wise scour evolution curve was estimated and values of rates were assigned to all the grid points, at every instant; 4) New contour maps were reconstructed from the grid with the rate values.

In Fig. 4, at t=1min and t=3min, it is shown clearly that scour starts at the side of the cylinder and it is initially progressing at higher rates there. At the same instants, it is shown that scour rates at the 0^o plane are almost zero and that sediments are deposited downstream

of the cylinder immediately after the initiation of scour. At t = 6 min, the scour rates have been reduced and the maximum values are observed in patches that are not located directly adjacent to the cylinder, but coincide approximately with the location of the maximum scour depth as shown in Fig. 2. Also, at this instant, scouring has already begun at the wake of the cylinder.

At the contour maps after t = 8 min, it is observed that scour rates have been further decreased and their distribution does not follow any particular pattern. As an example of this random distribution, the scour rate maps at t = 17 min, 34 min and 51 min are included in Fig. 4. It is shown that the maximum rates form smaller patches whose location varies in time. At some instants the scouring activity is very low at all locations (e.g. t = 17 min), and at some other instants most of the high-rate patches are accumulated at the front of the cylinder (e.g. t=34min), or at the side of the cylinder (e.g. t=51min). Overall, the most notable feature of the sequence of the scour rates is that after t=8min, the location, distribution and magnitude of the instantaneous rates vary significantly with time. Consequently, the distributions of scour rates averaged over longer periods (not shown here) are very low and uniform. The contrast in the evolution of the scour hole before and after t=9min suggests initially the presence of an organized structure which subsequently disappears and the phenomenon becomes more random.

The examination of all the series of scour rates shows that during t=0-9min the maximum scour rates coincide with the location of maximum scour depth. On the contrary, after t=9min, instantaneous peaks of high scour rates appear at random locations. These values when averaged over 20min or more a nearly zero-evolution pattern is observed.

To provide a more complete overview of the temporal evolution of scour, the volume of the excavated material of the reconstructed scour holes as a function of time is plotted in Fig. 5. The temporal evolution of the volume can be accurately described by two power curves. The breakpoint between the two curves is observed at about t=9min. As it was discussed earlier, this instant also marks the difference in the spatial distribution of the scour rates. Another important comparison between the temporal evolution of the rates and the volume is that despite the random distribution of the instantaneous maximum scour rate locations, the overall excavated volume, after t=9min, is very well described by a single power curve.

Based on results that have been discussed so far the scour evolution could be divided in two phases, namely before t=9min and after t=9min. Also, there can be made a crude categorization of different areas around the cylinder. The initial and development phases and the front, side and wake regions will be prematurely defined here to assist the presentation of the results and their discussion in the following sections. Table 1 includes the limits of the phases and the regions and some of their characteristics that will be discussed next.

3.3.2 Dependence of scour depth on location and time

Functional relationships were sought to express the scour depth at any location and instant as a function of time (t), distance from the surface of the cylinder (r), and angle relative to the flow direction (θ). The purpose of this investigation was to examine the temporal and spatial evolution of the scour hole and to validate the existence of separate phases of the phenomenon in time and areas within the scour hole with different erosional characteristics.

A dense (50x50 nodes) cylindrical grid was defined on the reconstructed topographies. For every point of the grid, the cylindrical coordinates, the time and the scour depth were defined (r, θ, t, s). Then, regression analysis was carried out to express scour depths as function of time. To do that a Matlab code was developed to fit logarithmic, power and polynomial functions to describe the temporal evolution of scour at all locations and evaluate the statistical justification of these functions based on the coefficient of determination (R^2) and the sum of squared errors (SSE). It was found that the temporal evolution of the scour depth at every location with $\theta < 130^o$ could be optimally ($R^2 > 0.95$) described by a piecewise power function, with one breakpoint. The area of the scour hole with $\theta > 120^o$ was described less successfully ($R^2 \sim 0.7$) by power functions. Table 1 shows the general form of the equations that describe scour as a function of time and Fig. 6 illustrates some examples of the curve fitting results. The breakpoint was placed successfully at t=9min for the locations where scour started during the first 3 minutes of the experiment (see Fig. 2). At the locations where scour started later, the breakpoint was placed at succeeding instants.

An additional distinction could be made for the area with $\theta < 0^o < 20^o$ where the slopes of the curves after the breakpoint were consistently higher compared to the slopes of the curves at $20^o < \theta < 130^o$. This is illustrated in Fig. 7, where pointwise scour is plotted against time for locations with r = 10 mm and θ varying from 0^o to 180^o. It is shown that after the initial phase (t>9min) the scour rate at $0^o < \theta < 20^o$ is greater compared to the other planes. As a result, at t = 250 min the scour depth is higher at the face of the cylinder. Also, in Fig. 7, it can be observed that the shapes of the scour depth evolution curves at $\theta > 130^o$ are significantly different compared to the other planes.

The second part of the morphological investigation was the regression analysis between the instantaneous scour depth and the radial distance from the cylinder (Fig. 8). The most important observation in Fig. 8, is that the slopes of all radial profiles within the scour hole remain relatively constant after t = 9 min. Also, the plots at planes 0^o to 90^o show more clearly the existence of the deeper groove that is located immediately adjacent to the cylinder and it was also observed in Fig. 2 and 3. The width of the groove is decreased towards the downstream direction. Despite the deepening effect of the groove, the regression analysis for the angular planes at the front and the sides of the cylinder ($0^o < \theta < 135^o$), can be well approximated ($R^2 > 0.9$) with linear curves whose slopes remain constant in time but vary with θ. On the other hand, the radial profiles at $\theta > 130^o$ cannot be represented with linear functions of r as effectively. Instead second or third degree polynomials should be used to approximate the local bed topography along angular planes at the wake (Table 1).

The time-averaged slope of every radial profile, after t=9min was found from the instantaneous linear fits of the radial profiles (as shown in Fig.8). The results are plotted in Fig. 9. It is shown that the average slopes at different angular planes vary significantly. They are increasing from $\theta = 0^o - 40^o$ and then they are decreasing from $\theta = 40^o - 110^o$. Also, the time-averaged slopes at $\theta = 50^o - 70^o$ are higher than the estimated angle of repose (35^o).

The final part of the morphological analysis included the investigation of functional relationships between s and θ (Fig. 10). It is shown that after t=9min, at r=5mm, s can be expressed as a sinusoidal function of θ (Table 1). Notably, the period of the sinusoidal equation that is defined in Fig. 10, is similar to the period of the sinusoidal function that

could be used to represent the average slope of the radial profiles in Fig. 9. As a result, a sinusoidal equation between s and θ could be applied at any r. The only area that does not follow this trend is at the front face of the cylinder ($\theta < 20^o$). At the latter location, scour depth increases at higher rates, discussed above.

3.4 Discussion

Summarizing the presented results (Table 1) we can define two phases of scour and divide the scour hole into three regions. Specifically, the initial phase lasts until t=9min and is followed by the scour development phase that lasts until the end of the experiment (t=250min). Regarding the spatial discretization of the scour hole, the angular limits of each region relative to the flow direction, are: $\theta<25^o$ for the front region, $25^o<\theta<135^o$ for the side region and $135^o<\theta<180^o$ for the wake region.

3.4.1 **Interpretation of the results**

During the initial phase, scour starts and evolves at very high rates at the side region (Fig. 2, Fig. 4). This is attributed to the higher bed stresses that are caused by the contraction of the streamlines as flow moves around the cylinder [*Dargahi*, 1990; *Istiarto and Graf*, 2001]. In general, the distribution of the scour rates, that remains relatively constant during the initial phase, provides a good representation of the distribution of the shear stresses that are higher than the critical stress for particle entrainment. Specifically, the sinusoidal distribution of the scour depth around the cylinder (Fig.6) is consistent with the results of flow measurements in previous studies. The velocity measurements of *Dey and Raikar* [2007], over a developing scour hole, showed that the bed shear is increasing from the 0^o-plane to the 45^o plane and then it keeps decreasing continuously at the 90^o, 135^o and 180^o

planes. Our results, show a similar trend with the maximum scour depth being at the 65^{o}-plane. Further, it is noteworthy that the slope of the scour hole in the radial direction, around the cylinder follows a similar distribution with the shear stress and the scour depth. Consequently, these experimental results do not support the common assumption that the slopes of the scour hole at every angular plane, except for the wake region, are equal to the angle of repose [*Mia and Nago,* 2003; *Yanmaz,* 2011, *Guo,* 2014], as shown in Fig.9. Also, the slopes at the angles 40^{o}-60^{o} are higher than the angle of repose and this can be attributed to the hydrodynamic forces that counteract with gravity.

Overall, the fact that the location of maximum shear stresses coincides with the maximum scour depth suggests that scour during the initial phase is driven by the high stresses whose distribution in space remains constant. As a matter of fact, measurements by *Devenport and Simpson,* [1990] and *Roulund and Sumer,* [2005] have shown that the average shear stresses at the sides of cylinders on flat beds are up to 10 times as high as those measured in the approach flow upstream of the junction.

Another feature of the scour hole that was observed in both the bed topographies (Fig. 2 and Fig. 3) and the angular planes (Fig. 8), is the existence of the deeper groove around the cylinder that is expanding with time. The groove has also been observed by *Breusers and Raudkivi,* [1991] and *Kirkil and Constantinescu,* [2007] and it has been attributed to the existence of a corner vortex that is located at the intersection of the bed with the cylinder and rotates in the opposite (counterclockwise) direction compared to the primary horseshoe vortex [*Kumar et al.,* 2012; *Kirkil and Constantinescu,* 2007].

At the beginning of the development phase, two important differences are observed compared to the initial phase: i) the rate of scour at the front region is higher compared to the sides and the wake (Fig. 7); and ii) the rate of scour evolution at any location within the scour hole is reduced (Fig. 6 and Fig. 7). The former could be attributed to the stabilization of the core of the horseshoe vortex upstream of the cylinder, as it has also been suggested by *Istiarto and Graf,* [2001]; *Kirkil and Constantinescu*, [2007]; *Dey and Kumar*, [2007]. This is further supported by the fact that the slopes of the radial profiles remain relatively constant in time (Fig. 8).

The reduced scour rates, at the front and side regions, are commonly explained by the increase in the size of the horseshoe vortex that scales with the span of the scour hole [*Escauriaza and Sotiropoulos*, 2011; *Kumar et al.*, 2012]. As the size of the horseshoe vortex increases, its strength is decreasing and exerts lower shear stresses on the bed. Overall, it can be concluded that the stabilization of the horseshoe vortex is manifested by the breakpoint in the power plots of scour depth and volume (Fig. 5, Fig.6, Fig.7). Also, it is remarkable that the reduction of the strength of the horseshoe vortex that leads to the decreased average shear stresses is occurring only 9 minutes after the beginning of the experiment.

During the development phase, the distribution of the scour rates (Fig.4) implies that scour is driven by peaks of high bed stresses, randomly distributed in space, and that there no time-average indication of stresses that act continuously on the same location. In fact, there is no indication of a horseshoe vortex at the present scour rate maps, rather just instantaneous peaks of high rates that might be attributed to the horseshoe vortex. This observation resembles the findings of the numerical simulations by *Escauriaza and*

Sotiropoulos [2011] in scour holes that were close to equilibrium. However, in the presented experiment this observation is valid a few minutes after the beginning of scour. This may suggest that a quasi-equilibrium state has been reached during which the time scale associated with turbulent fluctuations is much higher and the behavior is similar to what is encountered when the scour hole has reached the equilibrium stage. This probably means that it would not be meaningful to define additional temporal phases, even if the experiment was further continued.

Overall, despite the seemingly random distribution of the maximum scour rates, the point-wise temporal evolution of the scour depth (at the front and the sides), (Fig.6 and Fig. 7), and the volume of the excavated material (Fig. 5) are well described by a power function. Also, because the slopes are constant during the development phase, it can be concluded that the horizontal span of the scour hole at every plane is proportional to the scour depth at every plane, therefore it evolves following a power function, as well.

Regarding the wake region, it is shown in Fig. 7 that the scour evolution varies significantly depending on the exact location. Also, the slopes of the radial profiles (Fig. 8) within the wake region are decreasing as the angle of the corresponding planes increases. According to the literature, the flow components that drive the temporal evolution and the shape of the wake region are the vortices that are shed periodically downstream of the pier [*Dargahi*, 1989, *Kirkil et al.*, 2011] and the oscillating legs of the horseshoe vortex [*Kirkil and Constantinescu,* 2007; *Escauriaza and Sotiropoulos*, 2011]. Similar to the observations at the front and the side regions, there is not an evident imprint of the aforementioned flow components in the scour rate maps. The erosional pattern in the wake region detected

through the image analysis supports the notion of a scour hole driven by instantaneous peaks of shear stresses.

Further, in Fig.3 it is observed that the angular span of the wake region is reduced in time, as the deep groove is expanding around the cylinder. This trend was also observed in the vorticity contour maps of *Escauriaza and Sotiropoulos*, [2011].

Overall, it is concluded that the initial phase, despite its short duration, is critical for modelling purposes because 63% of the 5-hour scour depth is developed then and because after this phase the shape of the scour hole does not undergo significant changes.

3.4.2 Limitations/Evaluation of the measurements

One of the limitations of the current results, is that some areas of the scour hole were not measured, because they were not located within the common field of view of the cameras. These areas include: i) the largest part of the scour hole at the opposite side of the plane of symmetry; ii) small areas close to the outer edge of the scour hole, at the side region, after t=60min; and iii) the entire deposition area downstream of the wake region. Regarding the area across the plane of symmetry, it is common practice to assume symmetry in bridge scour experiments given the symmetric nature of the flow. Next, the occluded areas near the edge of the scour hole were reconstructed through extrapolation to better visualize the results. Due to the location (relatively far from the cylinder) and size of these areas (always less than 4 cm^2) it is expected that the results and discussion presented here cannot be significantly affected. Finally, an investigation of the characteristics of the deposition area would be very interesting; however it is not necessary for the conclusions that are drawn here.

There is ambiguity about the temporal evolution of the bed characteristics after the end of the measurements. Specifically, past studies [*Melville and Raudkivi*, 1977; *Dargahi*, 1990] have identified an additional temporal phase before equilibrium. Therefore, it is possible that the new curves could be used to describe the evolution of scour or volume after the end of the presented measurements. However, the purpose of this study was not the investigation of the equilibrium conditions, rather the temporal and spatial characteristics of the phenomenon. Based on the presented results, it is expected that further variations in the characteristics of the scour evolution would take place at significantly low rates.

It is emphasized that the spatiotemporal characteristics of scour are expected to vary with different experimental parameters. Therefore, the purpose of this study is not to provide general rules, applicable to any bridge scour simulation. However, the physical interpretation of the results and their correlation with existing flow investigations in similar setups, provide insight towards the understanding of the phenomenon. Also, the presented results represent the most comprehensive description of the evolution of a scour hole and could be used for the interpolation and/or explanation of experimental results of lower resolution or accuracy. It should be noted that previously suggested distinctions of phases or areas, in existing studies, were not defined quantitatively; rather they were mostly based on visual observations or speculations based on incomplete datasets.

Finally, based on some of the most commonly used categorizations of bridge scour simulations [*Melville* 1997; *Sheppard et al.*, 2014], the experiment considered here is representative of clear-water cases (V/Vc=0.9), with intermediate flow shallowness (H/D=1.4), and uniform, non-cohesive and of intermediate relative coarseness (D/d50=43)

sediments, in a subcritical flow (Fr=0.4). This is probably the most commonly studied case of bridge scour that can be found in the literature.

3.5 Conclusions

A new computer vision based technique was applied to monitor the morphological characteristics of an evolving gravel bed at the base of a cylinder, in clear water scour conditions, with very high temporal and spatial resolution. Dynamic characteristics of the bed, such as point-wise bathymetry at various locations, slope around the cylinder and volumes of excavated material, were illustrated. The ensemble of the presented statistics led to the categorization of the scour phenomenon in two main phases, namely the initial ($0 \text{ min} < t < 9 \text{ min}$) and the development ($9 \text{ min} < t < 250 \text{ min}$) phases. Also, the area of the scour hole was divided in three main regions, which are the front ($0^o<\theta<25^o$), the sides ($25^o<\theta<135^o$) and the wake ($135^o<\theta<180^o$) regions. During both phases, the temporal evolution of scour at the front and the side regions and the volume of the excavated material are described by power laws. Although similar classifications have been attempted in the past, this is the first time that the distinction of phases and regions of scour is supported by detailed experimental data and a quantitative characterization of their limits and their statistics in time and space has been achieved (Table 1).

It is shown that during the brief initial phase of scour, the bed material was eroded very fast. The maximum scour rates were concentrated on the side region and their spatial distribution remained relatively constant, during the initial phase. At the end of this phase, the variation of the bed's bathymetry and radial slopes at different angles relative to the flow direction, resembled the distribution of the shear stresses in that area, as has been

described in past studies. Consequently, the maximum radial slope were observed at planes 40^o-50^o and were marginally greater than the sediments' angle of repose. It is speculated that the end of the initial phase and the beginning of the development phase was caused by the stabilization of the horseshoe vortex within the scour hole and resulted to important changes to the dynamic characteristics of the bed. Specifically, the distribution of the maximum scour rates was characterized by small patches whose location was constantly changing in time. During the development phase scour evolved faster at the front region and the wake region, and only small activity was observed in the side region. Remarkably, the radial slopes of the scour hole exhibit remained essentially the same during the development phase.

Overall, the experiment that was detailed here represents a very simple geometry that has been widely used in the past for investigations of the flow characteristics. This similarity allows for safer comparisons between the topography of the evolving scour hole as measured here, and the topology of the flow field as measured in previous physical or numerical models. The detailed characterization of the brief but very important initial phase is an element that is usually absent from most existing scour studies. This study contributes to the understanding of the scour phenomenon by providing insight towards the understanding of the dynamic interaction between the flow and the evolving bed.

Acknowledgements

The authors would like to thank the National Science Foundation (EAR 0738759) and the Research Office of the United States Army Corps of Engineers (ARO 53512-EV) for their support for this study. The first author is also grateful to the Gerondelis Foundation and the Edna Bailey Sussman Foundation.

References

Baker, C. J. (1980), The Turbulent Horseshoe Vortex, J Wind Eng Ind Aerod, 6(1-2), 9-23.

Bouratsis, P., P. Diplas, C. L. Dancey, and N. Apsilidis (2013), High-resolution 3-D monitoring of evolving sediment beds, Water Resour. Res., 49(2), 977-992.

Breusers, H. N. C., A. J. Raudkivi, and International Association for Hydraulic Research. (1991), Scouring, vii, 143 p. pp., A. A. Balkema, Rotterdam ; Brookfield.

Dargahi, B. (1989), The Turbulent-Flow Field around a Circular-Cylinder, Exp Fluids, 8(1-2), 1-12.

Dargahi, B. (1990), Controlling Mechanism of Local Scouring, J. Hydraul. Eng.-ASCE, 116(10), 1197-1214.

Devenport, W. J., and R. L. Simpson (1990), Time-dependent and time-averaged turbulence structure near the nose of a wing body junction, J. Fluid Mech., 210, 23-55.

Dey, S., and R. V. Raikar (2007), Characteristics of horseshoe vortex in developing scour holes at piers, J. Hydraul. Eng.-ASCE, 133(4), 399-413.

Escauriaza, C., and F. Sotiropoulos (2011a), Initial stages of erosion and bed form development in a turbulent flow around a cylindrical pier, J Geophys Res-Earth, 116.

Escauriaza, C., and F. Sotiropoulos (2011b), Reynolds Number Effects on the Coherent Dynamics of the Turbulent Horseshoe Vortex System, Flow Turbul Combust, 86(2), 231-262.

Guo, J. (2014), Semi-analytical model for temporal clear-water scour at prototype piers, J. Hydraul. Res., 52(3), 366-374.

Istiarto and Graf, W.H. 2001, Experiments on flow around a cylinder in a scoured channel bed, *Int. J. Sediment Res. 16(4)*, 431-444

Kirkil, G., and G. Constantinescu (2010), Flow and turbulence structure around an in-stream rectangular cylinder with scour hole, Water Resour. Res., 46(11), W11549.

Kirkil, G., G. Constantinescu, and R. Ettema (2009), Detached Eddy Simulation Investigation of Turbulence at a Circular Pier with Scour Hole, J. Hydraul. Eng.-ASCE, 135(11), 888-901.

Koken, M., and G. Constantinescu (2009), An investigation of the dynamics of coherent structures in a turbulent channel flow with a vertical sidewall obstruction, Phys Fluids, 21(8).

Kothyari, U. C., W. H. Hager, and G. Oliveto (2007), Generalized approach for clear-water scour at bridge foundation elements, J. Hydraul. Eng.-ASCE, 133(11), 1229-1240.

Kumar, A., U. C. Kothyari, and K. G. R. Raju (2012), Flow structure and scour around circular compound bridge piers - A review, J Hydro-Environ Res, 6(4), 251-265.

Link, O., F. Pfleger, and U. Zanke (2008), Characteristics of developing scour-holes at a sand-embedded cylinder, Int J Sediment Res, 23(3), 258-266.

Lu, J. Y., Z. Z. Shi, J. H. Hong, J. J. Lee, and R. V. Raikar (2011), Temporal Variation of Scour Depth at Nonuniform Cylindrical Piers, J. Hydraul. Eng.-ASCE, 137(1), 45-56.

Melville, B. (1997), Pier and Abutment Scour: Integrated Approach, Journal of Hydraulic Engineering, 123(2), 125-136.

Melville, B. W., and A. J. Raudkivi (1977), Flow characteristics in local scour at bridge piers, J. Hydraul. Res., 15(4), 373-380.

Melville, B. W., and Y. M. Chiew (1999), Time scale for local scour at bridge piers, J. Hydraul. Eng.-ASCE, 125(1), 59-65.

Mia, F., and H. Nago (2003), Design method of time-dependent local scour at circular bridge pier, J. Hydraul. Eng.-ASCE, 129(6), 420-427.

Oliveto, G., and W. H. Hager (2002), Temporal evolution of clear-water pier and abutment scour, J. Hydraul. Eng.-ASCE, 128(9), 811-820.

Paik, J., and F. Sotiropoulos (2010), Numerical simulation of strongly swirling turbulent flows through an abrupt expansion, Int J Heat Fluid Fl, 31(3), 390-400.

Radice, A., and C. K. Tran (2012), Study of sediment motion in scour hole of a circular pier, J. Hydraul. Res., 50(1), 44-51.

Radice, A., G. Porta, and S. Franzetti (2009), Analysis of the time-averaged properties of sediment motion in a local scour process, Water Resour. Res., 45, 12.

Roulund, A., B. M. Sumer, J. Fredsoe, and J. Michelsen (2005), Numerical and experimental investigation of flow and scour around a circular pile, J. Fluid Mech., 534, 351-401.

Sabersky, R. H., A. J. Acosta, and E. G. Hauptmann (1989), Fluid flow : a first course in fluid mechanics, 3rd ed., xii, 537 p. pp., Macmillan ; Collier Macmillan, New York London.

Sheppard, D. M., B. Melville, and H. Demir (2014), Evaluation of Existing Equations for Local Scour at Bridge Piers, Journal of Hydraulic Engineering, 140(1), 14-23.

Sheppard, D. M., H. Demir, B. W. Melville, National Research Council (U.S.). Transportation Research Board., National Cooperative Highway Research Program., American Association of State Highway and Transportation Officials., and United States. Federal Highway Administration. (2011), Scour at wide piers and long skewed piers, 55 p. pp., Transportation Research Board, Washington, D.C.

Simarro, G., L. Teixeira, and A. H. Cardoso (2009), Closure to "Flow Intensity Parameter in Pier Scour Experiments" by Gonzalo Simarro, Luis Teixeira, and Antonio H. Cardoso, J. Hydraul. Eng.-ASCE, 135(2), 155-155.

Yanmaz, A. M., and O. Kose (2009), A semi-empirical model for clear-water scour evolution at bridge abutments, J. Hydraul. Res., 47(1), 110-118.

List of Figures

Figure 1. a. View of the hydrulic flume; b. view of the cameras recording the bed during the experiment.

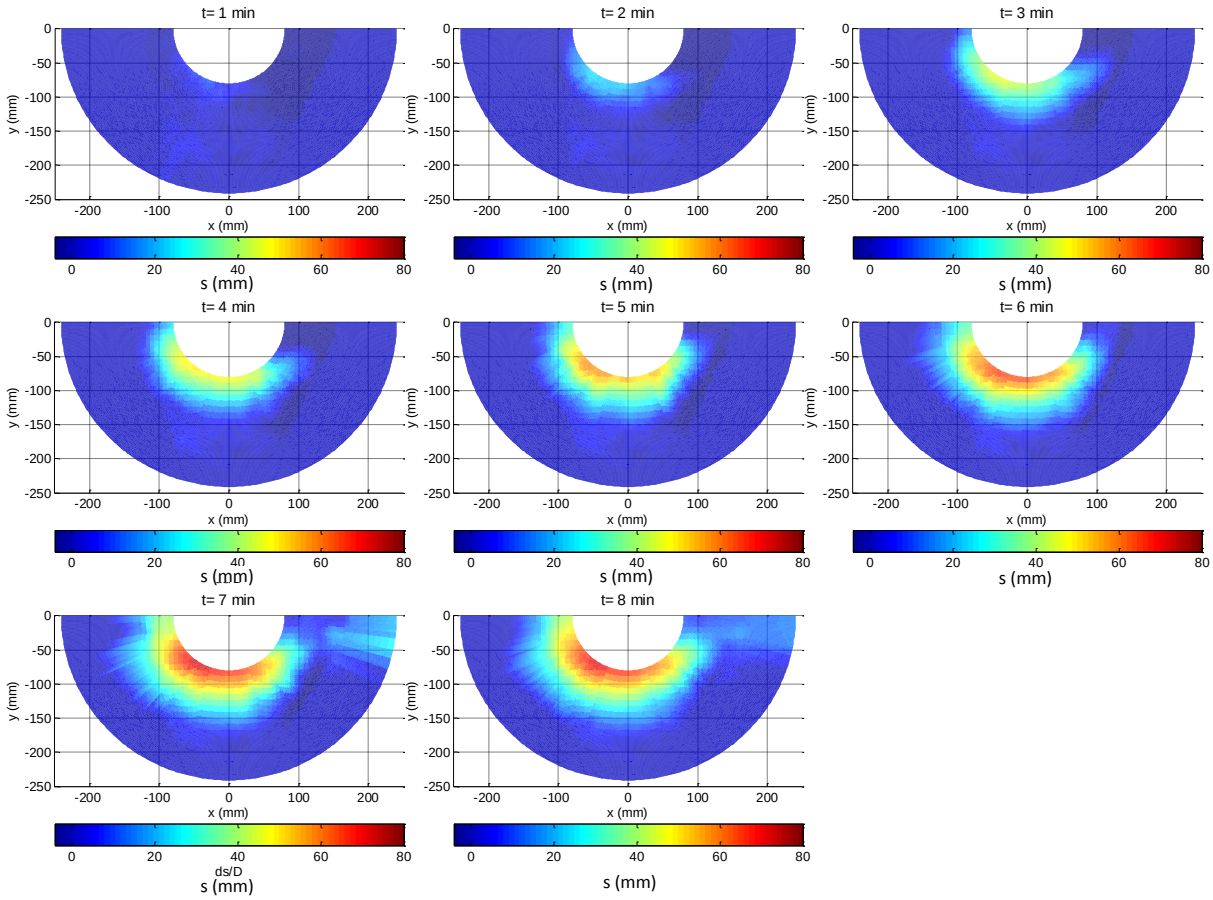

Figure 2. Scour depth contour maps during the first 8 minutes of the experiments. Flow direction is from left to right.

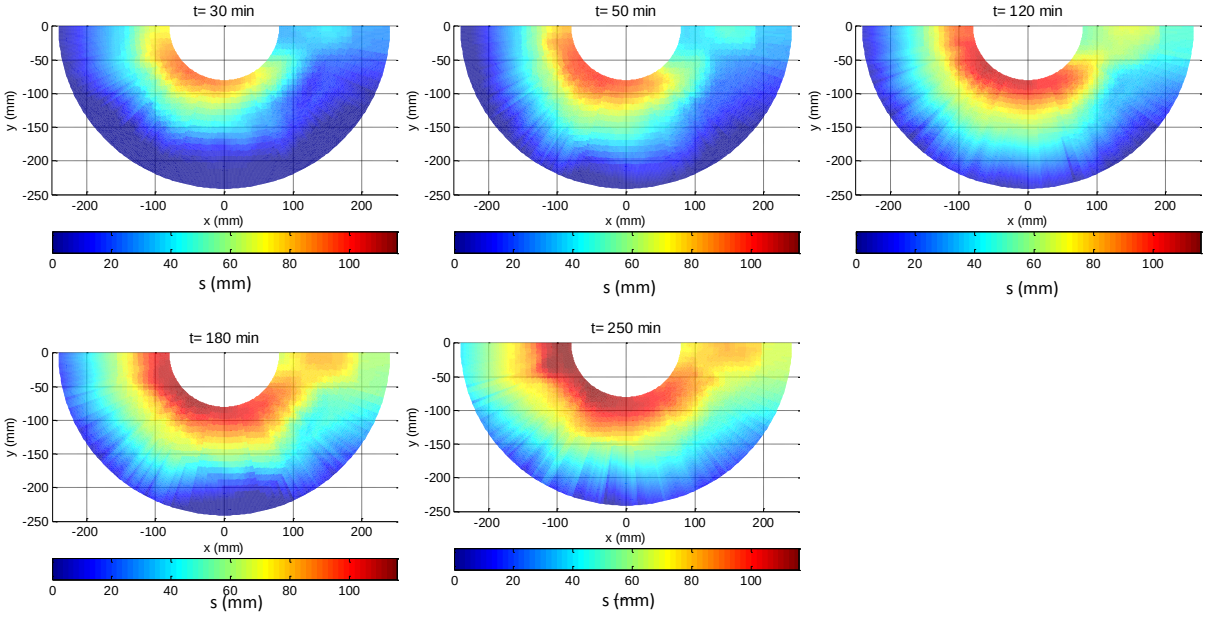

Figure 3. Scour depth contour maps at various instants.

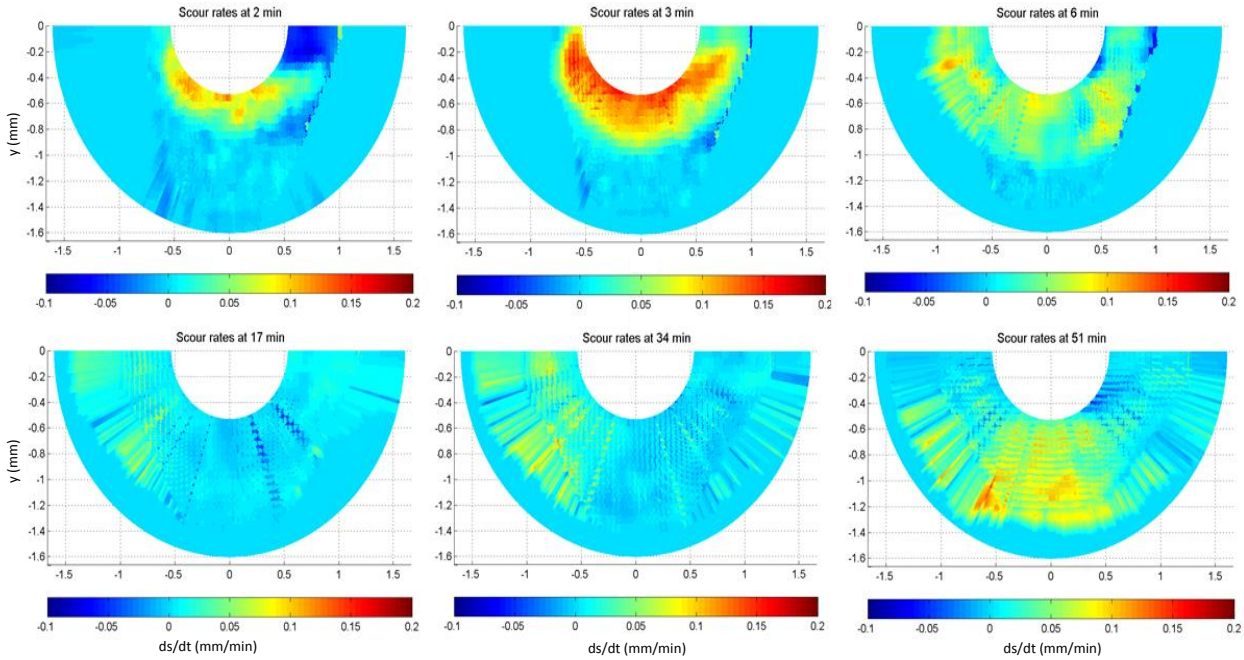

Figure 4. Instantaneous scour rate distributions.

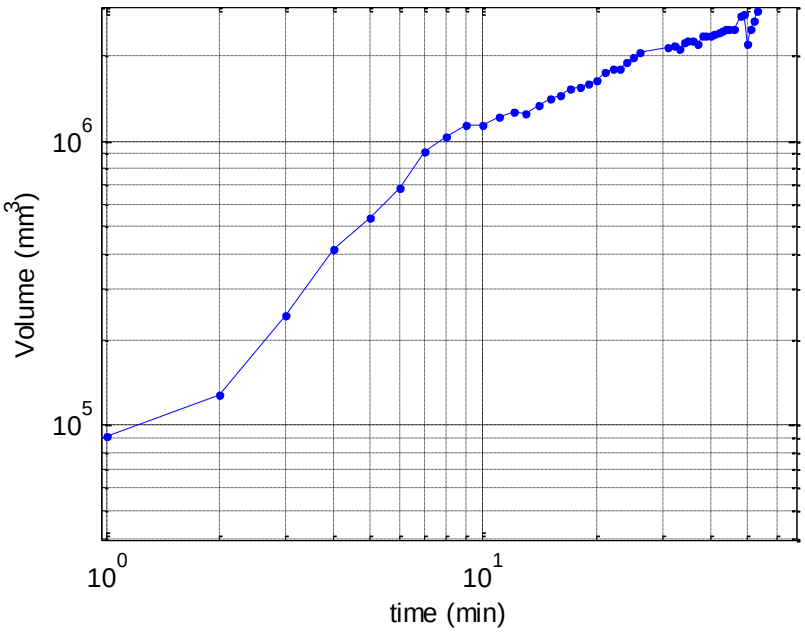

Figure 5. Volume of the scour hole.

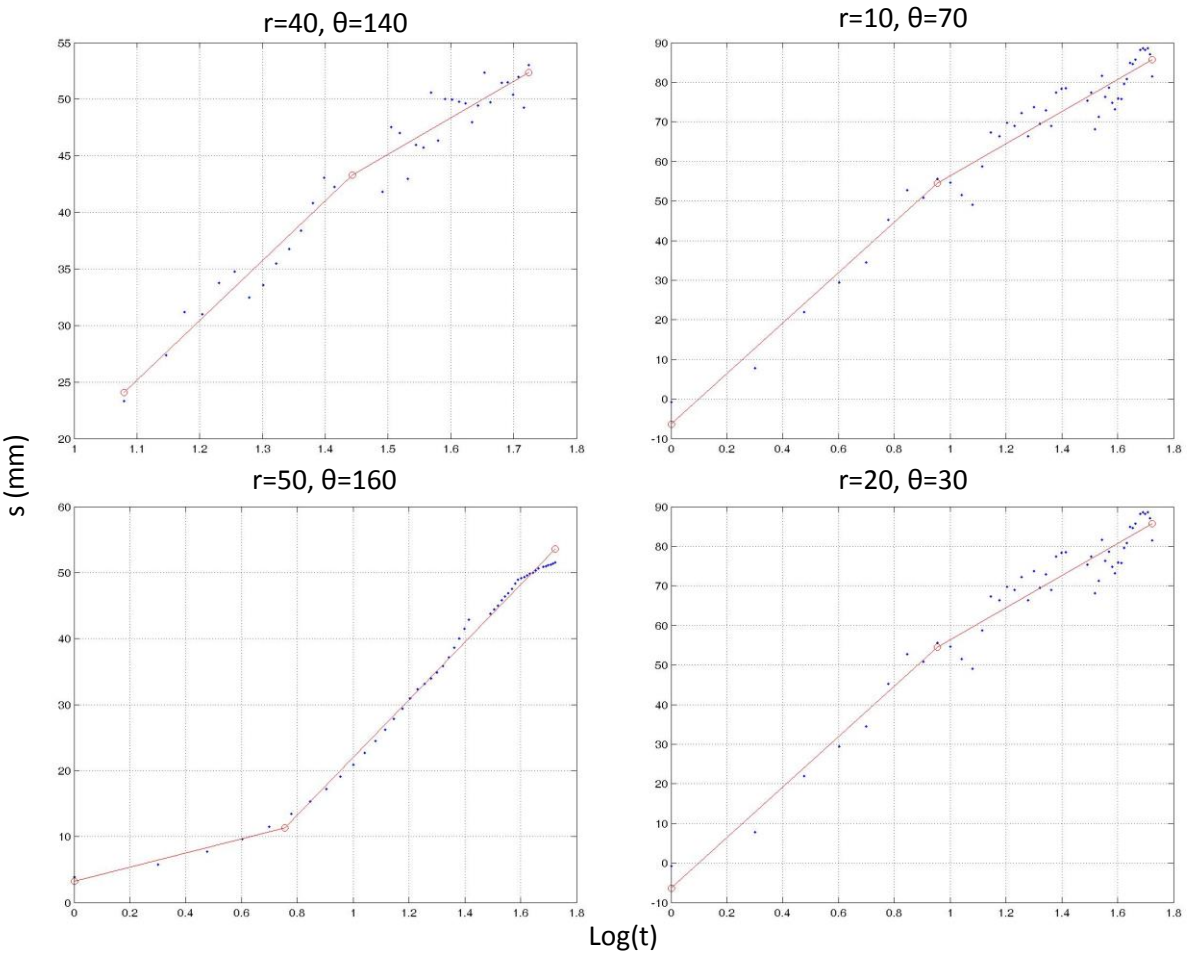

Figure 6. Examples of the piecewise curve fitting for the temporal functions of scour.

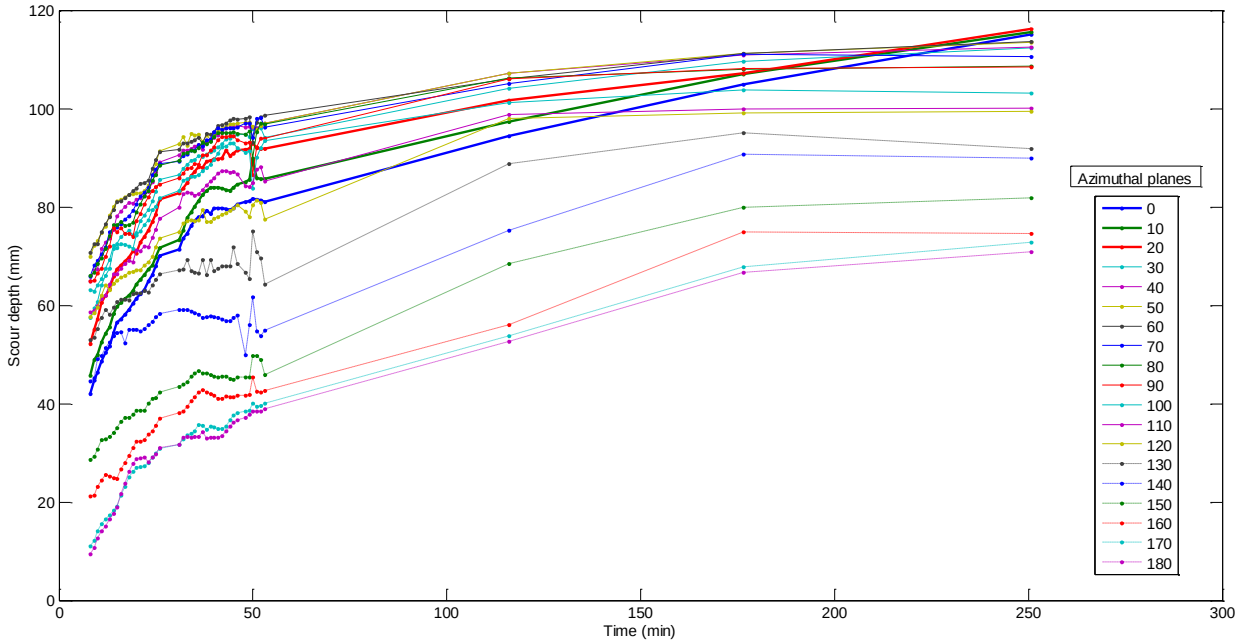

Figure 7. Temporal evolution of scour at locations with r=10mm and θ ranging from 0º to 180º.

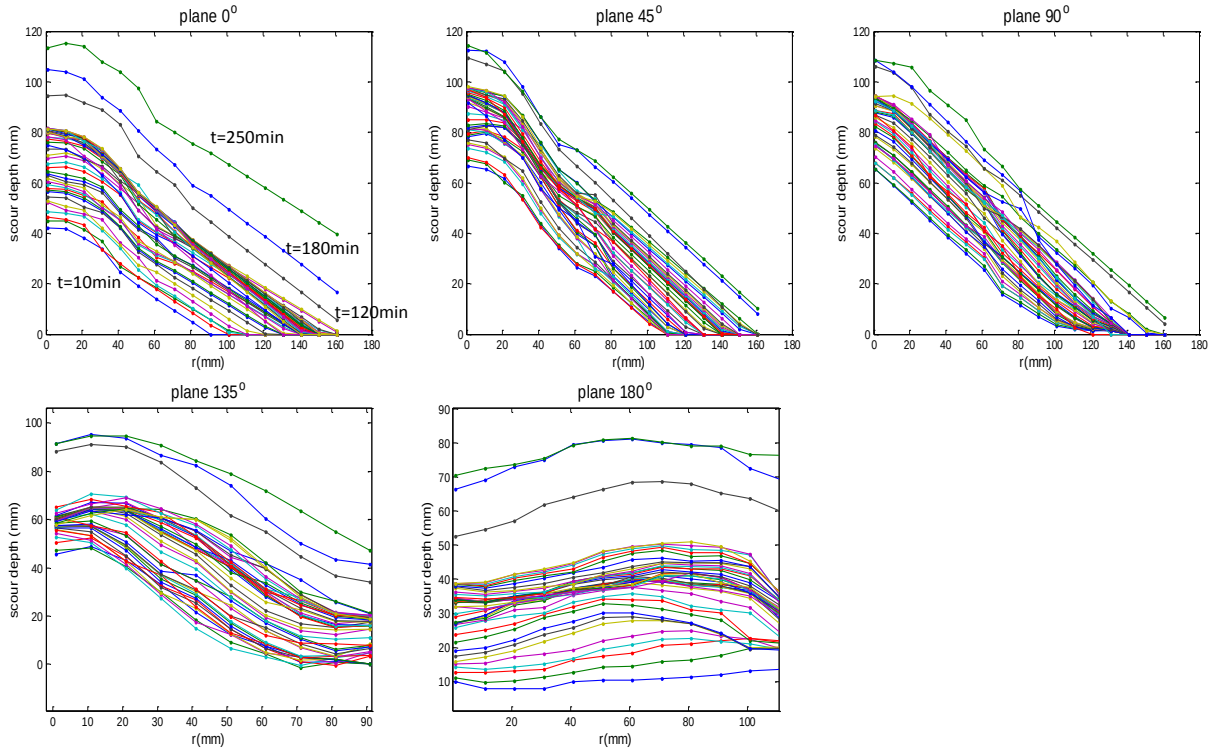

Figure 8. Scour depth against radial distance from the surface of the cylinder, for various instants after t=9min, in 5 angular planes, around the cylinder.

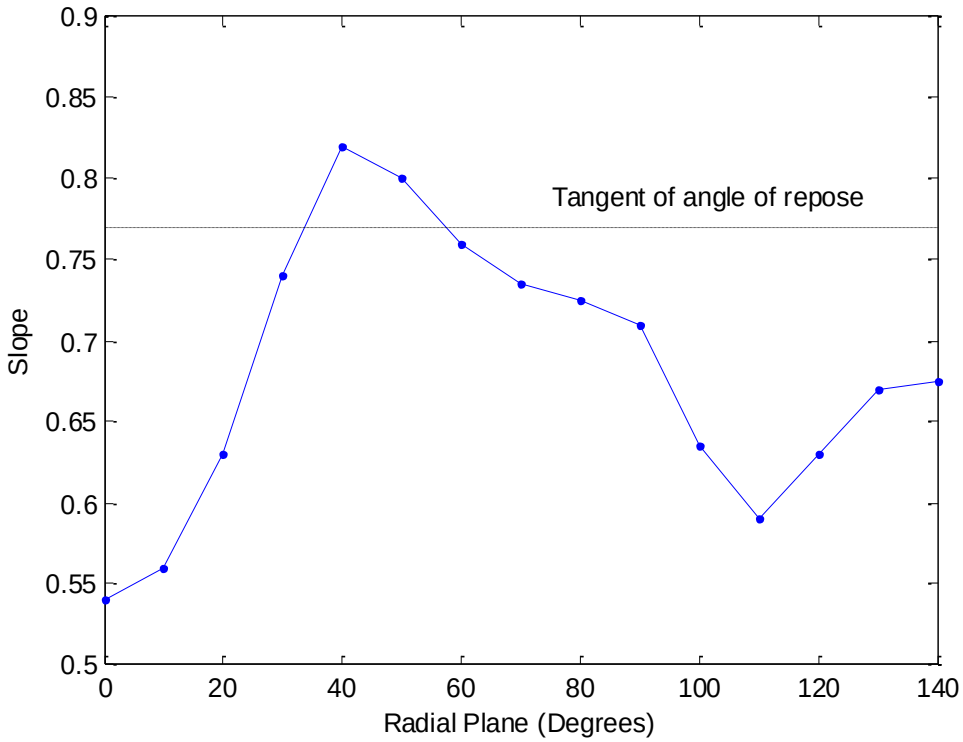

Figure 9. Average slope of radial profiles, at the front and the sides of (or around) the cylinder during the development phase.

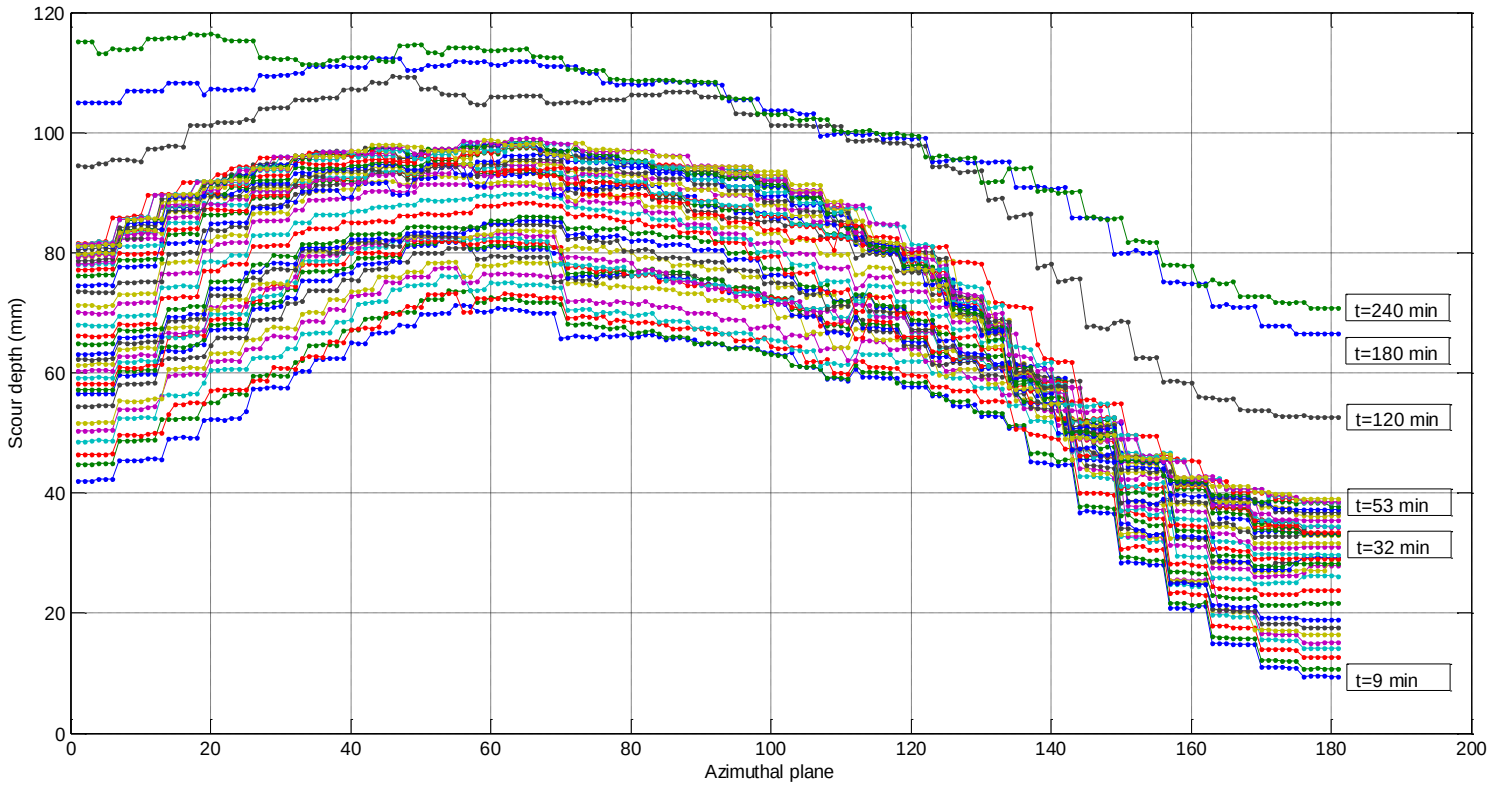

Figure 10. Scour depth as a function of the angle of the plane relative to the flow direction, at r=5mm, for various instants, after t=9min

List of tables

Table 1. Quantitative characteristics of the various phases and regions.

Phase	Region	Terminal scour depth (mm)	Location of max scour depth (θ, r)	Terminal excavated volume (mm^3)	Equations				
					s vs. t	s vs. θ	s vs.r	Volume vs. t	Slope vs. θ
Initial (0 min<t<9 min)	Front (0^o<θ<20^o)	46.04	(20,30)	$1.14*10^6$	$s=t^a$	-	s=ar+b	$s=t^a$	-
	Side (20^o<θ<125^o)	73.83	(60, 30)		$s=t^a+b$				
	Wake (125^o<θ<180^o)	23.91	(175, 180)		-		$s=ar^3+br^2+cr+d$		
Development (9 min<t<250 min)	Front (0^o<θ<20^o)	116.5	(0, 20)	$4.76*10^6$	$s=t^a$	s=asin(bθ)+c	s=ar+b	$s=t^a+b$	s=asin(bθ)+c
	Side (20^o<θ<125^o)	114.2	(60, 5)		$s=t^a+b$				
	Wake (125^o<θ<180^o)	80.5	(175, 100)		-		$s=ar^3+br^2+cr+d$		-

Chapter 4. Scour and Flow around Prototype Bridge Foundations

Abstract The prediction of local scour at the base of bridge piers remains a challenging engineering problem. The plethora of small scale laboratory and numerical simulations cannot fully replicate the mechanisms of scour in the way they occur at prototype scale bridges. This shortcoming is mainly attributed to the unknown scale effects that are inherent in most existing model studies that cannot completely satisfy dynamic similarity. Here, we present the results of two clear water experiments with large cylindrical piers that are carried out at near-prototype conditions. The only parameter that varies between these two experiments is the pier diameter. The corresponding pier diameter based Reynolds numbers, Re_D, are $9.1*10^5$ and $6.1*10^5$. The bridge scour phenomenon is described via scour evolution measurements at multiple locations and velocity measurements over the developing scour hole. The dimensionless coordinates of the measurement points are identical for both experiments, allowing for direct comparisons of the results. The quantitative comparisons between the two experiments and the qualitative comparisons with other small scale laboratory flume studies, provide insight on the effects of Re_D on flow characteristics and scour development at large scales. For the higher Re_D experiment the shear stresses at the wake of the pier are significantly increased. As a result scour is more pronounced and the slope of the scour holes at the wake is steeper, affecting the morphology of the scour hole at various planes around the pier. On the upstream edge of the pier, the depth and span of scour scales very well with the pier diameter. It is shown that only for the higher Re_D case the flow statistics point towards an organized turbulent

horseshoe vortex (THV). However, the shear stresses close to the bed, upstream of the pier, are similar between the two cases.

4.1 Introduction

Local scour at the base of bridge piers is the leading cause of bridge failures [*Briaud* 1999; *Wardhana*; *Annandale* 2006; *Melville and Coleman* 2000; *Shirole and Holt*, 1991]. The accurate prediction of the scour depth during flood events and the effective design of countermeasures for the mitigation of scour are some of the most extensively studied problems in hydraulic engineering. Despite the large amount of literature in this area, these problems continue to pose significant challenges and considerable research efforts in this area are ongoing.

The majority of the existing scour prediction formulae show substatial differences when their results are mutually compared, even though in many cases they have been developed following similar procedures and concepts [*Sheppard et al*., 2012]. Unfortunately, the very scarce field data that are currently available cannot resolve these disagreements and assist in selecting the most appropriate formula. For most of the available field data, the only recorded parameter is the maximum scour depth at a single instant, after the occurrence of multiple events of varying duration and intensity. Comparisons have shown the tendency for overprediction of the scour depth that leads to uneconomical design [*Melville and Coleman*, 2000]. Regarding the numerical models for the coupled simulation of the flow and scour around piers, only a few studies have shown promising results; however, their development is at a relatively early stage and they cannot be used for design purposes, yet.

Also, the design of the countermeasures is commonly based on engineering experience and it does not typically take into account the physics of the phenomenon.

The inadequacy of some of the existing methodologies is attributed to the lack of understanding of the complex interaction between the three-dimensional turbulent flow field, the erodible bed and the structure. One of the main reasons for that is the fact that our understanding of the bridge scour phenomenon is based primarily on the results from physical or numerical simulations with models that are orders of magnitude smaller than field cases.

The most common approach for the investigation of bridge scour and the development of prediction tools, is the derivation of semi-empirical formulas via laboratory experiments and dimensional analysis. Most of these studies focused on the prediction of the equilibrium scour depth only (e.g. [*Arneson et al*., 2012; *Melville*, 1997]). A smaller number of similar studies have resulted in the derivation of formulas for the temporal evolution of scour [*Oliveto and Hager*, 2002; *Kothyari et al*., 2007; *Melville and Chiew*, 1999; *Unger and Hager*, 2007]. A thorough review and evaluation of the existing formulas has been presented by *Ettema et al.* [2011] and *Sheppard et al.* [2014]. The dimensionless parameters that are most commonly used for the estimation of scour around cylindrical piers, on cohesionless beds are: H/D, D/d_{50}, V/V_c or u_*/u_{*c}, σ_g, t/t_e, or t_*; where H: approach flow depth, D: pier diameter, d_{50}: median sediment size, V: approach flow velocity, V_c: critical velocity for sediment entrainment, u_*: shear velocity, u_{*c}: critical shear velocity, σ_g: geometric standard deviation of the sediment diameter, t:time, $t_*= tV/D$, t_e: time required to reach equilibrium for a given geometry and flow conditions. Also, a few studies have emphasized the importance of the densimetric Froude number and the pier-based

Froude number in the development of the scour depth [*Oliveto* 2002, 2005; *Kothyari*, 2007; *Ettema*, 1998; *Lee and Sturm*, 2009]. From all of the aforementioned dimensionless parameters the only one that cannot be easily replicated in small scale models is D/d_{50} (i.e. sediment roughness). The scaling effects of the latter parameter have been investigated by *Sheppard et al.* [2004], *Sturm and Lee* [2009] and *Lanca et al.* [2013] and functional relationships were derived. One of their main findings was that the nondimensionilized scour depth is affected by D/d_{50} even for very high values of this parameter (>1000); thus, this effect should be taken into account for the interpretation of small scale studies.

Important insight on the mechanism of scour has been gained by the investigation of flows around wall-mounted obstacles. *Baker* [1979], *Danvenport and Simpson* [1991] and *Dargahi* [1989], have described the most fundamental features of junction flows that they observed in water-flume and wind-tunnel experiments. They reported observations with regards to the number, the size and frequency of the horseshoe and wake vortices and they investigated the mechanisms that create them. Following studies reported the characteristics of the flow field around model piers, over sediment beds, in small-scale physical and numerical experiments. *Kumar and Kothyari* [2012], *Dey and Raikar* [2007], *Istiarto and Graf* [2001] and *Ettema and Constantinescu* [2009] carried out flow measurements with Acoustic Doppler Velocimeters (ADVs) over equilibrium or developing scour holes that were artificially stabilized. *Escauriaza and Sotiropoulos* [2011b] in their numerical simulations revealed very detailed aspects of the flow, and correlated the frequency of the vortices upstream of the pier and the distribution of the shear stresses with scour periodicities and rates. Further, detailed results from numerical

simulations, along with validating physical experiments were presented by *Kirkil and Constantinescu*, [2009], and *Kirkil et al.* [2009].

A very important aspect that was revealed by some of these studies, is how even small variations in the pier-based Reynolds number (Re_D=UD/ν, where ν: kinematic viscosity), can completely alter the topology of the flow. Similarly, *Dargahi* [1989] presented detailed descriptions of the flow around a cylinder, mounted on a flat bed, in experiments with Re=8,400-46,000. He found that the number and periodicity of the vortices upstream of the cylinder and the shedding frequency of the wake vortices varied with Re_D. Although he did not report a functional relationship between any flow characteristics and the Re_D, the strong effects of this parameter were made evident. Dargahi's findings were also replicated in the numerical simulations by *Escauriaza and Sotiropoulos* [2011a], who also highlighted the differences in the topology of the instantaneous flow field and the distribution of the shear stresses around a cylinder, for two different Re_D ($Re_{D1}=2*10^4$, $Re_{D2}=0.9*10^4$). Also, *Koken and Constantinescu* [2009] showed major differences between the flow topology, and the instantaneous and average stresses on a flat bed around an abutment, for two Re_D ($Re_{D1}=1.8*10^4$, $Re_{D2}=50*10^4$). In the latter study, the flow simulations showed increased dimensionless stresses for the experiment with the highest Re_D, contrary to the expected trend that would justify the aforementioned overprediction tendencies. *Ettema et al.*, [2006] also reported significant differences in the vorticity and shedding frequency of the wake vortices, over sediment beds, for different Re_D and suggested that the scour depth is also affected.

Despite the pronounced effects on the flow for even small changes in the Reynolds number, this parameter is rarely discussed in the bridge scour literature, which is partially attributed

to the fact that dynamic similitude cannot be achieved in small scale studies. Also, it is expected that, at prototype bridges, the viscous effects are not important, as far as the flow on the upstream face of piers is concerned. This does not suffice to ignore completely the Re effects from the similitude analysis for two main reasons: 1) changes in Re are expected to affect other important flow characteristics such as the position of the separation points at the sides of the pier, and the shedding frequency and vorticity of the wake vortices; and 2) viscous effects are also important for the turbulent horseshoe vortex (THV) characteristics in the range that most of the bridge scour experiments have been carried out; thus, the effects of Re are inherent in almost every bridge scour study. Therefore, both flow and scour observations at cases with prototype Re, are imperative for the correct description of bridge scour and the examination of the scale effects.

Large scale experiments were carried out by *Sheppard et al.* [2004] for Re_D that ranged up to $5*10^5$. In these experiments the emphasis was on the effects of D/d_{50} on the evolving and equilibrium scour depths. A similar approach was followed by *Lanca et al.* [2013], that also compared their data against previously developed formulas, in experiments with maximum $Re_D = 1.3*10^5$. Additionally, *Ettema et al.* [2009], discussed variations in the scour depth and the frequency and size of wake vortices for experiments with maximum $Re=1.9*10^5$.

Here we present two experiments that were carried out at near-prototype conditions. We describe the evolution of the scour depth at various locations around the pier along with flow and turbulence statistics over a developing scour hole. The nondimensionalized coordinates of the measured quantities are the same in both experiments, to allow for direct comparisons. In these experiments all dimensions and flow characteristics are the same,

except for the pier diameters. The Reynolds numbers are $Re_{D1}=9.14*10^5$ and $Re_{D2}=6.2*10^5$ and are the highest values that have been reported from laboratory studies. The instrumentation and the careful design of the experiments allow for the first time a detailed description of conditions that are representative of floods at bridge sites. We describe the scour depth and the shape of the scour hole, during scour development. Then the similarities and the differences between the two experiments are explained via the investigation of the flow after several hours of scour and before equilibrium has been reached. Differences and similarities between the average velocities, turbulence statistics and scour evolution are discussed in detail.

The experimental setup, instrumentation, and data-processing methodology are described in the next section. The temporal development of scour is described in Section 3.1 and the characteristics of the flow field upstream and downstream of the pier are discussed in Sections 3.2 and 3.3. The main implications of the presented results are summarized in Section 4.

4.2 Setup and Procedures

4.2.1 Facilities and Experiments

The experiments were carried out at the Environmental Research and Development Center (ERDC) of the US Army Corps of Engineers, located in Vicksburg, MS. The flume used during the present experiments was 39 m long, 7.3 m wide and 3.1 m deep. The sediments were well-sorted pea gravels with median diameter d_{50}=14.2 mm and geometric standard deviation σ_g=1.4. The height of the sediment layer was 1.5 m. At the entrance of the flume, two layers of 0.9 m-wide gabion-baskets with rip-rap, were placed before the gravels to

help create uniform flow. The center of the pier was located 24 m downstream of the entrance. An adjustable weir was positioned at the downstream end of the flume, to control the depth of the flow. Figure 1 shows a view of the flume.

Six pumps were used to draw water from a very large reservoir into the flume. The cumulative capacity of the pumps was $5.66 m^3/s$. The unobstructed depth-average velocity was $V_o = 0.805$ m/s, the flow depth was H = 0.6 m and the slope of the free surface was S = 0.1%. The experiments were carried out in the clear water regime, with the ratio of shear velocity to critical shear velocity being: $u_*/u_{*c} = 0.7$. For the two experimental runs that are presented here, the only changing dimensional parameter was the pier diameter ($D_1 = 91.44$ cm and D_2=60.96 cm). The experiment with the largest pier was carried out twice to ensure the repeatability of the results. The corresponding pier diameter based Reynolds numbers were $Re_{D1} = 9.1*10^5$ and $Re_{D2} = 6.1*10^5$. The experiments lasted for $t_1 = 10$ h and $t_2 = 6$ h, that correspond to the same dimensionless time (t_*). The important dimensionless parameters of both experiments are displayed in Table 1.

For the measurements of the flow velocity, we used six Acoustic Doppler Velocimeters (ADVs). One of the ADVs was a 16 MHz MicroADV and was collecting single-point measurements at 50 Hz. Two of the ADVs were 10 MHz VectrinosI and were collecting single-point measurements at 200 Hz. The three remaining ADVs were 10 MHz VectrinosII that were carrying out velocity profile measurements at 100Hz. Each profile increment was composed by 30 measurements that were 1mm apart. The VectinosI and VectrinosII were synchronized using Polysync data collection software. For the bathymetric measurements, 11 Acoustic Range Finders (ARFs) were employed. The ARFs

were 5 MHz cylindrical acoustic transducers with diameter and height equal to 2.54 cm and 5.08 cm, respectively. They were collecting data at 5 Hz.

Auxiliary measurements were carried out with additional instrumentation to monitor the experimental conditions in real-time. A transparent window on the pier surface and a video camera that was mounted within the pier, allowed for the recording of scouring at part of the scour hole, upstream of the pier. An adhesive measuring tape was placed on the window of the pier and was used to monitor the scour depth. Additionally, the flow depth, the temperature of the water and a rough estimate of the discharge were monitored using adhesive scales on the sidewalls of the flume, thermometers and an electromagnetic FloMate (Model 2000), respectively.

Above the installed pier, a system of three catwalks was built. Two horizontal rails that were positioned on the planes of symmetry upstream and downstream of the pier, were mounted on the pier and the catwalks. Five ADVs and an array of 8 ARFs were attached on vertical rods that were mounted on the horizontal rails and could be translated horizontally and vertically. Adhesive scales were placed on the rods and the rails. This configuration allowed for the precise translation of the instruments on the plane of symmetry by the users who were standing on the catwalks. Also, four acoustic range finders were firmly attached on the perimeter of the pier at 25^o, 45^o, $90^o$and 135^o relative to the flow direction. Figure 2 provides a view of the instrumented pier and the catwalks. Figure 3 shows a schematic of the set up and the possible positions of the instruments. The exact positions of the remaining ARFs and the ADVs were different for each experiment. Details are presented at the following sections.

Before the experiments, the horizontal rails were fixed over the pier and the rods with the instruments were mounted on them. Extensive validation measurements were carried out to verify that the orientation of the ADVs and the ARFs was correct. Then the gravel bed was leveled using thick metallic beams whose length spanned the width of the flume. These beams were mounted on two rails that were installed on the sidewalls of the flume at the desired elevation and slope. Preliminary tests were carried out to verify that the mounting configuration could hold the instruments firmly and prevent vibrations. Also, quality checks were performed to ensure the instruments were working properly.

While the sluice gate was fully closed, a pump was turned on and the water level within the flume slowly increased. The sluice gate was gradually lifted while additional pumps were initiated. The timing of the steps of this procedure was determined through trial and error, prior to the experiments. Scouring commenced a few minutes (less than 5 min) before the desired flow conditions were reached. The experiments contained two main phases. The first phase commenced with the introduction of the flow and at its conclusion the scour rates were less than 1cm/sec. The exact duration of phase#1 for the two experiments were t_1 = 10 h and t_2 = 6 h, that correspond to the same dimensionless times. During this phase, the temporal evolution of scour, flow-velocity, and pressure on the surface of the pier were measured with the ARFs, the ADVs and the pressure transducers; however, only bathymetric results will be presented here for Phase#1. During the second phase, which lasted for about 5 hours in both experiments, vertical velocity profiles and bathymetric profiles on the plane of symmetry upstream and downstream of the pier were measured. The duration of the velocity measurements at every location was 3-5 minutes long. The setup did not allow for velocity measurements very close to the free surface (i.e. less than

10cm). The bathymetry measurements, showed that during the second phase, the topography of the scour hole experienced very small variations, on the order of 2cm. After the completion of phase 2, the flume was carefully drained with gradual adjustments of the sluice gate.

The purpose of this work was to simulate prototype conditions within a carefully controlled environment. For this reason, it was chosen not to attempt to stabilize the surface of the scour hole via a sealant or another adhesive to avoid removing the effects of porosity on the flow.

4.2.2 Data processing

A simple filtering routine was applied to the bathymetric data to remove outliers and improve their quality. At first, sub-samples of 101 measurements (20 seconds long) were defined around every observation. Observations whose absolute difference from the median of the respective sub-sample were larger than three times the standard deviation, were removed. A handheld measuring scale was used to carry out crude preliminary validation measurements, before the leveling of the bed. Through these measurements, it was concluded that this filtering routine is sufficient, since the average observed error less than 2cm.

A more thorough filtering procedure was required for the velocity measurements. At first, the time-series were filtered based on the signal to noise ratio (SNR) and the correlation score, which are common quality indicators of ADV data [*Wahl*, 2000]. If the SNR or the correlation score of a single velocity component were less than 10 or 50 respectively, the entire observation was removed. Additionally, the velocity signals were filtered using the

despiking algorithm that was introduced by *Islam and Zhu* [2013]. This algorithm is a modification of the widely used phase space thresholding technique [*Goring and Nikora*, 2002]. Eventually, if more than 60% of the observations from a time-series were removed, then the entire measurement was removed.

The selection of this filtering scheme was the result of an extensive trial and error procedure. Data samples were filtered for various values of SNR and correlation score thresholds. Also, the classic phase-space thresholding by *Goring and Nikora*, [2002] and a modified phase-space thresholding by *Parsheh et al.* [2010] were tested. Although no validation velocity measurements were available to indicate the most effective filtering scheme, inspection of the average velocities and the turbulence statistics suggested that the selected scheme could resulted in vertical profiles of higher fidelity. Modified versions of the USGS codes of *Gunawan and Neary* [2011] were used in this procedure, along with in-house Matlab codes.

The aforementioned filtering routine was adequate for the processing of the data from the VectrinoI and the MicroADV. On the other hand, the data from the VectrinoII required further processing. Visual inspection of the results indicated that parts of the vertical profiles of the velocities and the turbulence statistics were clearly erroneous. After extensive experimentation with different filtering schemes, it was decided that the only effective approach was the complete removal of measured points from the tails of every profile increment. For the vertical profiles of the average velocities, the top and bottom 5 cells were removed and then a fourth order polynomial was fitted to the entire vertical profile. For the turbulence statistics, only the central point of each profile increment was used.

4.3 Results and Discussion

The bathymetric measurements of phase#1 and the flow measurements of phase#2 are presented in the following sections. The pier diameter (D) and the depth-averaged approach velocity (Vo) have been used for the normalization of most of the parameters that are presented in this paper. The shear velocity (u_*) is used in a later section for the normalization of turbulence statistics. The x-axis is in the streamwise direction, positive downstream, and the z-axis is perpendicular to the channel bottom. The position (x/D = 0, z/D = 0) coincides with the center of the pier, at the level of the unscoured bed.

4.3.1 Scour Evolution

Figure 4 shows the scour depth evolution at 6 locations around the larger pier. Each location is 1.27 cm away from the surface of the pier and is denoted by the angle of the plane within which it is located relative to the flow direction ($\varphi = 0^o$, 25^o, 45^o, 90^o, 135^o, 180^o).

As it has been frequently observed in small scale investigations and explained in numerical studies, scour initiated at the sides of the pier (45^o-90^o), where the initial shear stresses are expected to be higher (e.g. [*Kirkil and Constaninescu*, 2007]). At the beginning of our scour experiments, the maximum depth was observed at the 90^o plane. At $t_* = 3400$, the maximum scour depth was located at the 45^o plane. The location of the maximum scour depth remained unchanged until the end of the measurements (t = 8 hours, or $t_* = 25000$). After t_*=3400 and until the end of the measurements, the ranking of scour depth at each plane from highest to lowest, was as follows: 45^o, 90^o, 25^o, 0^o, 135^o, 180^o. For the entire duration of the measurements, the scour depth profiles were qualitatively similar at the area within the 0^o - 90^o planes, with the maximum variation being equal to 0.1D. Towards the

wake of the pier, the scour depth was significantly reduced and the minimum values were observed at 180^{o}. The maximum and the minimum observed scour depths at t_{*} = 25000 were equal to 0.5D and 0.1D, respectively.

Contrary to what is frequently observed in small scale studies, the scour depth at the 0 ^{o} plane remained smaller around the first half of the pier. Specifically, *Sheppard et al.* [2011], and *Melville and Chiew* [1999] have reported that soon after the commencement of scour, the maximum depth is expected at 0 ^{o}. Judging by the rates of scour towards the end of the experiment and extrapolating the curves, it can be crudely estimated that only after several days could the maximum scour position migrate to the face of the pier.

The scour evolution time-series at each location within the 0 ^{o} -90 ^{o} planes could be approximated very well with either logarithmic or power functions, as has been reported in small scale studies [*Oliveto and Hager*, 2002; *Unger and Hager*, 2007; *Melville and Chiew*, 1999]. This was not the case for the scour depth in the wake region, which must be described by a more irregular curve.

The periodic fluctuations that are observed (Fig. 4) in the scour time-series were intentionally not smoothened. Even though all the time-series have been processed following the same procedure, the magnitude of the fluctuations at the wake (i.e 135^{o}) were significantly higher. Representations of the data in the frequency domain (not included here) show that near the wake there are strong periodic components in the scour data. In both experiments, the dominating frequency components were between 0.15-0.65 Hz and the power spectral energy was highest at the beginning of scour. Towards the end of the experiment it was reduced to about 50% of the original values. This means that the

fluctuations that are observed in Fig. 4 tend to have a reduced magnitude in time. On the other hand, scour at the front of the pier did not include any dominant periodic components. Although part of these fluctuations in the scour depth is expected to be noise, they should also be partially attributed to the amount of suspended sediment at every location. The time-series of scour at the wake region show that even though the average scour depth remains almost constant, there is significant sediment mobility (i.e. strong fluctuations) that is not reduced with time.

The comparison of the scour evolution at the same locations around the smaller pier (not included here) shows very similar trends. The most noteworthy difference is that scour at the 90 ^{o} plane was smaller compared to the 45 ^{o}, 25 ^{o} and 0 ^{o} planes. Also, as it is illustrated next, for the smaller pier experiment the initial scour rates were.

In Figure 5 the nondimensionalized scour depth evolution of the small and the large pier are compared. The similarity of the scour evolution for the two experiments in the 0 ^{o} and 25 ^{o} planes is remarkable. These experiments suggest that in this range of Reynolds numbers, the scour depth at the face of the pier scales perfectly with the pier diameter.

In the 45 ^{o} to 180 ^{o} planes, the nondimensionalized scour was larger in the large pier experiment. When moving towards the wake, a gradual increase in the difference between the scour depths is observed. Specifically, the nondimensional scour depth difference, between the two experiments, at t_*=25000, was 0.02D, 0.03D, 0.08D, 0.11D, 0.14D, 0.15D, for the 0 ^{o}, 24 ^{o}, 45 ^{o}, 90 ^{o}, 135 ^{o}, 180 ^{o} planes, respectively. Another major difference shown in the 180^{o} plane, in Figure 5, is that significant deposition close to the surface of the pier took place only in the small pier experiment, during the initial instants of scour (t_*<2000).

Further, it can be observed from Fig. 5 that the rate of dimensionless scour at the initial phase was higher in the large pier experiment, in all planes.

Figure 6 includes the scour depth profiles on the centerline planes upstream and downstream of the pier, for the two experiments, at $t_* = 31700$. These profiles are composed from measurements obtained by the ARFs and the ADVs. The nondimensionalized upstream centerline profiles were nearly identical, while significant differences were observed at the downstream profiles. The slopes of the downstream centerline profiles were 20^o and 37^o for the small and the large pier experiments, respectively. The upstream slope was 38^o and this compares well with the angle of repose of the median sediment diameter ($\theta = 40^o$). The horizontal span of the scour hole along the upstream centerline planes scaled very well with D, as well.

According to the traditional concepts in the physical modelling of bridge scour, because the Fr number is kept the same, the observed differences in the scour depth would be attributed to the dimensionless flow depth (H/D) and the dimensionless sediment coarseness (D/d_{50}). In particular, the effects of H/D would be expected to result in greater scour for the small pier experiment [*Melville*, 1997]. Furthermore, older studies proposed that the effect of the dimensionless sediment coarseness is not expected to be significant in the range of the current experiments ($D/d_{50}>25$) [*Melville*, 1997]. However, more recent studies have shown that the scour depth would be expected to be higher for the small pier experiment, due to the lower D/d_{50} parameter [*Sheppard et al.*, 2004; *Lee and Sturm*, 2009]. Lastly, in the very few studies that compared or examined the scour depth as a function of Re_D, it was observed that nondimensionilized scour decreases as Re_D increases [*Raudkivi*, 1986; *Ettema et al.*, 2006]. Contrary to the aforementioned functional relationships, here

we observe that the nondimensionilized scour depth is identical at the front of the pier and it becomes greater towards the wake of the pier for the large pier experiment. One possible explanation for these contradictions is that the existing functional relationships have not been tested at the scale of the experiments that are presented here. It is also noteworthy that the effects of the dimensionless parameters on the shape of the scour hole are rarely discussed in the literature, since usually measurements are carried out only at the front of the pier. In the following sections, we will explain the observed differences in the shapes of the scour holes, via the velocity measurements that were carried out during the second phase of the experiments.

4.3.2.1 Overview of the Average Flow Field

The average flow field on the plane of symmetry, for the large pier experiment, is illustrated in the vector diagram in Figure 6a. Some qualitative characteristics of the flow that have been well described in the literature were also observed here [*Dargahi*, 1990; *Melville and Coleman*, 2000]. The effect of the pier size on the average velocity profiles was not evident upstream of the edge of the scour hole. Very close to the pier(x/D=-0.57), on the upstream plane of symmetry, a very strong downward flow existed. The downward flow components and the reversed flow direction very close to the bed at x/D=-0.57 and x/D=-0.73, provide an indication that a horseshoe vortex was present which rotated in the clock-wise direction. Another commonly observed component of the flow, namely the corner vortex, that should rotate in the anti-clockwise direction, at the junction of the pier with the upstream plane of symmetry, was not detected here. This could be attributed to the resolution and location of the current measurements. The average flow, upstream of the smaller pier (Figure 6b),

is similar to the larger pier for z/D>0.05. A qualitative difference between the two experiments is that is that flow reversal is observed only upstream of the larger pier.

On the downstream centerline of the large pier (Figure 6a), the effect of the pier on the average flow dissipated significantly before x/D = 0.95. At both x/D = 0.58 and x/D = 0.75, there was a very strong upward velocity component. At x/D = 0.58 the streamwise component of the flow was negative, while at x = 0.95, the streamwise velocity was positive. The main characteristics of the average velocities at the wake of the pier were the strong upward component and the weak streamwise component. Another qualitative difference between the two experiments is that the span of the area that the aforementioned components were present, was smaller at the larger pier experiment. A more quantitative examination of the average flow velocities along with the turbulence statistics follows next.

4.3.2.2 Flow Field Upstream of the Pier

In this section, vertical profiles of the flow statistics for the two experiments will be presented. Comparisons between the results of the two experiments will be made for the measurements that were carried out at the same nondimensionalized coordinates. In the notation used here: Vx, Vy and Vz are the streamwise, spanwise and vertical velocity components. Also, uu, vv and ww are the normal stresses towards the streamwise, spanwise and vertical directions. Finally, uv, uw, vw are the respective Reynolds stresses.

At x/D = -0.57 (Fig. 7), the average flow velocities were very similar. The most important difference was that for the smaller pier experiment, there was no reversed flow, while for the larger pier experiment there was weak reversed flow close to the bed. For both cases, the vertical velocity component was dominant. The downward flow was stronger under the

original bed elevation (z/D = -0.1 to -0.2). The spanwise velocity component in this location was small over the entire depth.

The plots of turbulence kinetic energies (TKE) and normal stresses of the two experiments showed significant differences (Fig. 8). In the larger pier case, there was a very strong bulge of TKE at the level of the original bed elevation (z/D = 0), while the vertical distribution of TKE in the smaller pier case was almost uniform. The TKE profile of the larger pier case showed similar trends with results reported in the literature from small-scale experiments over developing scour holes (e.g. [*Istarto and Graf*, 2002; *Kumar et al.*, 2012]). This peak in the TKE distribution is commonly associated with the core of a coherent vortex [*Kirkil and Constantinescu*, 2007; *Escauriaza and Sotiropoulos*, 2011]. The distribution of the normal stresses at this location (Fig.8) is very similar with the distribution of TKE, with the magnitude of ww being almost half the magnitude of uu and vv.

The distributions of the shear stresses for the two cases were very similar (Fig.8). The shear stresses were one order of magnitude smaller than the normal stresses. The stronger component was the uv stress that is higher above the original bed elevation. Also, the uw-stress distributions showed a peak at the elevation of the original bed.

At x/D=-0.74 (Fig.9), the similarity of the velocity distributions for the two cases was slightly reduced, compared to the measurements at x/D=-0.57. In the larger pier case, the downward component of the flow was stronger, while in the smaller pier case, the forward component of the flow was stronger. Reversed flow close to the bed was observed only for the larger pier case.

The TKE distribution for the smaller pier case showed a gradual increase as the distance from the bed is reduced (Fig.10). On the other hand, for the larger pier case, the TKE distribution showed two very distinct peaks right under and above the original bed elevation. At the peaks, the nondimensionalized TKE magnitudes were up to 3 times higher compared to the respective magnitudes from the low Re case. The magnitude of the peaks at x/D=-0.74 was similar to the magnitude of the peak at x/D=-0.57.

The uu stresses were stronger in both cases compared to the other normal stresses. For the larger pier case, the two peaks were observed only at the uu and vv distributions, while the lower peak was also present at the ww distributions.

The shear stresses were at least one order of magnitude smaller than the normal stresses. The absolute magnitudes of the uw stresses for the smaller pier case were larger compared to the larger pier case, except for a very strong peak observed at the latter case. This peak was located at the same elevation where the lower peak of the TKE distribution (z/D=-0.15) occurred and it was approximately one order of magnitude larger than the maximum uw. This peak was also present at both the uv and vw distributions of the larger pier case. The magnitude in these distributions is significantly lower. The shear stresses of the smaller pier case are always small and do not show any particular trends.

At x/D=-0.92, in the large pier case, the shear stresses (not shown here) were one order of magnitude smaller that at x/D=-0.74. Also at x/D=-0.92, x/D=-1.11 and x/D=-1.34, in the high Re case, there were no distinctive peaks in the Reynolds stresses distributions. This suggests that the effects of the pier on the shear stresses were significantly reduced within the scour hole at approximately $x/D \geq -1$.

The resemblance in the nondimensionalized average velocities at x/D=-0.57 and x/D=-0.74, on the upstream plane of symmetry was expected and is consistent with the scaled bathymetric measurements. Overall, the main difference between the two cases, at the upstream flow field, is with respect to the evidence for the existence of a horseshoe vortex. The reversed flow close to the bed, along with the strong peaks of TKE at the level of the original bed, were suggestive of the location of the core of a horseshoe vortex. These elements of the flow exist only at the larger pier case. This may suggest that at this stage of scour there is not a coherent vortex, in the smaller pier case. Also, it is possible that a coherent vortex exists, but it is not detectable in the average flow statistics, because its location varies significantly with time [*Dargahi*, 1989]. Interestingly, the presence of a coherent vortex does not seem to affect the shear stresses very close to the bed, at least, at this stage of scour.

Probability distributions of the velocity measurements upstream of the pier were computed at selected locations. *Devenport and Simpson* [1990] were the first to report the existence of bimodal distributions of the velocity fluctuations. It was suggested that the bimodal behavior is associated with the dynamics of the horseshoe vortex. This behavior has been validated in both numerical investigations and small-scale, bridge scour experiments by *Lee and Sturm* [2009] and *Escauriaza and Sotiropoulos* [2011b], respectively. However, this signature behavior was not observed here, for either of the experiments. Figure 11 includes the probability density functions of the streamwise velocity fluctuations, at various distances from the bed. It is shown that the pdfs follow approximately normal distributions, without significant variations.

4.3.2.3 Flow Field Downstream of the Pier

At x/D=0.58 (i.e. very close to the pier), for both cases, the overall velocity magnitude was higher close to the bed and decreases towards the free surface (Fig.12). For the larger pier case, the upward vertical component was larger, while for the smaller pier case the backward horizontal component was stronger. For both cases, the upward component was stronger at z/D=0, approximately. The most important difference between the two cases was with respect to the spanwise velocity component (v). This component showed two very strong peaks of opposite direction for the larger pier case, while it is small and uniform for the smaller pier case. Both of the peaks for the larger pier case were located below the original bed elevation. Overall, for the larger pier case, the average flow is 3-dimensional while for the smaller pier case, the flow is mostly 2-dimensional.

For both cases, the TKE and normal stress distributions showed a strong peak (Fig.13). For the smaller pier case, the peak was located at z/D=0, while for the larger pier case the peak was at z/D=-0.1. The highest normal stresses are in the spanwise direction. The TKE was higher for the larger pier case. The TKE values at x/D=0.58 were at least two times higher than those at x/D=-0.54 and x/D=-0.75.

Above z/D=0, the shear stresses for both cases were very similar, while under z/D=0 the stresses were higher for the larger pier case. While on the upstream symmetry plane the stronger stresses were observed in the uw stress, here the stronger stresses were observed in uv and vw. The strong vv, uv and wv stresses right on the bed elevation, suggest that the excavated sediments transport towards the spanwise direction, after entrainment. The shear stresses on the downstream plane of symmetry were larger than at the upstream plane of symmetry.

At x/D=0.95, for the larger pier experiment, due to technical difficulties it was not possible to obtain measurements in the upper half of the flow. At this location, there were significant differences in the distributions of the velocity components. The streamwise and spanwise components were stronger for the high Re case (Fig14). The streamwise components for both cases were positive, with the only exception being for the smaller pier case that had a weakly backward moving component close to the bed. The spanwise components for both cases changed direction at a certain elevation. For the smaller pier case this elevation was z/D=0.15 and for the larger pier case it was z/D=0. The vertical components of the velocities are very similar for both cases.

At this location, scour was larger for the larger pier case, while it was almost zero for the low Re case. Here, the profiles of the TKE and the normal stresses are very similar for z/D>0 (Fig.15). The TKE distributions were of similar magnitudes and are maximized at z/D=0. The strongest normal stresses are the vv stresses that were 2-3 times higher than the uu and ww stresses. At this location, the TKE and the normal stresses were much larger compared to x/D=0.58.

The shear stresses were approximately 20% of the normal stresses and were of similar magnitude for both cases. The stronger stresses acted on the uv plane. For both cases, the shear stresses exhibited a change of direction. For the high Re case, this change took place at z/D=0, while for the smaller pier case, there was not an apparent trend. Overall, the significantly greater shear stresses that were observed in the larger pier case justify the higher scour depth, on the downstream centerline. The primary direction of the shear stresses and thus of the particle entrainment, was the spanwise.

The velocity signals downstream of the pier were examined in the frequency domain, to investigate the effect of Re_D on the shedding frequency and energy of the shedding wake vortices. The power spectral densities of two samples are illustrated, in Fig.16. Also, the dominating frequencies and the associated powers varied with the flow depth. Table 2 includes the median frequencies and powers for the two experiments at x/D=0.58 and x/D=0.95. As expected, the vortex shedding frequency (0.32Hz-0.41Hz) is very close to the dominating frequency that was observed in the scour signals in the wake (0.15Hz-0.65Hz); similar observations were made by *Dargahi*, [1989] and *Ettema et al.*, [2006]. The differences between the two cases are small; however, it was observed that the power for the larger pier experiment was consistently higher compared to the smaller pier experiment.

Overall, at the plane of symmetry, downstream of the pier, the comparisons of the average flows showed significant differences. These differences were evident in both the average velocities and the Reynolds stresses. Apparently, the differences in the bathymetry of the scour hole at the wake of the pier are better explained through the significant differences in the average velocities and turbulence statistics, rather on the shedding frequencies, which were similar. Particularly, the Reynolds stresses very close to the bed at x/D=0.58, that were 2-3 times higher for the larger pier experiment may explain the largest scour depth. The fact that the effects of the pier on the flow at the wake become less intense sooner at the larger pier experiment (better shown in Fig.6), explains why the slope of the centerline downstream of the larger pier is almost twice the slope downstream of the smaller pier.

4.4 Conclusions

We presented the results of two bridge scour, clear-water experiments that were carried out at near-prototype pier-based Reynolds numbers. The only dimensional parameter that was not constant between these experiments was the pier diameter. The design of the experiments, allowed for direct comparisons of the multiple characteristics of the scour and the flow around the piers. It was found that the flow field at the wake of the pier was significantly different for the two experiments. Specifically, it was observed that for $Re_{D1}=9.1*10^5$ the flow immediately downstream of the pier was strongly three-dimensional and that very high stresses were exerted near the bed, towards the spanwise direction. These stresses were 2-3 times higher compared to the ones observed at the experiment with $Re_{D2}=6.1*10^5$. Consistent with this higher stress, the scour depth at the wake of the larger pier was significantly greater and the slope of the bed was almost twice than at the smaller pier. The effects on the bed bathymetry were evident around the perimeter of the pier, as well. Specifically, the scour depth throughout the experiments and the scour rates at the initial stage of scour were higher for the larger-pier experiment. Right on the upstream face of the piers, the dimensionless scour depth and the slope of the scour hole were identical for the two experiments. The flow measurements on the centerline, upstream of the pier, showed that the average flow velocities were very similar and that there were differences in the turbulence statistics inside the scour hole, on the upstream plane of symmetry. These differences indicate that a coherent vortex on the upstream centerline is only evident in the high Re_{D1} experiment, via the examination of the average-flow statistics.

The presented results contradict many widely used functional relationships that would predict a deeper scour hole around the smaller pier. It is very likely that this is due to the

fact that existing laboratory investigations have been carried out at Reynolds numbers that are usually one order of magnitude lower than the expected prototype values and that there have not been significant efforts to quantify the effects of this parameter. Further, the main emphasis of bridge scour investigations is with respect to the flow field upstream of the pier, for various conditions. However, here it is suggested that for two experiments with different pier diameters, the most important changes are observed on the centerline downstream of the pier and that these changes affect the bed bathymetry around the pier.

The main purpose of this study is to provide insight on the scale effects that are inherent in existing bridge scour investigations and not to derive new functional relationships. The descriptions of the flow and the scour that are included here would be very difficult to obtain at the field and offer a much better perception of the phenomenon, as opposed to mere values of equilibrium scour. The presented statistics of scour and flow can be used towards the improvement of numerical models and for comparisons with the results of small scale studies.

Acknowledgements

The authors would like to thank the National Science Foundation (EAR 0738759) and the Research Office of the United States Army Corps of Engineers (ARO 53512-EV) for their support for this study. The first author is also grateful to the Virginia Water Resources Research Center, the Gerondelis Foundation, and the Edna Bailey Sussman Foundation.

References

Annandale, G. W. (2006), Scour technology : mechanics and engineering practice, xviii, 430 p. pp., McGraw-Hill, New York.

Arneson, L. A., L. W. Zevenbergen, P. F. Lagasse, and P. E. Clopper (2012), Evaluating Scour at Bridges, Fifth EditionRep., 340p pp.

Baker, C. J. (1980), The turbulent horseshoe vortex, Journal of Wind Engineering and Industrial Aerodynamics, 6(1–2), 9-23.

Briaud, J., F. Ting, H. Chen, R. Gudavalli, S. Perugu, and G. Wei (1999), SRICOS: Prediction of Scour Rate in Cohesive Soils at Bridge Piers, Journal of Geotechnical and Geoenvironmental Engineering, 125(4), 237-246.

Dargahi, B. (1989), The turbulent flow field around a circular cylinder, Exp Fluids, 8(1-2), 1-12.

Dargahi, B. (1990), Controlling Mechanism of Local Scouring, Journal of Hydraulic Engineering, 116(10), 1197-1214.

Devenport, W. J., and R. L. Simpson (1990), Time-dependent and time-averaged turbulence structure near the nose of a wing body junction, J. Fluid Mech., 210, 23-55.

Dey, S., and R. Raikar (2007), Characteristics of Horseshoe Vortex in Developing Scour Holes at Piers, Journal of Hydraulic Engineering, 133(4), 399-413.

Escauriaza, C., and F. Sotiropoulos (2011a), Initial stages of erosion and bed form development in a turbulent flow around a cylindrical pier, Journal of Geophysical Research: Earth Surface, 116(F3), F03007.

Escauriaza, C., and F. Sotiropoulos (2011b), Reynolds Number Effects on the Coherent Dynamics of the Turbulent Horseshoe Vortex System, Flow Turbulence Combust, 86(2), 231-262.

Ettema, R., B. Melville, and B. Barkdoll (1998), Scale Effect in Pier-Scour Experiments, Journal of Hydraulic Engineering, 124(6), 639-642.

Ettema, R., G. Kirkil, and M. Muste (2006), Similitude of Large-Scale Turbulence in Experiments on Local Scour at Cylinders, Journal of Hydraulic Engineering, 132(1), 33-40.

Ettema, R., National Research Council (U.S.). Transportation Research Board., National Cooperative Highway Research Program., American Association of State Highway and Transportation Officials., and United States. Federal Highway Administration. (2011), Evaluation of bridge scour research: Pier scour processes and predictions, Transportation Research Board, Washington, D.C.

Goring, D., and V. Nikora (2002), Despiking Acoustic Doppler Velocimeter Data, Journal of Hydraulic Engineering, 128(1), 117-126.

Gunawan, B, Neary, V.S., McNutt, J. (2011). ORNL ADV Post-processing guide and MATLAB

algorithms for MHK Site flow and turbulence analysis. ORNL/TML-2011/338

Islam, M. R., and D. Z. Zhu (2013), Kernel Density-Based Algorithm for Despiking ADV Data, J. Hydraul. Eng.-ASCE, 139(7), 785-793.

Istiarto, I., and Graf, W. H. 2001. Experiments on flow around a cylinder in a scoured channel bed. International Journal of Sediment Research, 16(4), 431-444.

Kirkil, G., and G. Constantinescu (2009), Nature of flow and turbulence structure around an in-stream vertical plate in a shallow channel and the implications for sediment erosion, Water Resources Research, 45(6), W06412.

Kirkil, G., G. Constantinescu, and R. Ettema (2009), Detached Eddy Simulation Investigation of Turbulence at a Circular Pier with Scour Hole, Journal of Hydraulic Engineering, 135(11), 888-901.

Koken, M., and G. Constantinescu (2009), An investigation of the dynamics of coherent structures in a turbulent channel flow with a vertical sidewall obstruction, Physics of Fluids (1994-present), 21(8), -.

Kothyari, U., W. Hager, and G. Oliveto (2007), Generalized Approach for Clear-Water Scour at Bridge Foundation Elements, Journal of Hydraulic Engineering, 133(11), 1229-1240.

Kumar, A., U. C. Kothyari, and K. G. R. Raju (2012), Flow structure and scour around circular compound bridge piers - A review, J. Hydro-environ. Res., 6(4), 251-265.

Lança, R., C. Fael, R. Maia, J. Pêgo, and A. Cardoso (2013), Clear-Water Scour at Comparatively Large Cylindrical Piers, Journal of Hydraulic Engineering, 139(11), 1117-1125.

Lee, S., and T. Sturm (2009), Effect of Sediment Size Scaling on Physical Modeling of Bridge Pier Scour, Journal of Hydraulic Engineering, 135(10), 793-802.

Melville, B. (1997), Pier and Abutment Scour: Integrated Approach, Journal of Hydraulic Engineering, 123(2), 125-136.

Melville, B., and Y. Chiew (1999), Time Scale for Local Scour at Bridge Piers, Journal of Hydraulic Engineering, 125(1), 59-65.

Melville, B. W., and S. E. Coleman (2000), Bridge scour, xxii, 550 p. pp., Water Resources Publications, LLC, Highlands Ranch, Colo.

Oliveto, G., and W. Hager (2002), Temporal Evolution of Clear-Water Pier and Abutment Scour, Journal of Hydraulic Engineering, 128(9), 811-820.

Oliveto, G., and W. H. Hager (2005), Further results to time-dependent local scour at bridge elements, J. Hydraul. Eng.-ASCE, 131(2), 97-105.

Parsheh, M., F. Sotiropoulos, and F. Porté-Agel (2010), Estimation of Power Spectra of Acoustic-Doppler Velocimetry Data Contaminated with Intermittent Spikes, Journal of Hydraulic Engineering, 136(6), 368-378.

Raudkivi, A. (1986), Functional Trends of Scour at Bridge Piers, Journal of Hydraulic Engineering, 112(1), 1-13.

Sheppard, D., M. Odeh, and T. Glasser (2004), Large Scale Clear-Water Local Pier Scour Experiments, Journal of Hydraulic Engineering, 130(10), 957-963.

Sheppard, D. M., B. Melville, and H. Demir (2014), Evaluation of Existing Equations for Local Scour at Bridge Piers, Journal of Hydraulic Engineering, 140(1), 14-23.

Sheppard, D. M., H. Demir, B. W. Melville, National Research Council (U.S.). Transportation Research Board., National Cooperative Highway Research Program., American Association of State Highway and Transportation Officials., and United States. Federal Highway Administration. (2011), Scour at wide piers and long skewed piers, 55 p. pp., Transportation Research Board, Washington, D.C.

Shirole, A. M., and R. C. Holt (1991), Planning for a comprehensive bridge safety assurance program, Transportation Research Board.

Unger, J., and W. Hager (2007), Down-flow and horseshoe vortex characteristics of sediment embedded bridge piers, Exp Fluids, 42(1), 1-19.

Wahl, T. L. (2000). "WinADV computer ." Bureau of Reclamation, Water Resources Research laboratory.

Wardhana, K., and F. Hadipriono (2003), Analysis of Recent Bridge Failures in the United States, Journal of Performance of Constructed Facilities, 17(3), 144-150.

List of Figures

Figure 1. View of the ERDC flume from the downstream end.

Figure 2. View of the instrumented, 0.61m-wide pier. Flow direction is from right to left. On the centerline upstream of the pier, 4 ADVs and an array of ARFs are visible. Three ARFs on the surface of the pier can be observed.

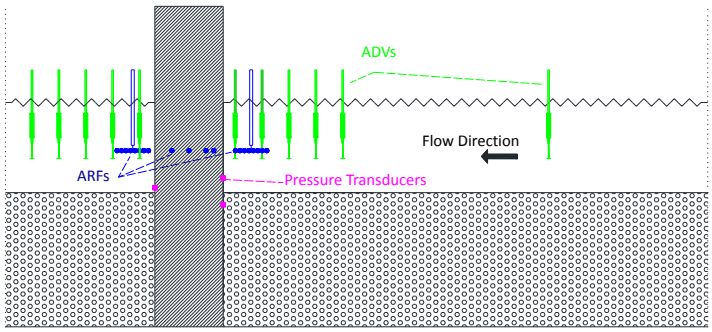

Figure 3. Sketch (not to scale) that illustrates all the possible positions of the main instruments. All depicted instruments could be translated except for those located on the pier.

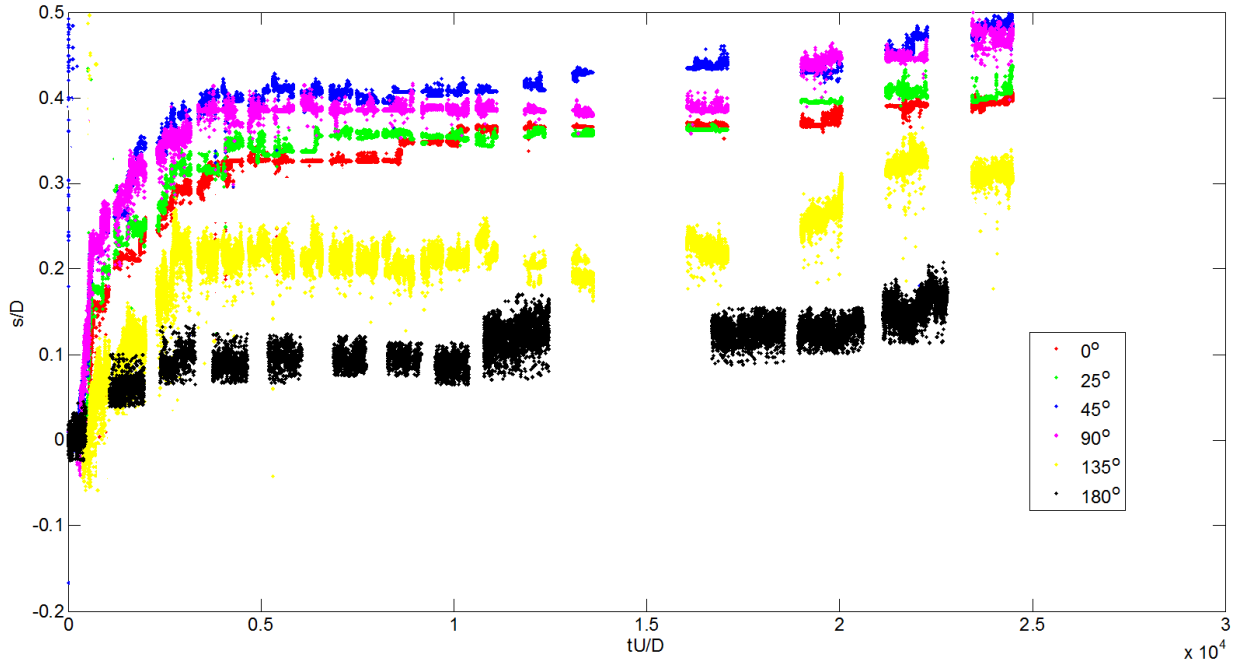

Figure 4. Temporal evolution of nondimensionalized scour depth at various planes around the larger pier. Measurements are 1.27cm away from the surface of the pier.

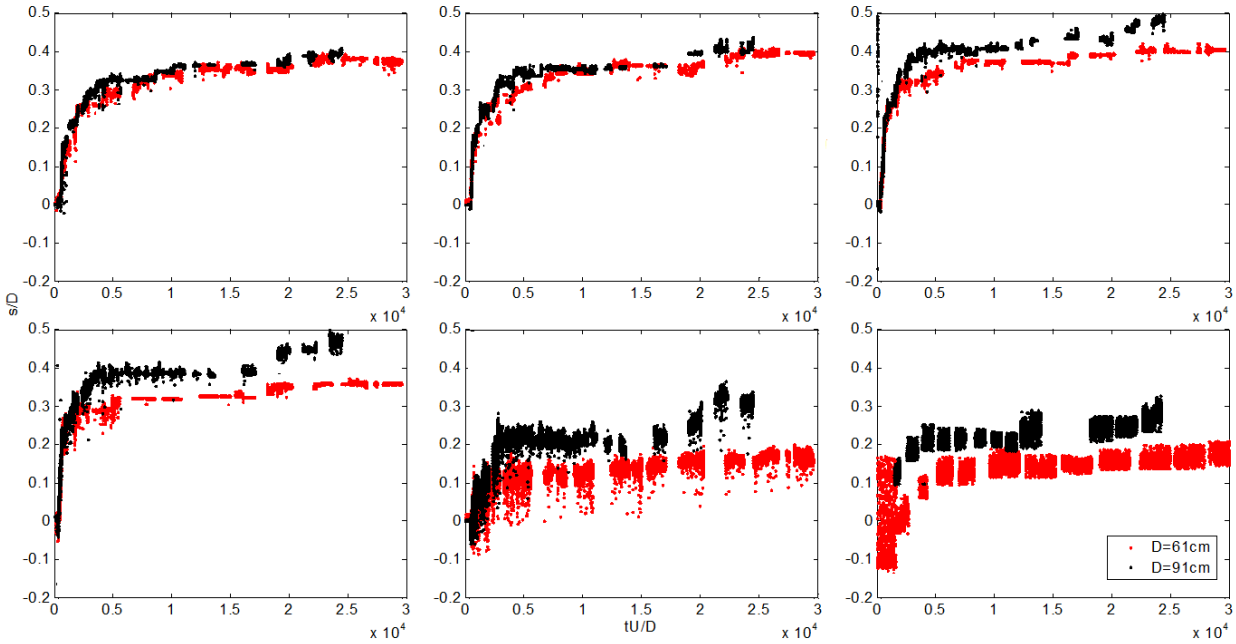

Figure 5. Comparison between the nondimensionalized scour depth of the large pier and small pier experiments, at the 0 º (top left), 24 º (top center), 45 º (top right), 90 º (bottom left), 135 º (bottom center), 180 º (bottom right) planes, close to the surface of the pier.

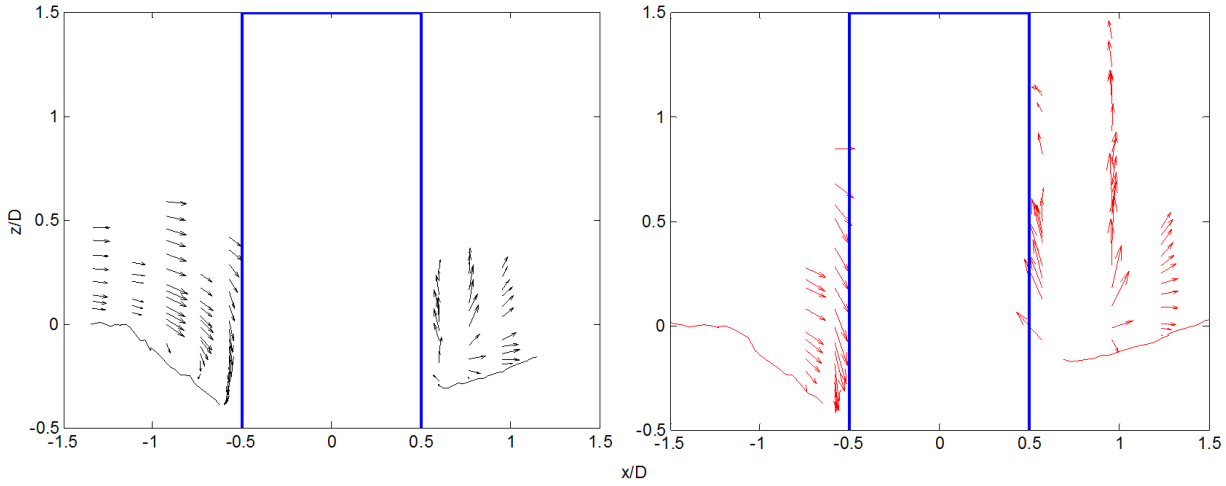

Figure 6. The average flow field on the plane of symmetry for the larger pier experiment (left) and the smaller pier experiment (right).

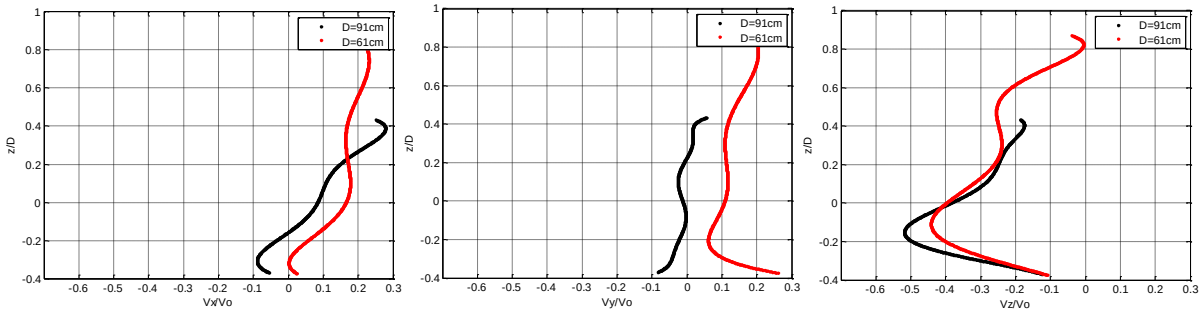

Figure 7. Vertical profiles of the average velocity components, at x/D=-0.57.

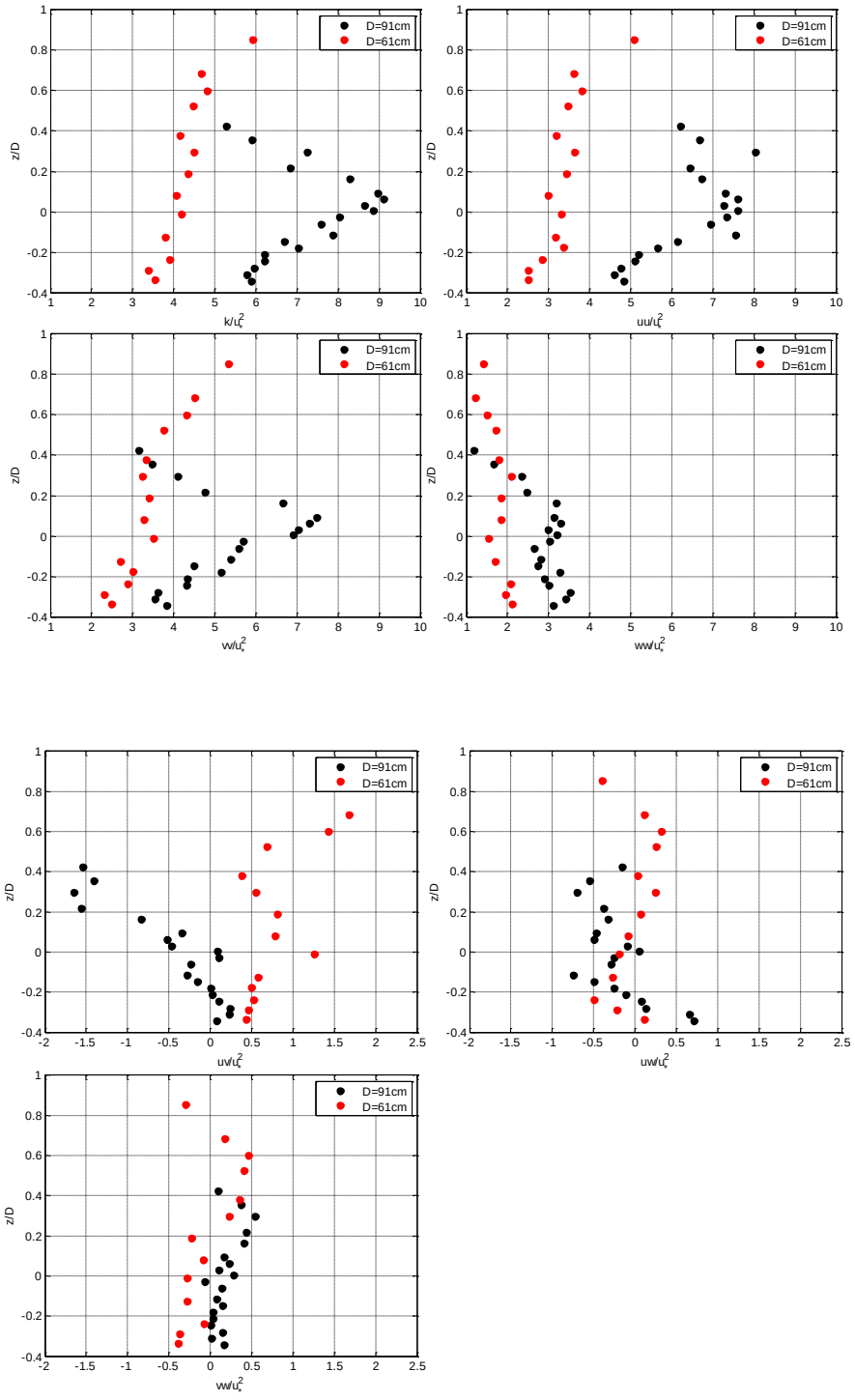

Figure 8. Vertical profiles of the average turbulence kinetic energy and the Reynolds stresses, at x/D = -0.57.

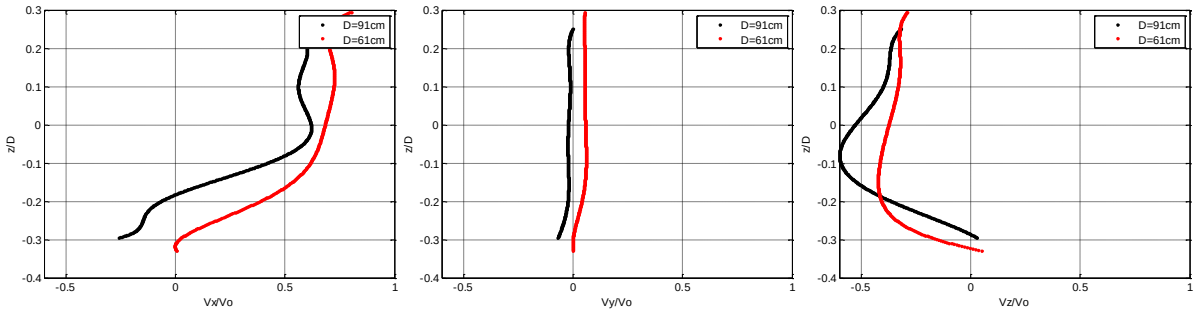

Figure 9. Vertical profiles of the average velocity components at x/D=-0.74.

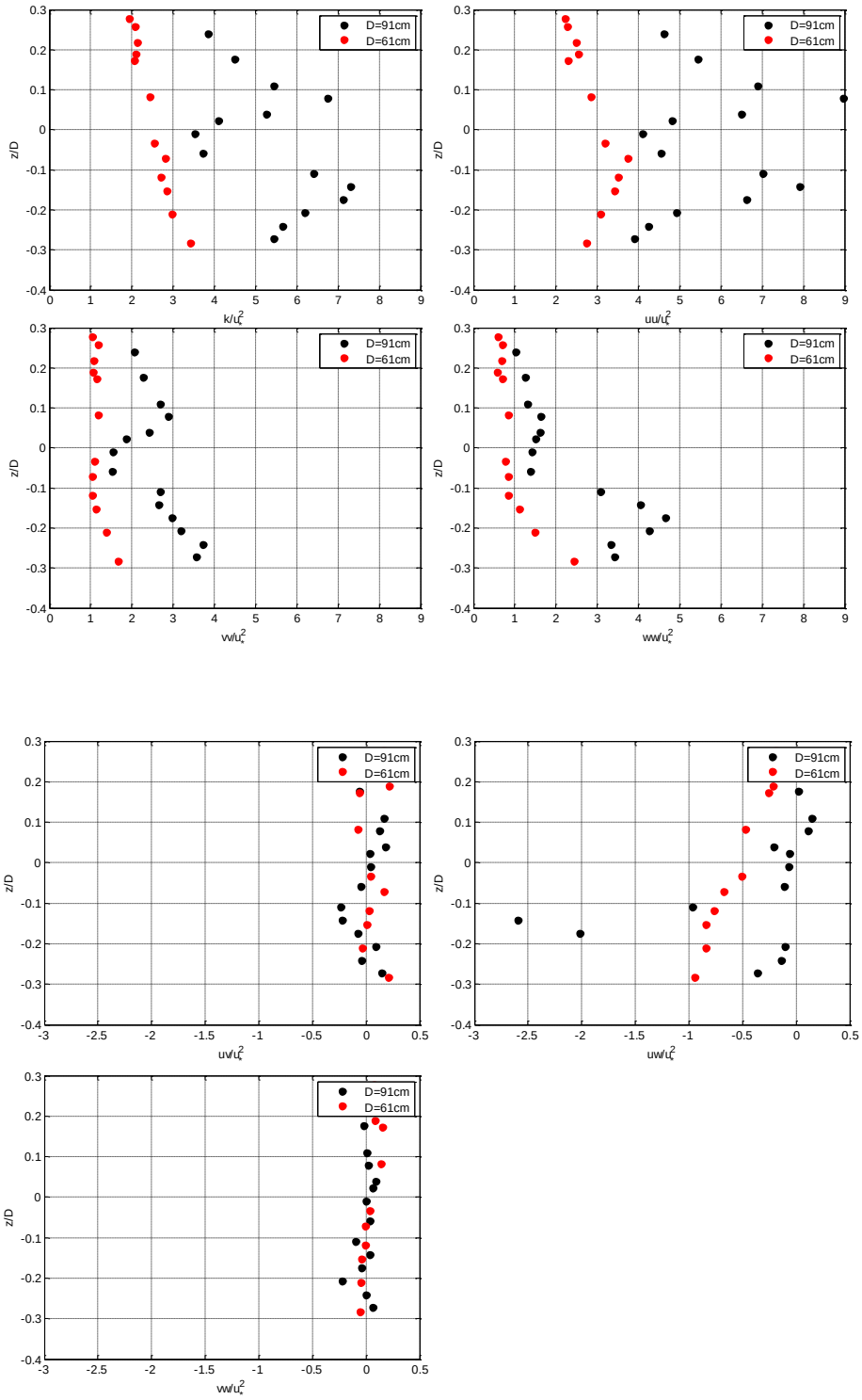

Figure 10. Vertical profiles of the average turbulence kinetic energy and the Reynolds stresses at

x/D = -0.74.

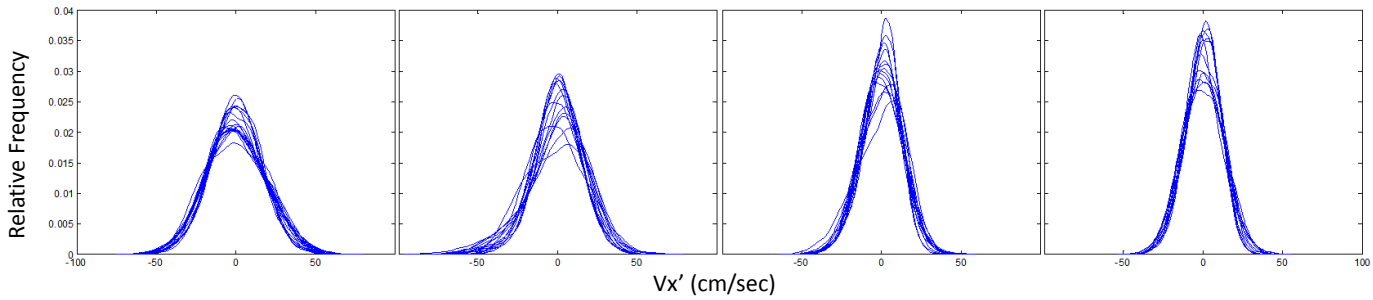

Figure 11. Probability density functions of the streamwise velocity fluctuations, at multiple elevations that span the entire depth for a. x/D=-0.57 smaller pier; b. x/D=-0.57 larger pier; c. x/D=-0.74 smaller pier; d. x/D=-0.74 larger pier.

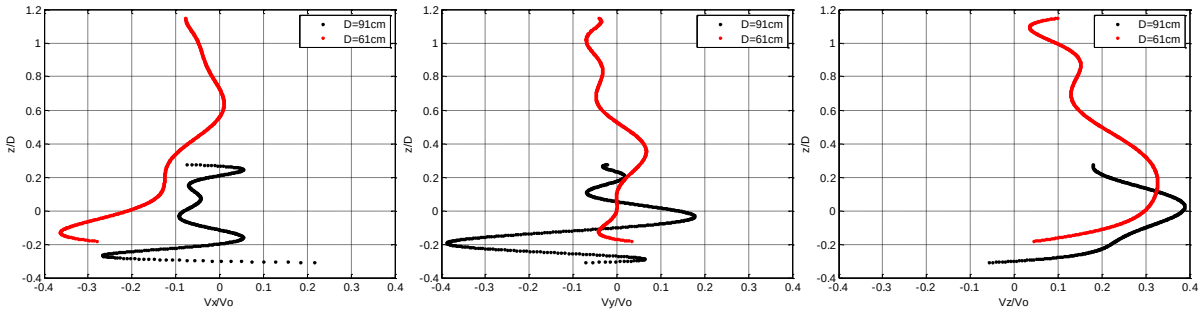

Figure 12. Vertical profiles of the average velocity components, at x/D=0.58.

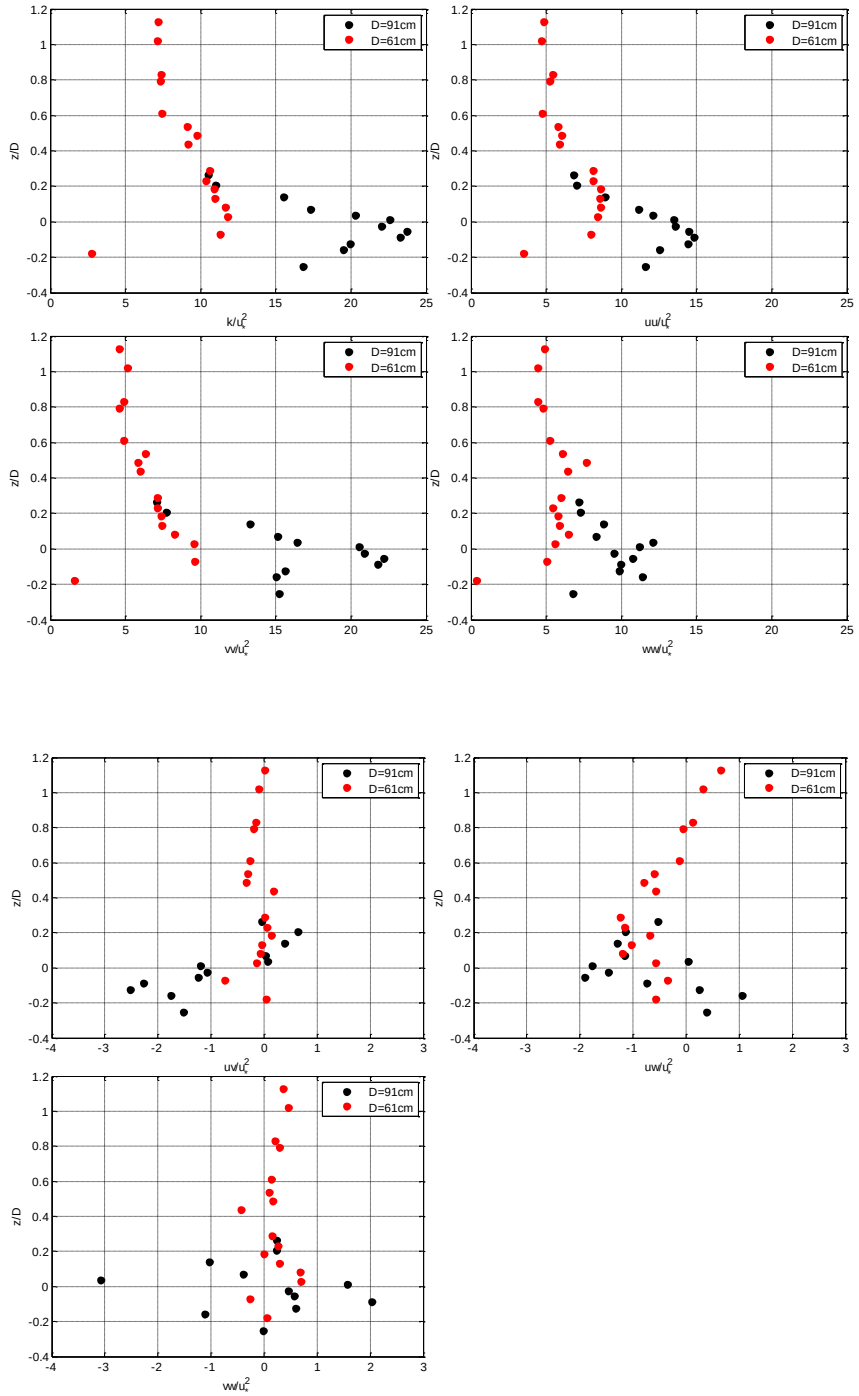

Figure 13. Vertical profiles of the average turbulence kinetic energy and the Reynolds stresses, at x/D=0.58.

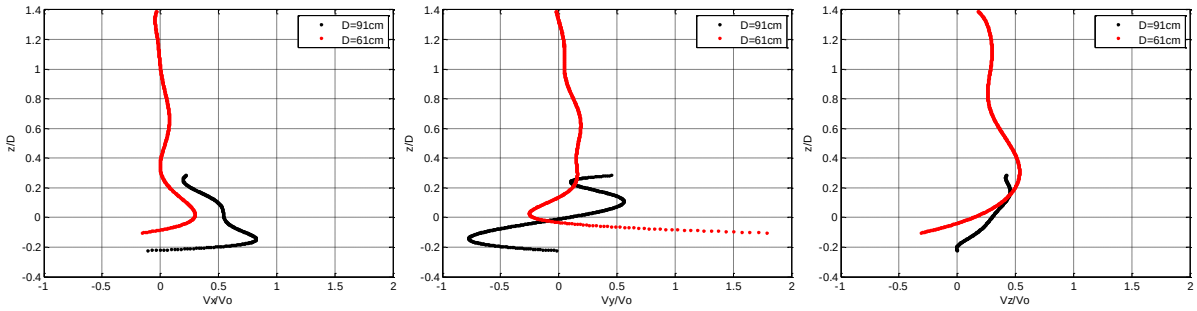

Figure 14. Vertical profiles of the average velocity components, at x/D=0.95.

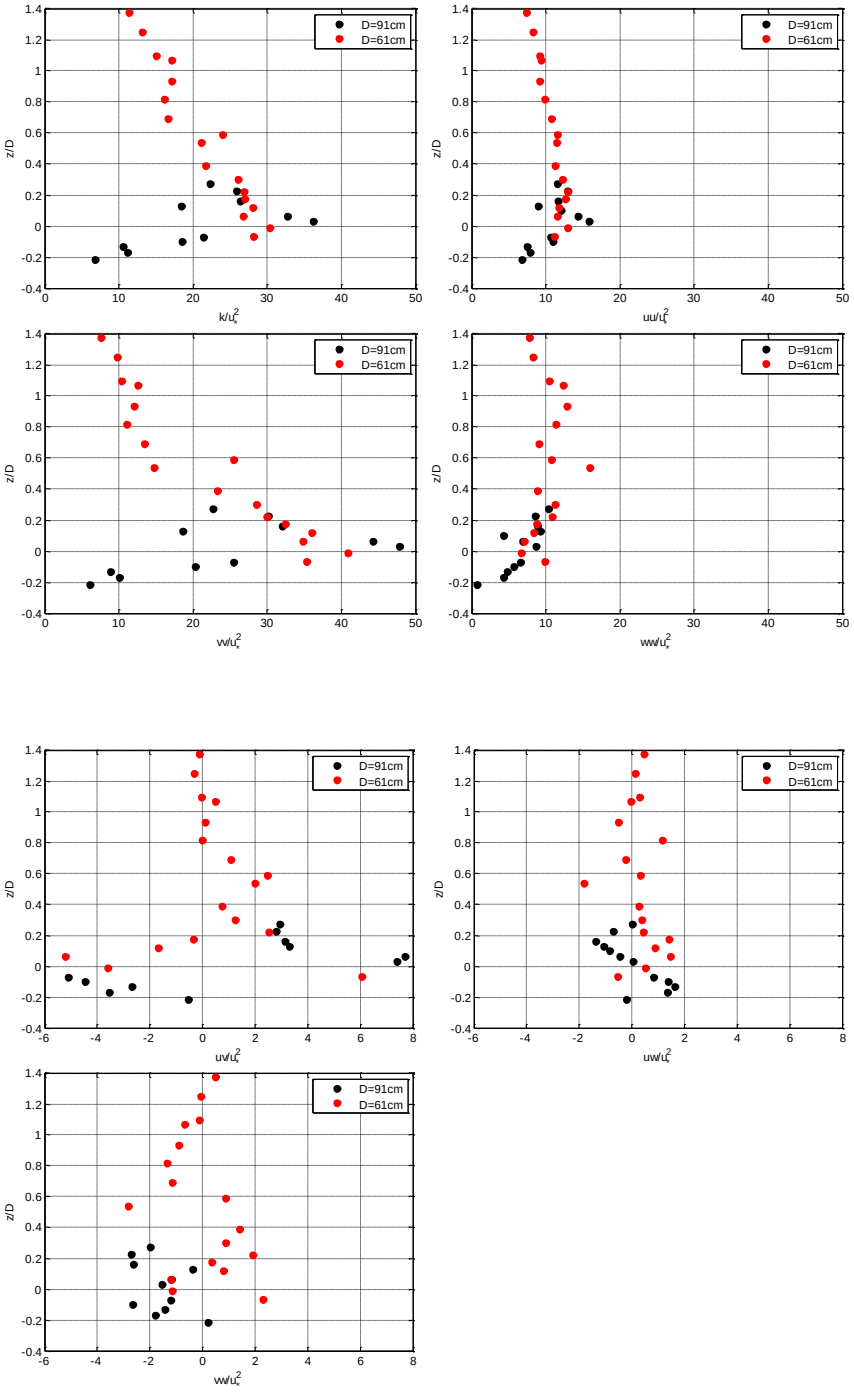

Figure 15. Vertical profiles of the average turbulence kinetic energy and the Reynolds stresses, at x/D=0.95.

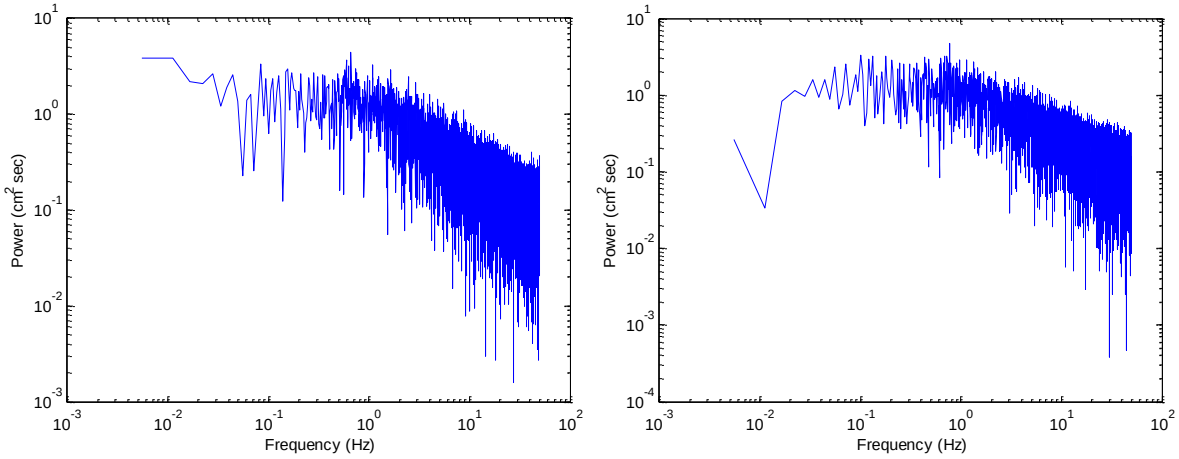

Figure 16. Power spectral densities at x/D=0.95 and z/D=0.2, for the smaller (left) and the larger pier (right) experiments.

List of Tables

Table 1. The more important dimensionless parameters of the experiments.

	Re_D	Fr_H	Fr_{d50}	H/D	D/d_{50}	u_*/u_{*c}
1	$9.2*10^6$	0.33	0.058	0.65	64	0.70
2	$9.1*10^6$	0.33	0.058	0.98	42	0.70

Table 2. Median shedding frequencies and power at the wake of the pier.

Pier	**x/D**	**F(Hz)**	**Power (cm^2 sec)**
smaller	0.95	0.41	3.78
larger	0.95	0.37	4.07
smaller	0.58	0.33	3.15
larger	0.58	0.32	4.14

Chapter 5. Conclusions

This research is divided in three main parts. In the first part (Chapter 2), the development of a new computer vision technique for the monitoring of evolving sediment beds in laboratory experiments was presented. The second part (Chapter 3), involved the description of the application of the technique in a water flume, at the Baker Environmental Hydraulics Laboratory, at Virginia Tech. In the third part (Chapter 4), the results of two experiments that were carried out at near-prototype conditions, in a large channel, at the Environmental Research and Development Center of the US Army Corps of Engineers, were compared.

Regarding the first part of this work, it was shown that the developed underwater photogrammetric technique can obtain uninterrupted, non-intrusive, 3D representations of the evolving scour hole topography. The technique outperforms existing methodologies in terms of spatiotemporal resolution and simplicity. It accepts pairs of coincident frames from a couple of video cameras that record the evolving bed. Then, it performs a series of computer vision algorithms for semi-automatic calibration and automatic correspondence establishment, outlier removal, stereo triangulation and surface fitting to produce detailed representations of the sediment bed. The main computational novelties include the correspondence establishment and outlier removal algorithms; however, the ensemble of the algorithms that were put together for the first time, for this laboratory application, showed significant advantages that suggest that this technique can be used in a wide-range of sediment transport and scour experiments.

In the second part, the underwater photogrammetric2 technique was successfully applied to describe thoroughly the morphology of an evolving scour hole around a cylindrical model pier. The bed topography was quantified in detail for the first time, through representations of the instantaneous scour rates, the volume of the excavated material, the slopes around the scour hole and point-wise bathymetric measurements. The results were associated with the findings of previous studies on the flow field around cylinders. Via the data representations and regression analysis it was shown that clear water scour, around cylindrical piers, over cohesionless beds, can be described by 2 phases (initial and development) and that the scour hole can be divide in 3 main regions (front, sides and wake). During the initial phase, scour is driven by high stresses that act on the sides of the cylinder and cause very rapid erosion, there. Based on results from previous studies, it is suggested that slopes around the cylinder are determined by the spatial distribution of the stresses. Then, during the second phase (a.k.a. development phase), scour is driven by small patches of high stresses whose distribution varies in space and time. Despite, these variations, the slopes of the scour hole remain almost constant in time. During the development phase, the most active region is the front of the cylinder, while only small changes are observed at the sides of the pier. The temporal evolution of the volume of the excavated material and the scour depth at the front and the sides is described by a piecewise power law, with one breakpoint that coincides with the end of the initial phase and the beginning of the development phase.

Lastly, in the third part, two clear-water, bridge scour experiments were carried out at a very large scale. The main parameter under investigation was the pier diameter based Reynolds number (Re_D) which was $9.1*10^5$ and $6.1*10^5$ for the two experiments. These

are the highest Re_D values that have been reported in the literature and are representative of flooding conditions at prototype bridges. It was shown that the increase in Re_D affects significantly the flow at the wake of the pier and increases the bed shear stresses there. On the other hand, the stresses close to the bed, on the upstream plane of symmetry, were very similar. The effect of the flow on the bed topography was that the scour hole for the high Re_D case was significantly deeper downstream of the pier and that the bathymetric difference between the two experiments was reduced towards the upstream plane of symmetry, where the scour depths scaled very well with the pier diameter. This work emphasizes the discrepancies of the functional relationships proposed from small scale studies and attributes them on the effects of Re_D on the flow at the wake of the pier.

The logical sequence of this work would be the simultaneous investigation of both flow and scour, with time and space resolved measurements, in small scale experiments. This investigation would be targeted to focus on the most important aspects of the phenomenon as highlighted here. Then, a direct comparison with the obtained large scale data would further contribute to the understanding of the bridge scour phenomenon.